

2016

# Experimental investigation of multiphase flow: Mass transfer and fluid flow in Taylor-Couette reactor and velocity field of train of particles in a square duct

Mahdi Ramezani  
Iowa State University

Follow this and additional works at: <https://lib.dr.iastate.edu/etd>

 Part of the [Chemical Engineering Commons](#), and the [Mechanical Engineering Commons](#)

## Recommended Citation

Ramezani, Mahdi, "Experimental investigation of multiphase flow: Mass transfer and fluid flow in Taylor-Couette reactor and velocity field of train of particles in a square duct" (2016). *Graduate Theses and Dissertations*. 15998.  
<https://lib.dr.iastate.edu/etd/15998>

This Dissertation is brought to you for free and open access by the Iowa State University Capstones, Theses and Dissertations at Iowa State University Digital Repository. It has been accepted for inclusion in Graduate Theses and Dissertations by an authorized administrator of Iowa State University Digital Repository. For more information, please contact [digirep@iastate.edu](mailto:digirep@iastate.edu).

**Experimental investigation of multiphase flow: Mass transfer and fluid flow in Taylor-Couette reactor and velocity field of train of particles in a square duct**

by

**Mahdi Ramezani**

A dissertation submitted to the graduate faculty  
in partial fulfillment of the requirements for the degree of

DOCTOR OF PHILOSOPHY

Major: Mechanical Engineering

Program of Study Committee:

Michael G. Olsen, Major Professor

Shankar Subramaniam

R. Dennis Vigil

Theodore J. Heindel

Rodney O. Fox

Iowa State University

Ames, Iowa

2016

Copyright © Mahdi Ramezani, 2016. All rights reserved.

DEDICATION

To my family and friends who endured years of absence.

## TABLE OF CONTENTS

DEDICATION .....	ii
TABLE OF CONTENTS.....	iii
LIST OF FIGURES .....	vi
LIST OF TABLES .....	xiii
NOMENCLATURE .....	xiv
ACKNOWLEDGMENTS .....	xviii
ABSTRACT.....	xix
CHAPTER 1 INTRODUCTION.....	1
1.1 Taylor-Couette Gas-Liquid Vortex Reactor Mass Transfer .....	2
1.2 Flow Field Investigation around a Train of Particles in a Square Duct.....	6
CHAPTER 2 EXPERIMENTAL MEASUREMENT OF OXYGEN MASS TRANSFER AND BUBBLE SIZE DISTRIBUTION IN AN AIR-WATER MULTIPHASE TAYLOR- COUETTE VORTEX BIOREACTOR.....	9
2.1 Abstract .....	9
2.2 Introduction.....	10
2.3 Experimental Methods .....	12
2.4 Calculations.....	20
2.5 Results and Discussion .....	25
2.6 Conclusion .....	38
2.7 Acknowledgements.....	40

CHAPTER 3	EXPERIMENTAL INVESTIGATION OF THE EFFECT OF ETHYL ALCOHOL SURFACTANT ON OXYGEN MASS TRANSFER AND BUBBLE SIZE DISTRIBUTION IN AN AIR-WATER MULTIPHASE TAYLOR-COUETTE VORTEX BIOREACTOR.....	41
3.1	Abstract.....	41
3.2	Introduction.....	42
3.3	Experimental Methods.....	45
3.4	Results and Discussion.....	53
3.5	Conclusion.....	62
3.6	Acknowledgement.....	63
CHAPTER 4	AN ADAPTIVE MODEL FOR GAS-LIQUID MASS TRANSFER IN A TAYLOR VORTEX REACTOR.....	64
4.1	Abstract.....	64
4.2	Introduction.....	65
4.3	Model equations.....	70
4.4	Simulation approach and computational details.....	78
4.5	Results and discussion.....	81
4.6	Conclusions.....	99
4.7	Acknowledgments.....	101

CHAPTER 5	EXPERIMENTAL INVESTIGATION OF HYDRODYNAMIC FLUID- PARTICLE INTERACTIONS USING VELOCITY FIELD COMPARISON OF A FIXED TRAIN OF SPHERICAL PARTICLES INSIDE A SQUARE DUCT .....	102
5.1	Abstract .....	102
5.2	Introduction .....	102
5.3	Experimental setup and procedure .....	104
5.4	Results and Discussion .....	108
5.5	Conclusions .....	117
CHAPTER 6	DETAILED EXPERIMENTAL AND NUMERICAL INVESTIGATION OF HYDRODYNAMIC FLUID-PARTICLE INTERACTIONS USING VELOCITY FIELD COMPARISON OF A FIXED TRAIN OF SPHERICAL PARTICLES INSIDE A SQUARE DUCT .....	118
6.1	Abstract .....	118
6.2	Introduction .....	119
6.3	Approach .....	121
6.4	Results and Discussion .....	135
6.5	Conclusions .....	150
6.6	Acknowledgements .....	151
CHAPTER 7	CONCLUSION .....	152
CHAPTER 8	REFERENCES .....	156

## LIST OF FIGURES

Figure 2.1 Taylor-Couette vortex reactor .....	13
Figure 2.2 Sample bubble images including the measuring grid. Left: magnified view of bubble measurement zone   middle: 300 rpm - 0.235 vvm   Right: 500 rpm - 0.705 vvm; white rectangle depicts the complete bubble measurement area. ....	16
Figure 2.3 A full cycle of oxygen concentration data collection, showing the portion used for mass transfer calculations.....	19
Figure 2.4 Sample linear plot for calculation of $k_{LA}$ for five of the cases studied in this work. ....	25
Figure 2.5 Comparison of individual measured bubble dimensions for non-rotating cases against bubble column data (Akita and Yoshida, 1974). ....	27
Figure 2.6 Normalized bubble size ( $d_{32}/(r_o-r_i)$ ) calculated using the correlation of Eq. (2.13) versus the measured values using Eq. (2.10). ....	29
Figure 2.7 Probability density function of the Sauter diameter of bubbles ( $d_s$ ) using Eq. (2.9) and comparison against log-normal distribution. ....	30
Figure 2.8 Comparison of measured and calculated Sherwood number. ....	32
Figure 2.9 Volumetric mass transfer coefficient versus azimuthal Reynolds number at moderate to high axial Reynolds numbers compared with data for a horizontal Taylor-Couette reactor with co-flow of phases (Dłuska et al., 2001).....	35
Figure 2.10 Measured gas holdup versus gas flow rate for an annular bubble column (no cylinder rotation).....	37
Figure 2.11 Comparison of Sherwood vs Galilei numbers for annular and cylindrical bubble columns (Akita and Yoshida, 1974). ....	38

Figure 3.1 Taylor-Couette vortex reactor (Ramezani et al., 2015).....	45
Figure 3.2 Sample bubble images in reactor. Left: Using sparger stone in absence of alcohol   Right: Using sparger stone in presence of alcohol. ....	49
Figure 3.3 Sample bubble image showing major and minor axis measurements. ....	51
Figure 3.4 A full cycle of oxygen concentration data collection. Circles show the portion used for mass transfer calculations. ....	52
Figure 3.5 Probability density of bubble Sauter diameter for several measured cases.....	53
Figure 3.6 Effect of surface tension on Sauter mean bubble diameter. ....	54
Figure 3.7 Performance of the bubble Sauter diameter correlation. ....	56
Figure 3.8 Effect of surface tension on average ellipticity. ....	57
Figure 3.9 Comparison of volumetric mass transfer coefficient in terms of gas flow rate (Ramezani et al., 2015). ....	58
Figure 3.10 Comparison of volumetric mass transfer coefficient in terms of rotational speed (Ramezani et al., 2015). ....	59
Figure 3.11 Effect of surface tension on mass transfer coefficient.....	60
Figure 3.12 Performance of the mass transfer correlation. ....	61
Figure 4.1 Illustration of the relationships between volumetric mass transfer coefficient and various geometric, operational, and hydrodynamic parameters.....	66
Figure 4.2 Configuration of a Taylor vortex reactor.....	67
Figure 4.3 Schematic of Taylor–Couette bioreactor used for mass transfer experiments (Ramezani et al., 2015). ....	80

Figure 4.4 Axially averaged radial distributions of (a) volumetric mass transfer coefficient (1/s <sup>1</sup> /s), (b) gas volume fraction, (c) slip velocity (m/s), and (d) turbulence dissipation rate (m <sup>2</sup> /s <sup>3</sup> ) for rotation speed and gas flow rate of 300 rpm and 0.235 vvm, respectively. ....	83
Figure 4.5 Comparison of predicted average volumetric mass transfer rate by different mass transfer models with experimental data under different rotational speeds. ....	85
Figure 4.6 Comparison of predicted average volumetric mass transfer rate by different mass transfer models with experimental data under different inlet gas flow rates. ....	86
Figure 4.7 Comparison of simulated instantaneous liquid phase oxygen concentration with experimental data of a specific case (0.235 vvm, 300 rpm) at an axial location of 12.7 cm from the bottom of the reactor and near the outer cylinder wall. ....	87
Figure 4.8 Global slip velocity as a function of inlet gas flow rate and cylinder rotation speed. ....	90
Figure 4.9 Global turbulent dissipation rate as a function of inlet gas flow rate and cylinder rotation speed. ....	91
Figure 4.10 Comparison of simulated volume averaged gas holdup with experimental data for the case of no cylinder rotation. ....	92
Figure 4.11 Predicted global volume averaged gas fraction as a function of inlet gas flow rate and rotational speed. ....	94
Figure 4.12 Contour plots of (a) mass transfer coefficient $k_L$ (m/s) predicted by the adaptive mode and (b) specific interfacial area $a$ (m <sup>2</sup> /m <sup>3</sup> ) for a gas flow rate of 0.235 vvm and cylinder rotation speed of 300 rpm. In each plot, the inner cylinder wall is represented by the bottom boundary and the outer cylinder wall is represented by the top boundary. ....	96

Figure 4.13 Predicted average mass transfer coefficients by the adaptive mass transfer model under different rotational speeds and inlet gas flow rates.....	97
Figure 4.14 Predicted specific interfacial area as a function of cylinder gas flow rate and cylinder rotation speed.....	98
Figure 5.1 schematic of the experimental setup. Left: Details of the test section, Right: Flow loop. ....	105
Figure 5.2 Comparison of velocity profile in developing duct flow.....	108
Figure 5.3 Comparison of the interpolated velocity field with individual data fields for $Re_d=100$ . The lines represent the PR-DNS data and the contour plots represent the experimental data. ....	109
Figure 5.4 Experimental velocity field around a train of particles for $Re_d=100$ at different arrangements. ....	111
Figure 5.5 Spatio-temporal Average of flow between the spheres for different cases. ....	112
Figure 5.6 Stream-wise velocity profile on the centerline between the first and second spheres.....	114
Figure 5.7 Stream-wise velocity profile on the centerline downstream the last sphere. ....	115
Figure 5.8 Stream-wise velocity profile on the centerline downstream the last sphere. ....	116
Figure 5.9 Stream-wise velocity profile on the centerline downstream the last sphere. ....	117
Figure 6.1 Schematic of the experimental setup. Left: Details of the test section, Right: Flow loop. ....	122
Figure 6.2 Accuracy of numerical results ( $D_m=D/dx=90$ ) and analytical solution along the central line in the cross section of the duct. ....	128

Figure 6.3 Convergence of FD formulations in the duct flow using the $L_2$ -norm of the error.....	128
Figure 6.4 Drag coefficient ( $C_D$ ) for flow past a fixed sphere at various Reynolds numbers. The circles represent the numerical results from standard drag coefficient from Clift et al. (Clift et al., 2005).....	129
Figure 6.5 Comparison of centerline velocity development in duct flow.....	131
Figure 6.6 Comparison of velocity profile in developing duct flow.....	131
Figure 6.7 Comparison of the single sphere case at $Re_d=85$ . The line contours represent the experimental data and the color contours represent the numerical PR-DNS data. ....	133
Figure 6.8 Comparison of axial velocity profile along the axial lines for a sphere at $Re_d=85$ . The lines represent the PR-DNS data and the symbols represent the experimental data. ....	134
Figure 6.9 Comparison of axial velocity profile along the transverse lines for one sphere at $Re_d=85$ . The lines represent the PR-DNS data and the symbols represent the experimental data. ....	134
Figure 6.10 Experimental velocity field around a train of 5 particles overlaid on contour plots of velocity magnitude for $Re_d=100$ . Top: $l/D_p = 1.38$ , Bottom: $l/D_p = 2.19$ .....	136
Figure 6.11 Contour plot of velocity comparing the interpolated velocity field with that of individual cameras. Top: Streamwise velocity, Bottom: Cross-stream velocity.....	137
Figure 6.12 Three dimensional streamlines for train of five particles using PR-DNS results. ....	138
Figure 6.13 Comparison of the contours of velocity components between simulation (color) and experiment (line) for $l/D_p = 1.38$ .....	139

Figure 6.14 Comparison of the contours of velocity components between simulation (color) and experiment (line) for $l/D_p = 2.19$ .....	140
Figure 6.15 Comparison of axial velocity profile along axial lines at different transverse locations for train of 5 spheres at $l/D_p = 1.38$ . The lines represent the PR-DNS data and the symbols represent the experimental data. ....	142
Figure 6.16 Comparison of axial velocity profile along axial lines at different transverse locations for train of 5 spheres at $l/D_p = 2.19$ . The lines represent the PR-DNS data and the symbols represent the experimental data. ....	142
Figure 6.17 Streamwise velocity profile along transverse lines along the center of particles at $l/D_p = 1.38$ . The lines represent the PR-DNS data and the symbols represent the experimental data. ....	143
Figure 6.18 Streamwise velocity profile along transverse lines along the center of particles at $l/D_p = 2.19$ . The lines represent the PR-DNS data and the symbols represent the experimental data. ....	144
Figure 6.19 Streamwise velocity profile along transverse lines along middle of the first and last pair of spheres at $l/D_p = 1.38$ . The lines represent the PR-DNS data and the symbols represent the experimental data. ....	145
Figure 6.20 Streamwise velocity profile along transverse lines along middle of the first and last pair of spheres at $l/D_p = 2.19$ . The lines represent the PR-DNS data and the symbols represent the experimental data. ....	145
Figure 6.21 Streamwise velocity profile along transverse lines downstream the particle train of 5 spheres at $l/D_p = 1.38$ . The lines represent the PR-DNS data and the symbols represent the experimental data. ....	146

Figure 6.22 Streamwise velocity profile along transverse lines downstream the particle train of 5 spheres at $l/D_p = 2.19$ . The lines represent the PR-DNS data and the symbols represent the experimental data. ....	147
Figure 6.23 Comparison of transverse velocity profile along axial lines at different transverse locations for train of 5 spheres at $l/D_p = 1.38$ . The lines represent the PR-DNS data and the symbols represent the experimental data. ....	148
Figure 6.24 Comparison of transverse velocity profile along axial lines at different transverse locations for train of 5 spheres at $l/D_p = 2.19$ . The lines represent the PR-DNS data and the symbols represent the experimental data. ....	149

## LIST OF TABLES

Table 2.1 Comparison of mean bubble diameter values using different definitions, 300 rpm - 0.470 vvm. All values are in mm. ....	23
Table 2.2 Sauter mean bubble diameters measured for different cases. ....	26
Table 2.3 Measured values of $k_{La}$ [ $s^{-1}$ ] calculated for different experimental conditions at axial location of 12.7 cm. ....	31
Table 3.1 Properties of Ethanol-Water mixture. ....	50
Table 4.1 Constitutive relations for bubbly Taylor–Couette two-fluid model (Gao et al., 2015b, 2013). ....	72
Table 4.2 Constants in bubbly Taylor–Couette two-fluid model (Gao et al., 2015b). ....	72

## NOMENCLATURE

## Roman

$C$	Concentration [mg/L]
$d$	Bubble diameter [mm]
$D$	Diffusion coefficient [ $\text{m}^2/\text{s}$ ]
$E$	Ellipticity of spheroid
$g$	Gravitational acceleration [ $\text{m}/\text{s}^2$ ]
$h$	Axial distance from the bottom of reactor [m]
$k$	Volumetric mass transfer coefficient [m/s]
$l$	Spheroid major diameter [m]
$m$	Spheroid minor diameter [m]
$N$	Impeller (inner cylinder) rotational speed [rev/s]
$Q$	Volumetric flow rate [L/min]
$r_i$	Outer radius of the inner cylinder [m]
$r_o$	Inner radius of the outer cylinder [m]
$u$	Superficial velocity [m/s]
$a$	specific gas–liquid interfacial surface area [ $\text{m}^{-1}$ ]
$c_l$	liquid molar concentration [ $\text{kmol}/\text{m}^3$ ]
$c_{l*}$	liquid saturation molar concentration [ $\text{kmol}/\text{m}^3$ ]
$C_D$	drag coefficient
$d_b$	sauter mean diameter of bubble [m]
$D_L$	diffusion coefficient gas in liquid [ $\text{m}^2/\text{s}$ ]
$E_o$	Eötvös number

$H$	Henry's law constant [Pa.m <sup>3</sup> /kmol]
$F$	interphase force [kg/m <sup>2</sup> s <sup>2</sup> ]
$g$	gravitational acceleration [m/s <sup>2</sup> ]
$G_k$	generation of turbulent kinetic energy [kg/m.s <sup>3</sup> ]
$G_\omega$	generation of specific dissipation rate [kg/m <sup>3</sup> s <sup>2</sup> ]
$k_l$	turbulent kinetic energy of liquid [m <sup>2</sup> /s <sup>2</sup> ]
$k_L$	liquid side mass transfer coefficient [m/s]
$L$	cylinder height [m]
$M_{wi}$	molecular mass [kg/kmol]
$p$	pressure [Pa]
$r$	cylinder radius [m]
$R_{gl}^i$	rate of gas-liquid mass transfer of species $i$ [kmol/m <sup>3</sup> s]
$Re_b$	bubble Reynolds number
$Re_a$	axial Reynolds number
$Re_\theta$	azimuthal Reynolds number
$S$	net rate of production/destruction [kmol/m <sup>3</sup> s]
$Sh$	Sherwood number
$t_e$	exposure time [s]
$u$	velocity [m/s]
$Y_i$	mass fraction of specie of species $i$
$Y_k$	dissipation of turbulent kinetic energy [kg/m.s <sup>3</sup> ]
$Y_\omega$	dissipation of specific dissipation rate [kg/m <sup>3</sup> s <sup>2</sup> ]

## Greek

$\Gamma$	Reactor aspect Ratio ( $\Gamma=h/(r_o-r_i)$ )
$\varepsilon_G$	Gas holdup
$\eta$	Reactor radius ratio ( $\eta=r_i/r_o$ )
$\omega$	Rotational speed of the inner cylinder [rad/s]
$\nu$	Kinematic viscosity [ $\text{m}^2/\text{s}$ ]
$\alpha$	volume fraction
$\varepsilon$	turbulence dissipation rate [ $\text{m}^2/\text{s}^3$ ]
$\omega$	specific dissipation rate [ $\text{s}^{-1}$ ]
$\nu$	kinematic viscosity [Pa.s]
$\mu_t$	turbulent viscosity [Pa.s]
$\rho$	density [ $\text{kg}/\text{m}^3$ ]
$\bar{\tau}$	phase stress tensor [ $\text{N}/\text{m}^2$ ]
$\bar{\tau}^{\text{Re}}$	phase stress tensor [ $\text{N}/\text{m}^2$ ]
$\Gamma$	aspect ratio
$\eta$	radius ratio

## Subscript

$a$	Axial
$b,s$	Bubble surface equivalent
$b,v$	Bubble volume equivalent
$i$	Inner cylinder
$G$	Gas
$L$	Liquid

- o* Outer cylinder
- s* Sauter mean
- $\Theta$  Azimuthal
- b* bubble phase
- l* liquid phase
- g* gas or global
- i* species index

Superscript

- \* Saturation

## ACKNOWLEDGMENTS

I would like to thank my advisor and committee chair, Michael G. Olsen, and my committee members, Shankar Subramaniam, Dennis Vigil, Ted Heindel, and Rodney Fox, for their guidance and support throughout the course of this research.

In addition, I would also like to thank my friends, colleagues, the department faculty and staff for making my time at Iowa State University a wonderful experience.

I acknowledge the National Science Foundation (CBET-1034307 and CBET-1236676) for partially supporting this research.

## ABSTRACT

Multiphase flow systems occur in a variety of industrial applications and are prevalent in nature. The focus of this dissertation is on experimental investigation of such flows in laboratory scale setups for the purpose of better understanding the fundamentals, validation of numerical simulations and models, and derivation of correlations for practical applications.

Two major types of flow were studied including a gas-liquid two phase flow inside a Taylor-Couette vortex reactor and a solid-liquid flow of water flow around a train of solid spherical particles inside a square duct. For the Taylor-Couette system, characterization of mass transfer from gas into liquid phase was the main focus. In addition, the size and shape of the bubbles were measured and observed in order to quantify the mass transfer coefficient. This was followed up with the study of the effect of interfacial tension on the system using ethyl alcohol as a surfactant.

The duct flow around a train of particles was studied in order to enable observation of the interaction between arrangements of particles and the flow field. The velocity field data from Particle Image Velocimetry (PIV) experiments served as a validation case for Particle-Resolved Direct Numerical Simulation (PR-DNS). The number of spheres in the train arrangement was varied as well as their distance. The work performed for the two different setups are separately introduced in the following.

## CHAPTER 1

### INTRODUCTION

Multiphase flow systems occur in a variety of industrial applications and are prevalent in nature. The focus of this dissertation is on experimental investigation of such flows in laboratory scale setups for the purpose of better understanding the fundamentals, validation of numerical simulations and models, and derivation of correlations for practical applications.

Two major types of flow were studied including a gas-liquid two phase flow inside a Taylor-Couette vortex reactor and a solid-liquid flow of water flow around a train of solid spherical particles inside a square duct. For the Taylor-Couette system, characterization of mass transfer from gas into liquid phase was the main focus. In addition, the size and shape of the bubbles were measured and observed in order to quantify the mass transfer coefficient. This was followed up with the study of the effect of interfacial tension on the system using ethyl alcohol as a surfactant.

The duct flow around a train of particles was studied in order to enable observation of the interaction between arrangements of particles and the flow field. The velocity field data from Particle Image Velocimetry (PIV) experiments served as a validation case for Particle-Resolved Direct Numerical Simulation (PR-DNS). The number of spheres in the train arrangement was varied as well as their distance. The work performed for the two different setups are separately introduced in the following.

### 1.1 Taylor-Couette Gas-Liquid Vortex Reactor Mass Transfer

Mass transfer in gas-liquid agitated vessels is a problem with important industrial applications and it has been studied extensively. Interphase mass transfer is a key component in design, scale-up and optimization of several multiphase chemical and biological reactors. Various types of reactors such as bubble columns (Behkish et al., 2007; Calderbank and Lochiel, 1964; Heijnen et al., 1984; Linek et al., 2005b; Dale D McClure et al., 2015; Pittoors et al., 2014; Vasconcelos et al., 2003), stirred tanks (Bouaifi et al., 2001; Hassan et al., 2012; Kapic and Heindel, 2006; Labík et al., 2014; Schlüter and Deckwer, 1992; Ungerman and Heindel, 2007), and different wall-driven gas-liquid reactors (Baier et al., 2000; Haut et al., 2003; Hubacz and Wroński, 2004; Nemri et al., 2014) are typically used for such applications.

Liquid side mass transfer resistance at gas–liquid interfaces is usually assumed to limit the interphase mass transport, and hence, gas side mass transfer resistance is neglected (Deckwer et al., 1974). Therefore, the liquid side volumetric mass transfer coefficient ( $k_{La}$ ) is used to compute the overall mass transfer rate across a gas–liquid interface. Most of the mass transfer studies have focused on bubble columns (Asgharpour et al., 2010; Chen et al., 2013; Garcia-Abuin et al., 2013; Jia et al., 2015; Koide et al., 1985; Vázquez et al., 2000), although various other reactors have also been considered (Benedek and Heideger, 1971; Moraveji et al., 2012; van der Meer et al., 1992; Zhang et al., 2013). Many studies have focused of developing experimental correlations for calculation of interphase mass transfer coefficients (Baier et al., 2000; Dłuska et al., 2001; Garcia-Ochoa and Gomez, 2005; Hill, 2006; Strong and Carlucci, 1976; Wongsuchoto et al., 2003a) and proposing reliable numerical models for simulation of interphase mass transfer (Huang et al., 2010; Wang and Wang, 2007). Several factors including gas holdup and bubble size, slip velocity, and turbulent energy dissipation

rate affect the mass transfer coefficient which depends on other factors such as reactor operating conditions, geometry, and physical properties of the gas and liquid phases.

Taylor vortex flow occurs in the annular space between two concentric cylinders, with a rotating inner cylinder and a fixed outer cylinder. The instabilities and flow patterns produced in this canonical flow geometry have been studied extensively (Andereck et al., 1986; Bilson and Bremhorst, 2007; Dong, 2007; Donnelly, 1991; Fenstermacher et al., 1979; Lathrop et al., 1992; Pirrò and Quadrio, 2008; Puddjiono et al., 1992; Swinney, 1978; Taylor, 1923; Wang et al., 2005a; Wereley and Lueptow, 1999, 1998). As the rotation speed of inner cylinder increases above a critical value, the fluid undergoes transition from laminar Couette flow (circular flow with only an azimuthal component) to laminar Taylor vortex flow and then higher order instabilities such as wavy vortex flow, modulated wavy vortex flow, and turbulent Taylor vortex flow (Andereck et al., 1986; Coles, 1964; Wang et al., 2005a, 2005b). Such flow patterns are used in applications such as water purification (Dutta and Ray, 2004), emulsion polymerization (Imamura et al., 1993; Kataoka et al., 1995), liquid-liquid extraction (Baier et al., 2000; Davis and Weber, 1960), pigment preparation (Kim et al., 2014), photocatalysis (Sczechowski et al., 1995), culture of animal cells (Haut et al., 2003; Qiao et al., 2014b; Sorg et al., 2011), and cultivation of microalgae (Brown et al., 1964; Kliphuis et al., 2010; Kong and Vigil, 2014; Kong et al., 2013; Oasmaa et al., 2009).

Although single phase Taylor vortex flow has been thoroughly studied over many years, multiphase Taylor vortex flow is relatively less understood specially with respect to mass transport. Introduction of a second fluid phase into a Taylor vortex reactor causes different instabilities and flow patterns to arise (Baier and Graham, 2000; Campero and Vigil, 1999, 1997; Dłuska et al., 2004, 2001; Joseph and Preziosi, 2006; Joseph et al., 1984; Kadam

et al., 2008; Renardy and Joseph, 1985; Wroński et al., 1999; Zhu and Vigil, 2001a; Zhu et al., 2000) and addition of a second gas phase reduce the drag on the rotating inner cylinder (Chouippe et al., 2014; Maryami et al., 2014; van Gils et al., 2013; Van Gils et al., 2011). Some researchers have studied such gas-liquid interactions in Taylor-Couette flows recently (Djeridi et al., 2004; Dłuska et al., 2004, 2001; Hubacz and Wroński, 2004; Wroński et al., 2005, 1999). Most studies on development of empirical correlations for gas-liquid mass transfer have focused of other types of reactors such as bubble columns (Colombet et al., 2011; Gourich et al., 2006; Kawase et al., 1987; Muroyama et al., 2013), airlift reactors (Cockx et al., 2001; Huang et al., 2010; Kawase and Hashiguchi, 1996), and stirred tanks (Garcia-Ochoa and Gomez, 2005, 2004; García-Ochoa and Gómez, 1998; Özbek and Gayik, 2001a). There is even far less information available for simulation of interphase mass transport in two-phase Taylor-Couette flow with no previous model specifically developed for such systems.

Many factors such as presence of impurities, additives, or surfactants influence mass transfer in a gas-liquid system and the effect of surfactant has been widely studied (D. Gomez-Diaz et al., 2009; Diego Gomez-Diaz et al., 2009; Hebrard et al., 2009; Jamnongwong et al., 2010; Özbek and Gayik, 2001b; Sardeing et al., 2006). Interfacial surface tension between gas bubbles and the continuous liquid phase affects mass transfer (Belo et al., 2011; Chen et al., 2013; Sardeing et al., 2006), bubble size (Alves et al., 2002; Dumont et al., 2006; Gomez-Diaz et al., 2008; Jordan and Schumpe, 2001; Painmanakul et al., 2005) and coalescence and breakup of bubbles (Anastasiou et al., 2010; Chern et al., 2001; Sch et al., 2002; Walter and Blanch, 1986). It is reported that addition of surfactant generally increases the specific interfacial surface area,  $a$ , by reducing the size of bubbles (Chaumat et al., 2007; Garcia-Abuin et al., 2012, 2010; D. Gomez-Diaz et al., 2009; Hebrard et al., 2009; Özbek and Gayik, 2001b),

causes a higher gas holdup (Hur et al., 2014), and reduces the liquid side mass transfer coefficient,  $k_L$ , (Belo et al., 2011; McClure et al., 2014). The gas-liquid mass transfer rate gets affected by both the  $k_L$  and  $a$  reversely. It is generally expected that addition of a surfactant has a much larger impact on interfacial surface area, and therefore the value of  $k_L a$  increases with introduction of additives (Asgharpour et al., 2010; Benedek and Heideger, 1971). Examples of such surfactants in aqueous systems include alcohol (Anastasiou et al., 2010; Dumont et al., 2006; Garcia-Abuin et al., 2010; Hur et al., 2014; Jordan and Schumpe, 2001; McClure et al., 2015), glycerol (Özbek and Gayik, 2001b), the Tween family (Belo et al., 2011; Diego Gomez-Diaz et al., 2009), sodium sulphite solution (Linek et al., 2005a, 2004), ionic surfactants (Moraveji et al., 2012), and various sugars (Chern et al., 2001; Dale D. McClure et al., 2015).

Three separate articles are presented here describing the development of empirical correlations for bubble size and volumetric interphase mass transfer coefficients in CHAPTER 2, studying the effect of surfactant on bubble size and mass transfer coefficient in CHAPTER 3, and proposing a computational approach for calculating mass transfer by selecting appropriate models in CHAPTER 4. For a fixed reactor geometry (cylinder radii and length), the mass transfer coefficient and droplet diameter are found as functions of axial and azimuthal Reynolds numbers. Empirical correlations are proposed for calculation of these parameters and the results are then compared with similar correlations for bubble columns, horizontal Taylor-Couette reactors, and stirred tanks. Subsequently, the results are extended to include the effect of interfacial surface tension on the volumetric liquid side mass transfer coefficient as well as the size distribution and shapes of bubbles in the same reactor and it is shown that the results depend on the Capillary number as well. In addition, numerical simulation of this system is presented and interphase mass transfer coefficient is calculated by integrating local fluid

velocity and phase distribution information using well-known theoretical models for interfacial mass transport. Finally, the proposed numerical method is validated using the existing experimental results.

## 1.2 Flow Field Investigation around a Train of Particles in a Square Duct

Multiphase flow occurs in various industrial applications and are abundant in nature. The study of the micro scale of multiphase flow systems is necessary for developing a fundamental understanding of this relatively complex phenomenon. Particularly, two-phase fluid-solid flow is encountered in a variety of industrial applications (Dai and Grace, 2010; Wang et al., 2004). Several interesting aspects of these systems such as the effects of fluid phase hydrodynamics on the aggregation and dispersion of solid particles (Koch and Brady, 1985; Lim et al., 1995; Mehrabadi et al., 2015), the properties of the solid phase such as elasticity and friction (Mehrabadi et al., 2016a), electrostatic charges and surface properties of particles (Royer et al., 2009), and effects of the shape of the solid phase particles (Siewert et al., 2014) have been studied in fluid-solid two-phase systems.

Various studies have been performed in order to provide a better understanding of multiphase flow systems using theoretical analysis (Koch and Brady, 1985; Schlichting and Gersten, 1979), experimental measurement (Bachalo, 1994; Dai and Grace, 2010; Tsuji et al., 2003), and numerical simulation (Fox, 2014, 2012; Van Wachem and Almstedt, 2003). Several operating parameters such as flow rate, pressure drop, bed height, particle carry-over, clustering or preferential accumulation, fluid entrainment, and particle attrition are typically required for a successful design. Most of the studies in this area consider porous media or a fixed or fluidized bed (Tang et al., 2016; Wang et al., 2004). Clustering of particles is also of particular interest in such flow systems (Capecelatro et al., 2014). Previous studies have

investigated fluid flow around different arrangements of spherical solid particles based on drag force measurement (Liang et al., 1996; Zhu et al., 1994), numerical investigation of flow around multiple spheres (Jadoon et al., 2010; Maheshwari et al., 2006; Prah et al., 2009, 2007; Tsuji et al., 2003), and experimental field measurement of similar geometries (Chen and Wu, 2000; Ozgoren, 2013; Pinar et al., 2013; Tsuji et al., 1982).

Heat and mass transfer between the two phases and possibly chemical reactions in either or both phases occur in many industrial application of multiphase flow (Chen et al., 1997; Sun et al., 2016, 2015; Tenneti et al., 2013) and a fundamental understanding of the hydrodynamics in such flow systems is crucial for correctly predicting other aspects of these flows. Understanding the mesoscale and microscale phenomena involves studying the interaction of the dispersed phase with the continuous phase and also the dispersed phase interactions in the presence of the continuous phase. In the context of solid-fluid two phase flows, there are several studies that are used as benchmark for validation of numerical simulations that involve flow around single bluff bodies (Achenbach, 1974; Sakamoto and Haniu, 1995; Sakamoto et al., 1990, 1989; Taneda S, 1956; Taneda, 1959), or some cases with flow around multiple bodies (Ergun and Orning, 1949; Tsuji et al., 1982) and numerical models can be validated against the results of such studies.

A successful simulation requires appropriate closure models that can possibly be provided using experiments and analytical modeling. However, the complex nature of these flows makes these approaches challenging and experimental investigations in specific, are inherently difficult due to the presence of the particles that inhibits access and hinders data collection from inside the bed. This causes many of the small scale phenomena occurring inside the flow to be not traceable directly and only local and average readings are available. In

contrast, very detailed information can be acquired using Direct Numerical Simulation (DNS) of such flows and if simulated appropriately, can provide the necessary data to develop and validate closure models (Mehrabadi et al., 2015; Sun et al., 2015; Tang et al., 2016; Tenneti and Subramaniam, 2014; Tenneti et al., 2013, 2011, 2010). It is of utmost importance that these simulations are carefully validated and recent flow visualizations methods such as Particle Image Velocimetry (PIV) are great candidates for this purpose. PIV allows for practically non-intrusive measurement of the velocity field in contrast to point measurements using other methods that provides plenty of data for validation. Recently, several studies have been done by different researchers in a variety of geometries (Chen and Wu, 2000; Johnson and Patel, 1999; Liang et al., 1996; Maheshwari et al., 2006; Ozgoren, 2013; Ozgoren et al., 2014, 2013, 2011; Pinar et al., 2013; Prahl et al., 2007; Tsuji et al., 2003, 1982; Zhu et al., 1994).

Two separate articles are presented here describing the experimental study of flow around a train of particles in CHAPTER 5 and a comparison with numerical simulation for some of the studied cases in CHAPTER 6. A simplified case of a train of successive spherical solid particles inside a liquid flowing medium confined in a square duct is experimentally studied and results are presented. These results are of particular interest in validating multiphase flow models and also for developing a fundamental understanding of the interaction of the distributed and the continuous phases in such flows. A Particle Resolved DNS (PR-DNS) simulation method is introduced and validated using experimental data. This simulation method is capable of providing numerical correlations for the drag coefficient, Nusselt number, and Schmidt number along with closure models for pseudo turbulent terms in the Favre-averaged continuum equations.

## CHAPTER 2

EXPERIMENTAL MEASUREMENT OF OXYGEN MASS TRANSFER AND BUBBLE  
SIZE DISTRIBUTION IN AN AIR-WATER MULTIPHASE TAYLOR-COUPETTE  
VORTEX BIOREACTOR

This chapter is an article published in Chemical Engineering Journal (Ramezani et al., 2015). I am the main contributor to this work.

## 2.1 Abstract

Experimental measurements of the volumetric liquid mass transfer and bubble size distribution in a vertically oriented semi-batch gas-liquid Taylor-Couette vortex reactor with radius ratio  $\eta=r_i/r_o=0.75$  and aspect ratio  $T=h/(r_o-r_i)=40$  were performed, and the results are presented for axial and azimuthal Reynolds number ranges of  $Re_a=11.9-143$  and  $Re_\theta=0-3.5\times 10^4$ , respectively. Based on these data, power-law correlations are presented for the dimensionless Sauter mean diameter, bubble size distribution, bubble ellipticity, and volumetric mass transfer coefficient in terms of relevant parameters including the axial and azimuthal Reynolds numbers. The interaction between wall-driven Taylor vortices and the axial passage of buoyancy-driven gas bubbles leads to significantly different dependencies of the mass transfer coefficient on important operating parameters such as inner cylinder angular velocity and axial superficial gas velocity than has been observed in horizontally oriented gas-liquid Taylor vortex reactors. In general, the volumetric mass transfer coefficients in vertical Taylor vortex reactors have a weaker dependence upon both the axial and azimuthal Reynolds numbers and are smaller in magnitude than those observed in horizontal Taylor vortex reactors or in stirred tank reactors. These findings can be explained by differences in the size and spatial

distribution of gas bubbles in the vertically oriented reactor in comparison with the other systems.

## 2.2 Introduction

Gas-liquid mass transfer in agitated vessels is a problem with important industrial applications, and consequently it has been studied extensively, including the development of correlations for volumetric mass transfer coefficients. While most such studies have concentrated on stirred tanks (Bouaifi et al., 2001; Kopic and Heindel, 2006; Schlüter and Deckwer, 1992; Ungerman and Heindel, 2007) or bubble columns (Behkish et al., 2007; Calderbank and Lochiel, 1964; Linek et al., 2005b; Vasconcelos et al., 2003), relatively few investigations have considered mass transfer in wall-driven gas-liquid flows. In this work, a mass transfer correlation is developed for semi-batch gas-liquid Taylor vortex flow wherein fluid motion is driven by the rotation of a cylinder and by axial passage of buoyant gas bubbles.

Taylor vortex flow occurs in the annular space between two concentric cylinders, with a rotating inner cylinder and a fixed outer cylinder, as shown in Figure 2.1. The flow patterns and instabilities produced in this canonical flow geometry have been extensively studied over the course of many decades (Andereck et al., 1986; Bilson and Bremhorst, 2007; Dong, 2007; Donnelly, 1991; Lathrop et al., 1992; Pirrò and Quadrio, 2008; Pudjiono et al., 1992; Swinney, 1978; Taylor, 1923; Wang et al., 2005a; Wereley and Lueptow, 1999, 1998), and Taylor vortex flow patterns have been used in many varied applications such as water purification (Dutta and Ray, 2004), emulsion polymerization (Imamura et al., 1993; Kataoka et al., 1995), liquid-liquid extraction (Baier et al., 2000; Davis and Weber, 1960), pigment preparation (Kim et al., 2014), photocatalysis (Sczechowski et al., 1995), culture of animal cells (Haut et al., 2003), and cultivation of microalgae (Brown et al., 1964; Kong and Vigil, 2014; Kong et al., 2013;

Oasmaa et al., 2009). Nevertheless, despite the sustained and significant attention that Taylor vortex flow has received and the multiphase nature of many of its applications, multiphase Taylor-Couette flow remains relatively poorly understood.

The introduction of a second dispersed immiscible fluid phase in Taylor-Couette flow strongly impacts flow patterns and leads to many interesting phenomena. For example, if two immiscible liquids are fed continuously to a horizontally oriented Taylor vortex flow cell, a variety of spatial and spatiotemporal hydrodynamic structures arise (Baier and Graham, 2000; Campero and Vigil, 1999, 1997; Zhu and Vigil, 2001a). More recently it has been reported that the introduction of even a small amount of gas into a vertically oriented Taylor vortex flow cell results in dramatic drag reduction on the rotating inner cylinder and nontrivial gas bubble spatial distribution (Chouippe et al., 2014; Maryami et al., 2014; van Gils et al., 2013; Van Gils et al., 2011). Some recent studies have been performed in order to characterize these gas-liquid interactions in Taylor-Couette flows (Djeridi et al., 2004; Dłuska et al., 2004; Hubacz and Wroński, 2004; Wroński et al., 2005).

However, to our knowledge there exists no previous study of interphase gas-liquid mass transfer in a vertically oriented Taylor-Couette flow device. Dłuska *et al.* (Dłuska et al., 2004, 2001) have investigated gas-liquid mass transfer in a horizontal Taylor vortex reactor with continuous co-flow of both phases. They presented results of both physical and chemical absorption by studying the relationship between the volumetric mass transfer coefficient  $k_{La}$  and the dissipation energy of both axial and azimuthal flow.

In view of the existence of nontrivial flow patterns and phase distribution in a vertically oriented semi-batch gas-liquid Taylor vortex reactor, as well as its potentially important practical applications in biotechnology and other fields, the work presented here describes the

development of empirical correlations for bubble size and volumetric interphase mass transfer coefficients. The focus is on high azimuthal Reynolds numbers and gas flow rates that are likely to be relevant to industrial applications. It is shown for fixed reactor geometry (cylinder radii and length) that mass transfer coefficient and droplet diameter depend on both the axial and azimuthal Reynolds numbers. These results are then compared with similar correlations for bubble columns, horizontal Taylor-Couette reactors, and stirred tanks.

## 2.3 Experimental Methods

### 2.3.1 Apparatus

A drawing of the Taylor-Couette apparatus used in this investigation is shown in Figure 2.1. The rotating stainless steel inner cylinder has an outer radius of 3.81 cm and the fixed transparent acrylic outer cylinder has an inner radius of 5.08 cm, resulting in a gap width of 1.27 cm. The length of the reactor is 50.8 cm and the reactor is filled to a height of  $h = 48$  cm, hence the total working volume of liquid (deionized water) is 1.70 L. The corresponding radius ratio and aspect ratio of the apparatus are given by  $\eta = r_i/r_o = 0.75$  and  $\Gamma = h/(r_o - r_i) = 40$  respectively.

During each experiment the annulus was first filled with room temperature nitrogen-saturated deionized water. Although no specific measures were taken to control the fluid temperature, thermocouple measurements at the top of the reactor showed that after starting the rotation of the inner cylinder and allowing the system to reach a steady state, the working liquid temperature typically fluctuated less than 0.2 degrees during the duration of an experiment.

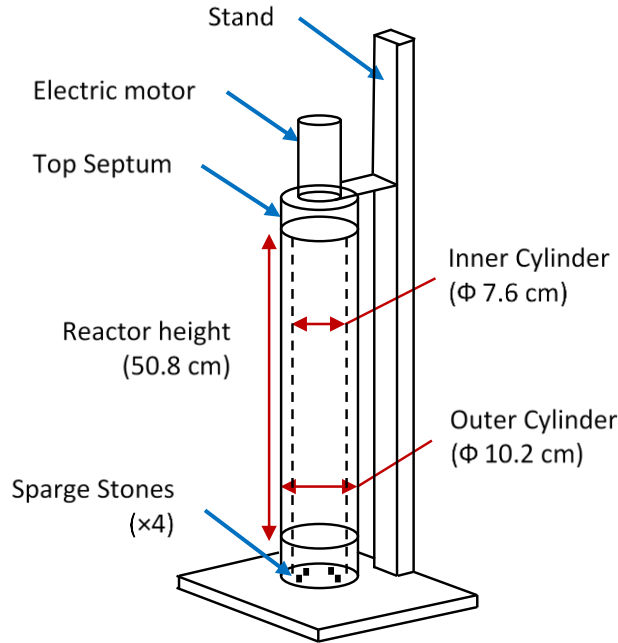


Figure 2.1 Taylor-Couette vortex reactor

The inner cylinder was rotated using a computer-controlled electric motor (Applied Motion STM series) mounted above the apparatus and connected to the inner cylinder with a center slotted-disc flexible shaft coupler (McMaster). Rotation rates of zero to 800 rpm with increments of 100 rpm were studied in this experiment, producing azimuthal Reynolds numbers, defined as:

$$Re_{\theta} = \frac{r_i \omega_i (r_o - r_i)}{\nu_L} \quad (2.1)$$

up to  $3.5 \times 10^4$ . For single phase flow, this range is well within the turbulent Taylor vortex flow regime (Andereck et al., 1986).

Gas was continuously fed to the reactor through four equally spaced sparger stones (Sure-Seal Miniature Muffler) mounted in the annular region of the bottom plate. Alicat gas flow rate controllers (MFC series) were used to control both the gas flow rate and the gas mixture composition to within 1% of set point values. Gases were derived from compressed

tanks and premixed before feeding to the reactor. In all experiments, the gas consisted of 79 mole percent nitrogen and 21 mole percent oxygen in order to approximate the composition of air, and to avoid variations in humidity. Total gas volumetric flow rates of 100 sccm to 1200 sccm were studied in this experiment with increments of 200 sccm. This corresponds to volumetric flow rates in the range of 0.059 vvm to 0.705 vvm. The axial Reynolds number was defined as:

$$Re_a = \frac{2u_G(r_o - r_i)}{\nu_L} \quad (2.2)$$

using the superficial gas velocity and the hydraulic diameter of the annulus. Axial Reynolds numbers ranged from 11.9 to 143, corresponding to superficial gas velocities of 0.47 mm/s to 5.64 mm/s. In the absence of cylinder rotation, these gas velocities correspond to the bubbly flow regime when compared to a bubble column with the same hydraulic diameter (Shah et al., 1982). A similar assumption leads to predicted gas holdups of approximately  $\varepsilon_G = 0.03$ -0.04 for the highest gas flow rate studied (Campero and Vigil, 1999). Over long periods of use and high gas flow rates, heating in the control valves can cause controllers to register unrealistically high gas temperatures, which in turn can affect flow rate accuracy. For this reason, the feed gas temperature was carefully monitored during each experiment to ensure that it remained constant, and in the few instances when the gas temperature did not remain constant, the experiment was aborted and the flow controllers were allowed to cool before another run was performed. Each experimental condition considered here was determined uniquely by the rotational speed of the inner cylinder (rpm) and the gas flow rate in vvm, volume gas flow per minute per liquid volume.

### 2.3.2 Bubble Size Measurements

Several investigators have measured bubble size in gas-liquid reactors (Akita and Yoshida, 1974; Behkish et al., 2007; Bouaifi et al., 2001; Polli et al., 2002). One method to measure bubble size is to extract a fluid sample and analyze the bubbles ex situ. Samples taken using this method vary in density, and there is a non-uniform distribution of pressure at the capillary entrance. In addition, the velocity of the gas and liquid phases are different, which results in biased selections of bubble size (Van't Riet, 1979). To avoid these problems, in this work an in-situ optical technique was used to measure bubble sizes. Specifically, digital photographs of the annulus were acquired using a Nikon DSLR camera equipped with an electronic flash and a zoom lens adjusted to a focal length of 31 mm. A shutter speed of 1/500 s and an aperture of f/14 were used to freeze bubble motion and to ensure that the depth of field was sufficient to produce sharp images, an example of which is shown in Figure 2.2. A 2 mm grid printed onto the outer surface of the rotating inner cylinder provided a reference length scale. Although curvature of the transparent outer cylinder results in refraction distortions, the grid provides a means for estimating the severity of this distortion. Bubbles appearing in the middle of each frame were essentially undistorted, and therefore only bubbles appearing in the mid frame region as designated in Figure 2.2 were measured.

Because the bubbles are ellipsoidal, bubble size was measured by counting pixels and using the calibration scale to determine major and minor axis lengths for each bubble. Due to the cylindrical shape of the reactor, the scale factors for the horizontal and vertical directions differed by 8%. Since the major and minor axes of the bubbles are inclined in most cases, an average of these two scales was used for all bubble orientations. For each experimental condition studied, 10 photographs were acquired from which at least 150 individual bubbles

were measured. Due to the rotational nature of the flow, it was assumed that consecutive images at a fixed axial location were representative of the azimuthal distribution of bubbles, and at least three images were processed for each case. In addition, for every processed image, bubbles from the bottom to the top of the reactor were measured, thereby providing a complete axial sample of bubbles.



*Figure 2.2 Sample bubble images including the measuring grid. Left: magnified view of bubble measurement zone / middle: 300 rpm - 0.235 vvm / Right: 500 rpm - 0.705 vvm; white rectangle depicts the complete bubble measurement area.*

Figure 2.2 shows sample bubble images and illustrates the bubble measuring procedure. The photograph in the middle is for a moderate rotation speed and gas flow rate, and individual bubbles can clearly be distinguished. On the left is a magnified portion of the same image showing major and minor axes of several bubbles marked with white lines. For experiments

performed with a combination of high rotation speed and gas flow rate, it is nearly impossible to discern individual bubbles due to presence of bubble swarms. The right panel in Figure 2.2 shows an image for the highest cylinder rotation speed (500 rpm) and gas flow rate (0.705 vvm) combination investigated for bubble size measurement, and the difficulty in distinguishing individual bubbles is apparent.

### 2.3.3 Mass Transfer Measurements

The rate of mass transport of oxygen from the gas to the liquid was determined from temporal dissolved oxygen measurements. Specifically, a minimally invasive oxygen sensing system (PreSens Fibox 4 transmitter and Pst3 sensor spots) was used to measure the time-dependent dissolved oxygen concentration in the deionized water at the inside surface of the transparent outer cylinder at several locations along the main axis of the reactor. The optical oxygen sensor system employs an external fiber optics laser probe to measure the oxygen concentration at small 5 mm diameter patches mounted flush with the inside of the stationary outer cylinder wall. In particular, four circular patches of 1 mm thickness were mounted on the inside surface at different axial distances of 5.1 cm, 12.7 cm, 25.4 cm, and 38.1 cm measured from the bottom of the reactor. The small size and thickness of these patches make them practically a non-intrusive means of measurement. The accuracy of the measured concentrations using this instrument is  $\pm 3\%$  for dissolved oxygen. The probe response time is less than 6 seconds, while the shortest mass transfer response time ( $1/k_{LA}$ ) measured was approximately 50 seconds.

Oxygen mass transfer experiments were performed using a dynamic method based on the measurement of the concentration of dissolved oxygen in water (Garcia-Ochoa and Gomez, 2009). A step change in the concentration of inlet gas results in a dynamic response in the

concentration of oxygen dissolved in the liquid phase, and these temporal concentration data are used to calculate a mass transfer coefficient. Experiments were performed for a gas flow rate range of 0.059 vvm to 0.705 vvm and rotation rates of up to 800 rpm, corresponding to axial Reynolds number ranging between 11.9 and 143 and azimuthal Reynolds numbers up to  $3.5 \times 10^4$ , respectively.

In a typical experiment, the annular reactor was filled with room temperature deionized water. Use of deionized water is important due to the fact that the presence of ions in water can reduce the average bubble size, which results in a larger specific interfacial area ( $a$ ) (Van't Riet, 1979). Subsequently, pure nitrogen gas was pumped through sparge stones (using a separate gas flow controller than the ones used for the simulated air) into the bottom of the reactor at a volumetric flow rate of 512 sccm without rotating the inner cylinder. During this oxygen displacement stage the dissolved oxygen concentration was monitored, and after it reached a minimum value of 0.15 mg/L, the flow of nitrogen was stopped and 5 minutes of rest time was elapsed to ensure that nitrogen bubbles exited the reactor.

After executing the oxygen purge procedure described above, the inner cylinder was accelerated to the desired rotation speed and flow of simulated air commenced at the chosen volumetric flow rate. The dissolved oxygen concentration was continually monitored throughout this process until it returned to the initial value (approximately 8 mg/L) measured before the oxygen purge began. Because the fluid flow does not respond instantaneously to the step changes in gas flow rate and cylinder rotation speed, the dissolved oxygen measurements obtained during the first 30 seconds after the simulated air is introduced into the reactor were omitted from calculations of the volumetric mass transfer coefficient.

A typical plot of the dissolved oxygen concentration versus time during the three steps described above (oxygen purge, no gas feed, and feed of simulated air) is shown in Figure 2.3. Also indicated is the portion of the data that was used for mass transfer calculations described in section 2.4.1 . At the end of data collection for a given experimental trial, the water was replaced before repeating the protocol described above for the next trial.

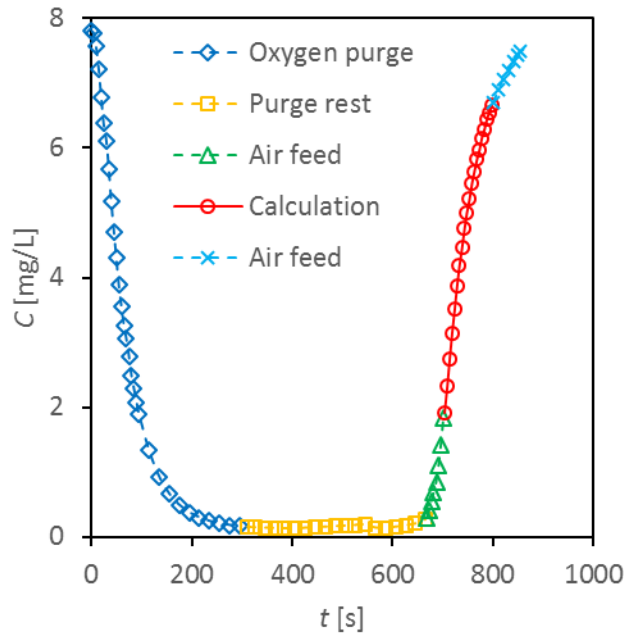


Figure 2.3 A full cycle of oxygen concentration data collection, showing the portion used for mass transfer calculations.

An attempt was made to quantify the variation of the mass transfer coefficient with reactor axial position by measuring  $k_{La}$  at four different axial locations for the five cylinder rotation/gas flow rate combinations of (0 rpm, 0.059 vvm), (100 rpm, 0.470 vvm), (200 rpm, 0.117 vvm), (300 rpm, 0.117 vvm), and (400 rpm, 0.352 vvm). It was observed from these experiments that the variation of  $k_{La}$  with axial position, with the exception of the location closest to gas inlet, was smaller than the accuracy of the measurements at a fixed axial position. For this reason, no further experiments were carried out at multiple axial positions and instead

the remaining data were collected at an axial position 12.7 cm above the gas feed, and these data were deemed sufficient to compute representative average reactor mass transfer coefficients.

## 2.4 Calculations

### 2.4.1 Bubble Size

It has been previously observed that for buoyancy-driven flows in the absence of agitation (for example in bubble columns), bubbles take on the shape of oblate spheroids (Polli et al., 2002; Popovic and Robinson, 1989). In such cases the bubble minor axis is aligned with the principle direction of their motion. In contrast, in the present case bubble motion is driven both by fluid shear generated by the rotating inner cylinder and by buoyancy. Even for the lowest azimuthal Reynolds numbers investigated, the azimuthal motion of bubbles is significant when compared to the axial distance of travel. Consequently, it is not surprising that photographs of bubbles in the Taylor vortex reactor show that bubble major axes are nearly horizontal. Furthermore, because the sheared bubbles have a distinctly ellipsoidal appearance with the major axis aligned horizontally with the azimuthal component of velocity, it is more appropriate to approximate their shapes as prolate spheroids rather than oblate spheroids, except in the case of no cylinder rotation. The recent work of Qiao *et al.* (Qiao et al., 2014a) also suggests that bubbles are stretched circumferentially in Taylor-Couette vortex flow, and at least one other investigation reported prolate bubbles in a vertical Taylor Couette reactor (van Gils et al., 2013).

In view of the above discussion and for the purpose of calculating bubble sizes, bubbles were assumed to be oblate in the absence of rotation of the inner cylinder whereas they were assumed to be prolate for cases with cylinder rotation. Specifically, the volume equivalent

bubble diameter was computed using Eqs. (2.3) and (2.4) for oblate and prolate spheroids, respectively.

$$d_{b,v}^{prolate} = \sqrt[3]{lm^2} \quad (2.3)$$

$$d_{b,v}^{oblate} = \sqrt[3]{l^2m} \quad (2.4)$$

where  $l$  is the major diameter of the spheroid and  $m$  is the minor diameter. Subsequently, the Sauter mean diameter for a population of bubbles is obtained from Eq. (2.5) (Asgharpour et al., 2010; Shah et al., 1982).

$$d_{s,v} = \frac{\sum d_{b,v}^3}{\sum d_{b,v}^2} \quad (2.5)$$

The above approach for computing the Sauter mean diameter assumes that bubble elongation, as determined by the ratio of the major to minor axis, is modest. However for non-spheroidal bubbles a more elaborate calculation of bubble diameter is possible as suggested by Muroyama *et al.* (Muroyama et al., 2013, 2012). Since in all cases studied here bubble elongation was significant (with maximum aspect ratios typically ranging from 2.5-4.0), the latter method was employed. This method requires calculation of the surface equivalent diameter using Eqs. (2.6) and (2.7), assuming prolate or oblate spheroids respectively (Weisstein, n.d.).

$$d_{b,s}^{prolate} = \sqrt{\frac{1}{2} \left( m^2 + \frac{lm}{E} \sin^{-1} E \right)} \quad (2.6)$$

$$d_{b,s}^{oblate} = \sqrt{\frac{1}{2} \left( l^2 + \frac{m^2}{2E} \ln \left( \frac{1+E}{1-E} \right) \right)} \quad (2.7)$$

Here, the ellipticity of a spheroid is calculated using:

$$E = \sqrt{1 - \frac{m^2}{l^2}} \quad (2.8)$$

where  $E$  is equal to one for the case of a sphere. Based on these definitions, it is possible to calculate a Sauter diameter for each individual bubble defined as:

$$d_s = d_{b,v}^3 / d_{b,s}^2 \quad (2.9)$$

These Sauter diameters were used for the calculation of the mean and standard deviation for the bubble size distribution presented in section 4. However, for the calculation of the Sherwood number, a Sauter mean diameter is used to represent the average bubble diameter, defined by:

$$d_{32} = \sum d_{b,v}^3 / \sum d_{b,s}^2 \quad (2.10)$$

It is important to note that the mean of the bubble Sauter diameters calculated using Eq. (2.9) is different from the Sauter mean of bubble diameters calculated using Eq. (2.10) presents a comparison between the different definitions of bubble diameters given here for the case of 300 rpm and 0.470 vvm from a sample of 151 measured bubble diameters. The brackets denote sample means. The case reported in Table 2.1 has a mean ellipticity of 0.660 and minimum and maximum ellipticities of 0.035 and 0.964, respectively. These same values correspond to a mean of 1.47, minimum of 1.00 and a maximum of 3.75 for the bubble aspect ratio, which is simply the ratio of the major diameter over minor diameter ( $l/m$ ).

Table 2.1 Comparison of mean bubble diameter values using different definitions, 300 rpm - 0.470 vvm.  
All values are in mm.

Definition	Prolate spheroid	Oblate Spheroid	Equation
$\langle d_{b,v} \rangle$	3.27	3.70	2.3,2.4
$\langle d_{b,s} \rangle$	3.32	3.77	2.6,2.7
$\langle d_s \rangle$	3.19	3.57	2.9
$\sigma_{d_s}$	0.94	1.05	2.9
$d_{s,v}$	3.87	4.41	2.5
$d_{32}$	3.76	4.24	2.10

Table 2.1 demonstrates a significant difference in computed diameters depending upon whether bubbles are assumed to be prolate or oblate spheroids. Relatively smaller difference in the Sauter mean between prolate and oblate spheroids occurs using Eq. (2.10) rather than Eq. (2.5). It is worth noting that the mean of the Sauter diameter calculated using Eq. (2.9) is smaller than the Sauter mean diameter calculated using either Eq. (2.5) or Eq. (2.10).

#### 2.4.2 Mass Transfer Coefficient

In order to compute a volumetric mass transfer coefficient based upon a time series of dissolved oxygen concentrations, it is necessary to invoke an approximation concerning the mixing of the liquid phase. Concentration measurements of dissolved oxygen were performed at four different axial positions and the mass transfer coefficient was found to be independent of axial position within the accuracy of the measurement method used in this study and accordingly, the liquid phase was assumed to be well-mixed. Hence, an oxygen mole balance on the liquid phase (assuming that no oxygen is dissolved in the liquid initially) leads to:

$$\ln\left(1 - \frac{C_L}{C^*}\right) = -k_L a t \quad (2.11)$$

where  $C^*$  and  $C_L$  are the oxygen concentrations in the liquid for saturated conditions and at an arbitrary time  $t$ , respectively,  $a$  is the specific gas-liquid interfacial surface area, and  $k_L$  is the liquid volumetric mass transfer coefficient (Garcia-Ochoa and Gomez, 2009). It should be mentioned that although the initial concentration of oxygen is measured for each experiment, assuming a value of zero (instead of the measured initial oxygen concentration) does not change the computed value of  $k_L a$  and therefore Eq. (2.11) may be used without modification. However, this equation does require an accurate value for the saturation concentration  $C^*$ , which depends upon temperature. The temperature dependence of the saturation concentration was determined using the correlation of Battino *et al.* (Battino *et al.*, 1983):

$$C^* = \exp(-52.16764 + 84.59929/\tau + 23.41230 \ln \tau) \quad (2.12)$$

where  $\tau = T/100$  K, the temperature is in Kelvins and  $C^*$  has units of mL<sub>(Gas)</sub>/L<sub>(Liquid)</sub>.

A typical plot of experimental data according to Eq. (2.11) for five different cases is depicted in Figure 2.4. Over a relatively long range of time the plots are linear, suggesting that the well-mixed approximation is justified. Hence, by fitting a line to the linear portion of the curve,  $k_L a$  can be estimated from the slope. In all cases studied in this work the linear fit resulted in a normalized squared residual of 0.995 or greater.

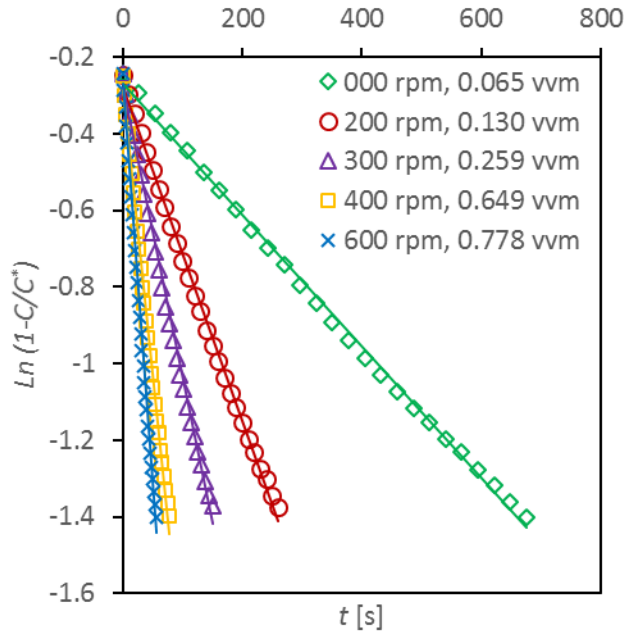


Figure 2.4 Sample linear plot for calculation of  $k_{LA}$  for five of the cases studied in this work.

## 2.5 Results and Discussion

### 2.5.1 Bubble Size

The Sauter mean bubble diameter is reported in Table 2.2 for all cases for which measurements were acquired. The two missing entries in this table are a result of experimental conditions that produce bubble swarms, thereby making it impossible to distinguish individual bubbles.

*Table 2.2 Sauter mean bubble diameters measured for different cases.*

rpm \ vvm	0	100	300	500
0.059	2.12	2.24	3.28	3.82
0.235	2.26	2.69	3.38	4.06
0.470	2.91	3.42	3.76	
0.705	3.11	3.06	4.11	

Individual measured major and minor axis dimensions are plotted in Figure 2.5 for experiments carried out with no inner cylinder rotation. For comparison, the data of Akita and Yoshida (Akita and Yoshida, 1974) obtained using a bubble column are also shown. However, the gas flow rate for which those investigators obtained their data was not reported. With this caveat, it is apparent from Figure 2.5 that the oblate gas bubbles observed in the annular geometry are more ellipsoidal than those found in a cylindrical bubble column. Evidently, wall effects associated with the annular flow result in greater bubble distortion than in the cylindrical bubble column.

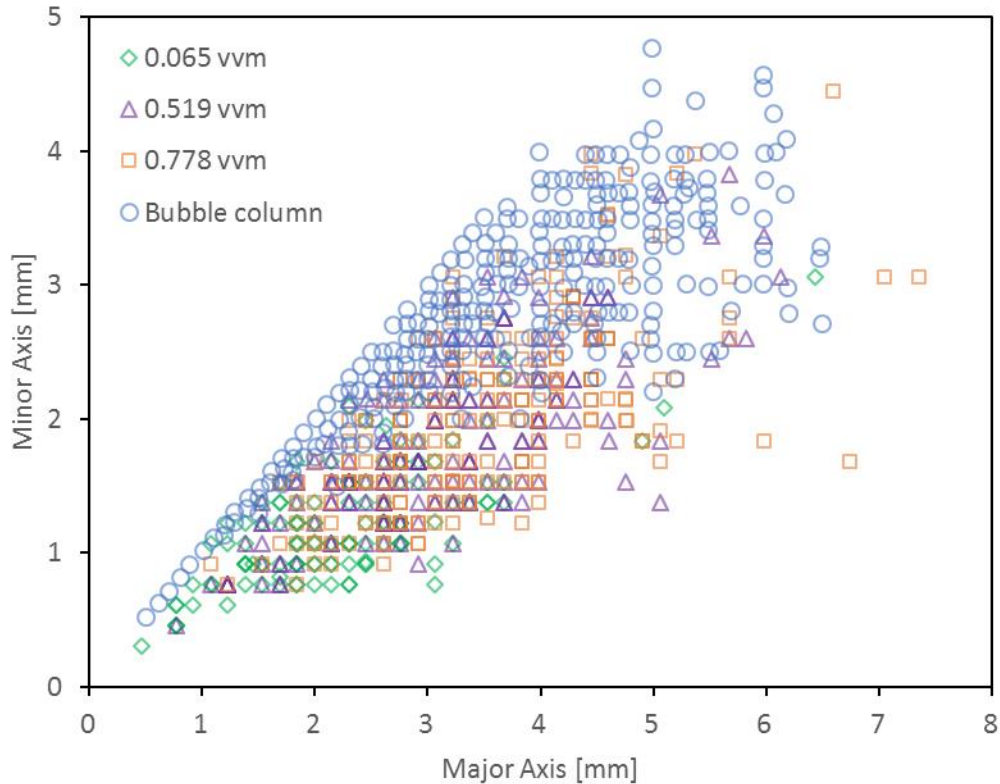


Figure 2.5 Comparison of individual measured bubble dimensions for non-rotating cases against bubble column data (Akita and Yoshida, 1974).

In order to generalize these results, a bubble diameter correlation was developed based upon the two variables considered, namely the cylinder rotation speed and the gas flow rate. The effect of the wall-driven flow can be represented by an azimuthal Reynolds number, defined by Eq. (2.1). Similarly, the strength of the axial gas flow can be quantified by the axial Reynolds number as defined in Eq. (2.2).

Although the bubble diameter should depend upon the superficial gas velocity, it can be expected that other factors, such as the bubble buoyancy and surface tension also play important roles. However, in this study a single pair of fluids was used, and therefore the densities of the fluids and the interfacial surface tension were not varied. Hence, in developing a correlation for the mean bubble diameter, other factors that may be important for a more

general correlation were omitted, such as the Bond number. Nevertheless, since aqueous solutions in contact with low molecular weight gases are common, the correlations developed here may have wide applicability.

Here it is assumed that the Sauter mean diameter can be correlated with the azimuthal and axial Reynolds numbers using a power law relation. The correlation also ensures that the bubble size has a non-zero value at zero azimuthal Reynolds number. The following expression was then obtained using nonlinear least squares regression.

$$\frac{d_{32}}{r_o - r_i} = 1.0 \times 10^{-5} Re_a^{0.11} (Re_\theta + 3.3 \times 10^4)^{0.91} \quad (2.13)$$

A comparison of the dimensionless bubble diameters predicted by this correlation versus experimentally measured values is presented in Figure 2.6, which demonstrates close agreement quantified by a normalized  $R^2$  value of 0.983. For small azimuthal Reynolds numbers, the constant in parenthesis dominates, and the bubble size is relatively independent of the rotational speed of the inner cylinder. For larger azimuthal Reynolds numbers, the monotonic increase in bubble size can be explained as follows. It was observed that as the inner cylinder rotation speed increases, the gas bubbles form bands at boundaries between Taylor vortices, similar to those observed by Hubacz and Wronski (Hubacz and Wroński, 2004). In addition, although gas holdup was not measured, our visual observations are consistent with the hypothesis that gas holdup increases with increasing rotational speed. As a result of these two factors (increased bubble proximity and gas holdup), it can be expected that bubble size will increase due to bubble coalescence as the azimuthal Reynolds number increases.

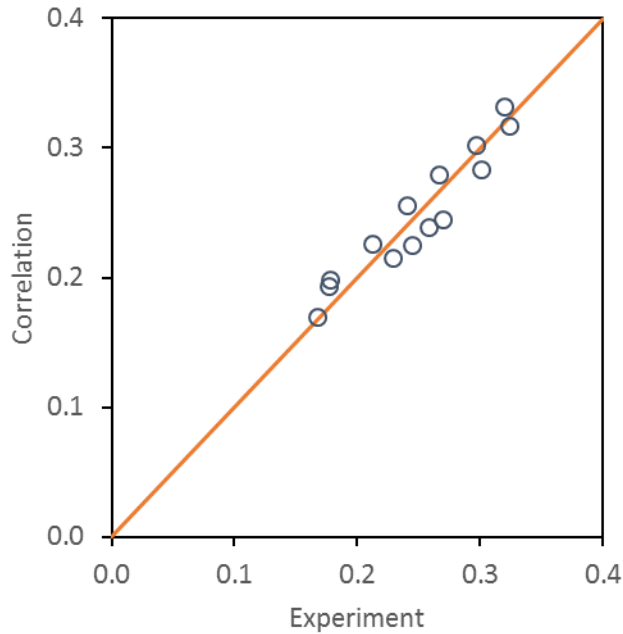


Figure 2.6 Normalized bubble size ( $d_{32}/(r_o-r_i)$ ) calculated using the correlation of Eq. (2.13) versus the measured values using Eq. (2.10).

Detailed simulations of bubbly flow in a Taylor-Couette reactor may require a distribution of bubble sizes rather than simply the Sauter mean diameter. The distributions of bubble sizes calculated using Eq. (2.9) for five experimental cases are shown in Figure 2.7, and each distribution is fit to a log-normal probability density function having identical values of the mean and standard deviation as the corresponding experimental distribution. In all cases, the experimentally determined bubble size distributions are well represented by log-normal functions.

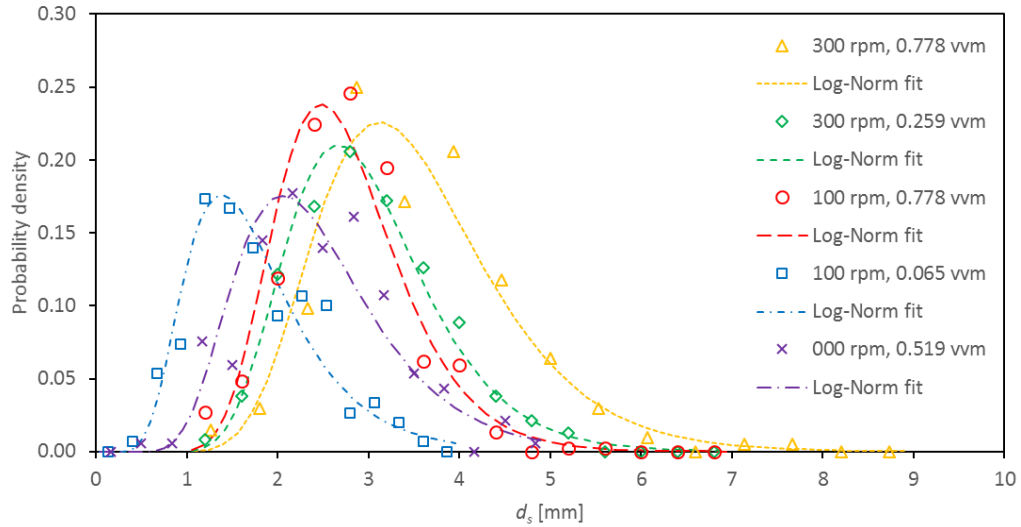


Figure 2.7 Probability density function of the Sauter diameter of bubbles ( $d_s$ ) using Eq. (2.9) and comparison against log-normal distribution.

Following the same approach as for the Sauter mean diameter, a correlation was developed for calculating the mean value of the log-normal bubble size distribution, resulting in the following equation:

$$\mu_{d_s} = 3.6 \times 10^{-6} Re_a^{0.15} (Re_\theta + 2.7 \times 10^4)^{0.89} \quad (2.14)$$

which results in a normalized  $R^2$  value of 0.963.

The standard deviation of the size distributions was approximately  $\sigma_{d_s} = 0.31 \pm 0.08$  for all cases considered, and did not appear to obey any trend with respect to the independent parameters. In addition, the average ellipticity of the bubbles was  $\langle E \rangle = 0.72 \pm 0.12$ .

### 2.5.2 Mass Transfer Coefficient

Values of  $k_{LA}$  were obtained from dissolved oxygen measurements described in section 2.3.3, and these results are reported in Table 2.3 for various cylinder rotation speeds and gas flow rates. In four instances, experiments were repeated two times in order to determine variability of the data. As a result of these replications, the data represented in this study are

estimated to be reproducible within a deviation of  $\pm 6\%$ . Rather than performing experiments for every possible combination of axial and azimuthal Reynolds numbers, approximately 63% of the cases were studied.

*Table 2.3 Measured values of  $k_{La}$  [ $s^{-1}$ ] calculated for different experimental conditions at axial location of 12.7 cm.*

rpm \ vvm	0	100	200	300	400	500	600	700
0.059	0.0021	0.0027	0.0028	0.0032	0.0038	0.0046	0.0063	0.0066
0.117			0.0048	0.0051				
0.235	0.0069		0.0076	0.0081		0.0090		
0.352		0.0104	0.0105		0.0114		0.0155	
0.470	0.0109	0.0126	0.0127	0.0129	0.0142		0.0185	
0.587		0.0153	0.0155	0.0156	0.0160	0.0191	0.0205	
0.705	0.0138	0.0179	0.0179		0.0183		0.0225	

Direct measurement of the gas holdup, and thus the specific interfacial surface area, was not performed due to the complicated motion of the water free surface in the reactor caused by the rotation of the inner cylinder and the escaping gas. In order to cope with this limitation, the following definition of the modified Sherwood number based on the Sauter mean diameter of bubbles was used in this study (Saenton and Illangasekare, 2013; Sujatha et al., 1999).

$$Sh = \frac{k_L a d_{32}^2}{D_L} \quad (2.15)$$

The diffusion coefficient of oxygen in water is  $D_L = 2.1 \times 10^{-9}$  m<sup>2</sup>/s for the average room temperature at which experiments were performed. For cases with a rotating inner cylinder, it

is reasonable to assume that the Sherwood number will depend upon the strength of the wall-driven Taylor vortex flow (characterized by the azimuthal Reynolds number) as well as the strength of the axial gas flow (characterized by the axial Reynolds number). As was discussed previously, a more general correlation accounting for buoyancy and surface tension would also include other factors such as the Bond number, but since these factors were not considered, they are omitted here. It should also be noted that the bubble size correlation of Eq. (2.13) was used to compute the Sherwood number. The mass transfer correlation resulting from nonlinear least squares regression is given by:

$$Sh = 1.45 \times 10^{-7} Re_a^{0.82} (Re_\theta + 1.47 \times 10^4)^{1.61} \quad (2.16)$$

The values of the Sherwood number predicted by this equation are compared to values calculated from experimental measurements in Figure 2.8, and the normalized  $R^2$  is 0.984, thereby demonstrating an excellent fit.

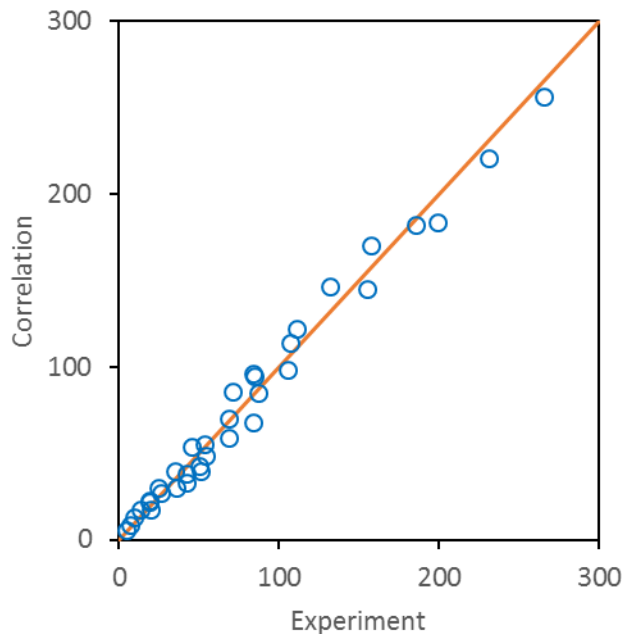


Figure 2.8 Comparison of measured and calculated Sherwood number.

It can be seen from the proposed correlation that at low rotation speeds, the term containing the azimuthal Reynolds number is dominated by the constant in parenthesis, and consequently mass transfer coefficients are predicted to be insensitive to cylinder rotation speed for small azimuthal Reynolds numbers. In contrast, an increase in the value of the axial Reynolds number results in monotonic growth in the value of Sherwood number.

Figure 2.9 shows a comparison of the volumetric mass transfer data of the current study with those published by Dluska *et al.* (Dłuska et al., 2001) for a similar range of axial Reynolds numbers. It is important to note that their experiments were performed using a horizontal Taylor-Couette system with co-flow of liquid and gas phases, using various ratios of the volumetric flow rates of the gas and liquid phases. In contrast, in the present study there is no net axial flow of the liquid phase and buoyancy can be expected to play an important role in driving the axial component of the gas bubble velocity. Here the axial Reynolds numbers are calculated based on the superficial gas velocity according to Eq. (2.2) and the superficial liquid velocity is neglected. Therefore, direct comparison of axial Reynolds numbers used in the two systems is not possible, and it should be observed that the difference between the superficial gas and liquid velocities,  $u_G - u_L$ , in the system with co-flow can be negative, positive or zero whereas it is always positive for the semi-batch system. Nevertheless, Fig. 9 demonstrates that interphase mass transfer is significantly enhanced by rotation of the inner cylinder for a horizontal orientation with co-flow of the two phases, whereas mass transfer is relatively insensitive to cylinder rotation speed for the vertical reactor orientation and semi-batch operation. With no inner cylinder rotation, the mass transfer coefficients in the vertical and horizontal reactors are similar irrespective of the axial flow conditions used.

The difference in the dependence of interphase mass transfer coefficients for the two reactors and flow configurations may be explained as follows. In the horizontal co-flow configuration at sufficiently low cylinder rotation speed, the gas will not be uniformly distributed azimuthally due to the strong relative contribution of buoyancy, and hence gas accumulates at the azimuthal location corresponding to the highest vertical location in the gravity field. Higher cylinder rotation speeds result in greater azimuthal (and radial) dispersion of the gas as well as smaller bubble sizes (Hubacz and Wroński, 2004). As a result of this dispersion and breakup of the gas phase into smaller bubbles, interfacial surface area increases as the azimuthal Reynolds number increases and it can be observed that the increase in the value of  $k_{La}$  is merely due to the increase of the interfacial area (Dłuska et al., 2004). It is shown that the value of the mass transfer coefficient stays relatively constant for the horizontal reactor above a threshold of rotation speed that corresponds to break up of the large gas regions into smaller individual bubbles (Djeridi et al., 2004).

Furthermore, in the horizontal configuration the buoyant force has no axial component and only acts in the radial and azimuthal directions, leading to higher bubble slip velocities where the buoyant force opposes fluid motion. In contrast, as reported in section 4.1, bubble sizes increase with an increase in azimuthal Reynolds number in the vertical configuration. In addition, the bubble dynamics are very different since the buoyant force acts only in the axial direction in the vertical reactor. As was discussed in section 2.5.1, increases in the cylinder rotation speed lead to radial bubble migration towards the inner cylinder and between the Taylor vortices and bubble size increases. Due to this effect, the change in the interfacial area in the vertical reactor as a result of higher rotation speeds is expected to be fairly negligible comparing to the horizontal reactor.

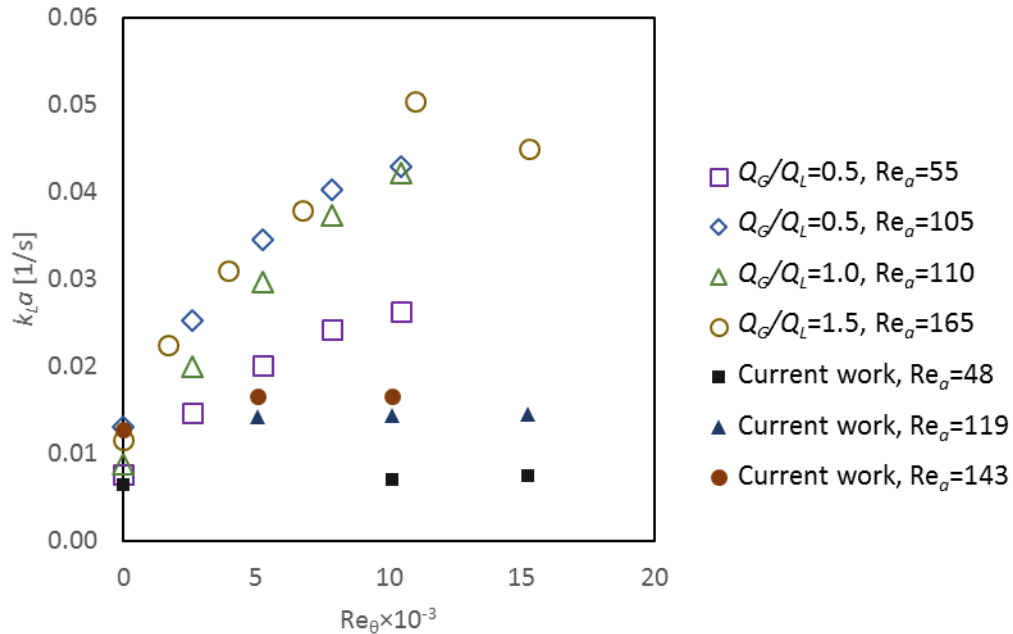


Figure 2.9 Volumetric mass transfer coefficient versus azimuthal Reynolds number at moderate to high axial Reynolds numbers compared with data for a horizontal Taylor-Couette reactor with co-flow of phases (Dluska et al., 2001).

It is also useful to compare interphase mass transfer coefficients in a semi-batch vertical Taylor-Couette vortex reactor with those observed in stirred tanks. For example, the correlation of Kapic and Heindel (Kapic and Heindel, 2006) implies the following relation:

$$k_L a \propto u_G^{0.93} N^{1.342} \quad (2.17)$$

This type of function inherently assumes the mass transfer coefficient to be zero when the impeller is stopped which in the correct case, it needs to converge to the bubble column value. In order to make the comparison possible, using data obtained in the present study excluding the non-rotating cases, an analogous correlation can be developed for the volumetric mass transfer coefficient in terms of parameters corresponding to those in Eq. (2.17) by equating the impeller diameter in a stirred tank with the inner cylinder diameter of a Taylor vortex reactor as follows:

$$k_L a = 0.423 u_G^{0.668} N^{0.178} \quad (2.18)$$

This correlation has a normalized  $R^2$  value of 0.981, which is an excellent fit within the range of the parameters studied. Comparison of exponents in Eqs. (2.17) and (2.18) gives insight into differences between the two types of reactors. Specifically, volumetric mass transfer coefficients in stirred tanks are more sensitive to both superficial gas velocity and impeller speed. In contrast, the generation of fluid shear through the motion of a long smooth wall (as opposed to an impeller) results in formation of Taylor vortices, large scale flow structures that efficiently transport energy and momentum towards the outer wall with relatively small variation in local shear rate, as compared to a stirred tank. This characteristic, namely the relatively uniform shear environment in a Taylor vortex reactor, is highly advantageous for processing material that may be susceptible to shear stress damage, such as microorganisms. However, much greater rotation speeds (as compared to the impeller in a stirred tank) are then required to distribute energy to smaller length scales that are efficacious for increasing interphase mass transport via bubble size reduction and increase of bubble slip velocity.

In the absence of inner cylinder rotation, the Taylor vortex reactor becomes an annular bubble column, and therefore it is useful to consider comparison of the correlations developed here (for  $Re_\theta = 0$ ) with those available for bubble columns. Furthermore, because the rise of the free surface location (with and without gas flow) at the top of the reactor can be easily measured in the absence of inner cylinder rotation, the gas holdup ( $\epsilon_G$ ) could also be determined. The results of these measurements are shown in Figure 2.10, where it can be seen that gas holdup increases linearly as a function of superficial gas velocity with a slope

$u_G/\varepsilon_G=0.23$ , which is essentially the same as the value of 0.24 reported for cylindrical bubble columns (Hills, 1976).

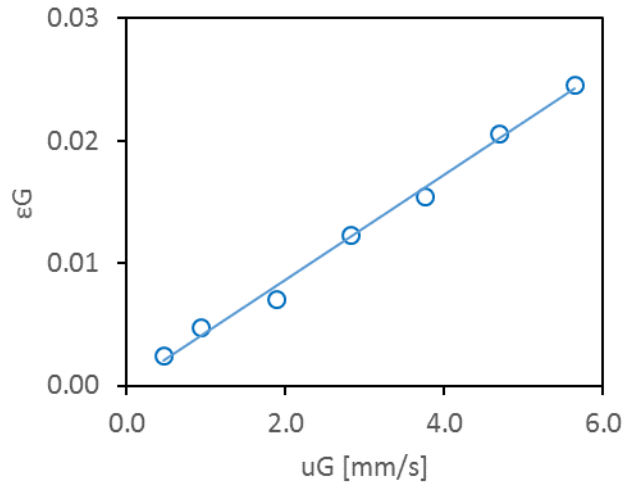


Figure 2.10 Measured gas holdup versus gas flow rate for an annular bubble column (no cylinder rotation).

The value for the interfacial surface area can then be calculated using the following equation (Popovic and Robinson, 1989).

$$a = 6 \varepsilon_G / d_{32} \quad (2.19)$$

and the usual definition of the Sherwood number can be used (Akita and Yoshida, 1973; Popovic and Robinson, 1989):

$$Sh = \frac{k_L d_{32}}{D_L} \quad (2.20)$$

Sherwood number computed using Eq. (2.20) are presented in Figure 2.11 and are compared with those obtained in cylindrical bubble column experiments of Akita & Yoshida (Akita and Yoshida, 1973). Here the Galilei number is defined as:

$$Ga = \frac{g d_{32}^3}{\nu_L^2} \quad (2.21)$$

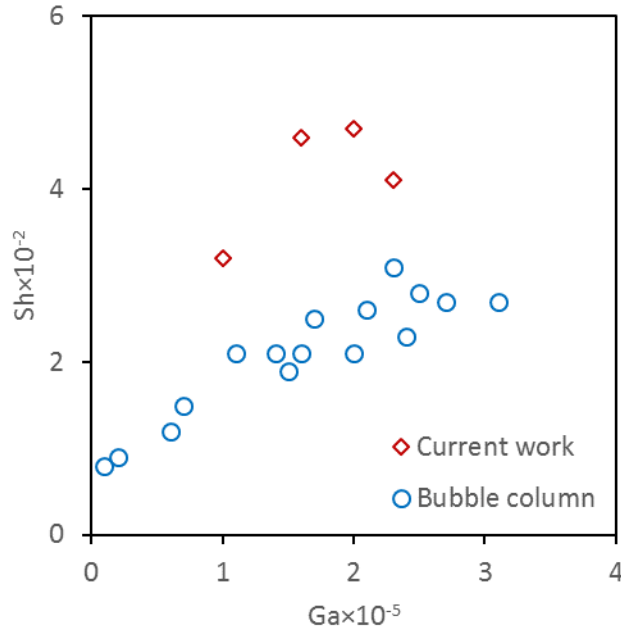


Figure 2.11 Comparison of Sherwood vs Galilei numbers for annular and cylindrical bubble columns (Akita and Yoshida, 1974).

Figure 2.11 shows that the Sherwood numbers for the annular bubble column are larger than those reported for cylindrical bubble columns. Figure 5 may provide insight into the cause of this difference. Specifically, most bubbles in a cylindrical bubble column have low aspect ratio and are essentially spherical. The annular geometry produces many more bubbles with high aspect ratio (greater ellipticity) and consequently greater specific interfacial area. Evidently, the greater specific wall area and narrow confinement in the annular geometry results in increased bubble deformation due to high shear stress near solid surfaces.

## 2.6 Conclusion

Experimental measurements were performed to obtain bubble size and shape distributions and liquid phase volumetric mass transfer coefficients in a vertically oriented semi-batch Taylor-Couette reactor for several combinations of axial and azimuthal Reynolds

numbers. Bubble size distributions were found to be log-normally distributed, and the Sauter mean diameter was shown to monotonically increase with increasing inner cylinder rotation speed and gas flow rate according to a power law relation.

Similarly, a correlation was developed to describe the dependence of the liquid side volumetric gas-liquid mass transfer coefficient on azimuthal and axial Reynolds numbers. Although the mass transfer coefficient increases with both axial and azimuthal Reynolds numbers, the dependence upon azimuthal Reynolds number is relatively weak when compared to data obtained in horizontal Taylor vortex reactors with co-flow of gas and liquid. The observed differences can be explained by considering the contribution of the buoyant force to bubble size and spatial distribution. Specifically, in horizontal reactors the buoyant force can be resolved into radial and azimuthal components and does not contribute to axial motion. As a result, increase in the inner cylinder rotation speed (azimuthal Reynolds number) leads to increased azimuthal and radial dispersion and smaller bubble size. In contrast, for vertical Taylor vortex reactors, the buoyant force acts only in the axial direction, and increases in cylinder rotation speed concentrates bubbles near the inner cylinder wall and between the Taylor vortices, producing larger bubbles.

For the instance of no inner cylinder rotation, the Taylor vortex reactor reduces to an annular bubble column and mass transfer coefficients can be compared with those for traditional cylindrical bubble columns. Bubble size and shape measurements demonstrate that bubbles have higher aspect ratio in annular columns compared to those observed in cylindrical columns, leading to slightly greater values of the volumetric mass transfer coefficient in the annular system.

Although volumetric mass transfer coefficients in vertically oriented gas-liquid Taylor vortex reactors do not increase as rapidly with increasing azimuthal Reynolds number as in horizontally oriented reactors, typical values for the turbulent flow conditions studied here ranged between  $k_{LA} = 0.01-0.02 \text{ s}^{-1}$ . When compared with characteristic time scales for slow reaction processes, such as those that occur in photosynthetic microorganisms to produce bio-oil, these values suggest that vertical gas-liquid Taylor vortex reactors are not mass transfer limited for these applications.

## 2.7 Acknowledgements

The authors acknowledge the efforts of undergraduate lab assistants, Ekoue Kangni and Eric Hessing in designing and performing the experiments. We also gratefully acknowledge financial support for this work from the National Science Foundation (CBET-1236676).

## CHAPTER 3

EXPERIMENTAL INVESTIGATION OF THE EFFECT OF ETHYL ALCOHOL  
SURFACTANT ON OXYGEN MASS TRANSFER AND BUBBLE SIZE DISTRIBUTION  
IN AN AIR-WATER MULTIPHASE TAYLOR-COUPETTE VORTEX BIOREACTOR

This chapter is a manuscript under preparation for submission to Chemical Engineering Journal. I am the main contributor to this work.

## 3.1 Abstract

Volumetric liquid mass transfer, bubble size distribution, and bubble shape were measured in a vertically oriented semi-batch gas-liquid Taylor-Couette vortex reactor with an aspect ratio of  $\Gamma=h/(r_o-r_i)=40$  and radius ratio of  $\eta=r_i/r_o=0.75$ . Azimuthal Reynolds number, Axial Reynolds number and Capillary number were varied between 0 to  $5.1\times 10^4$ , 7 to 99, and  $6.1\times 10^{-6}$  to  $76.0\times 10^{-6}$ , respectively. Power-law correlations based on these data are presented for dimensionless Sauter mean diameter and Sherwood number in terms of the dimensionless parameters. Presence of ethanol as surfactant in the liquid was shown to inhibit bubble coalescence, which in addition to a lower interfacial surface tension causes a generally lower bubble size at higher concentrations of surfactant. It was also shown that the mass transfer coefficient generally increases with higher concentrations of surfactant. Both the bubble diameter and mass transfer are influenced more at lower concentrations of surfactant and introduction of higher amount of ethanol causes a lower change in both parameters.

### 3.2 Introduction

Gas-liquid mass transfer in agitated vessels is a problem with important industrial applications and it has been studied extensively, including the development of correlations for volumetric mass transfer coefficients. Reactors typically used for these applications include bubble columns (Behkish et al., 2007; Calderbank and Lochiel, 1964; Heijnen et al., 1984; Linek et al., 2005b; Dale D McClure et al., 2015; Pittoors et al., 2014; Vasconcelos et al., 2003), stirred tanks (Bouaifi et al., 2001; Hassan et al., 2012; Kapic and Heindel, 2006; Labík et al., 2014; Schlüter and Deckwer, 1992; Ungerman and Heindel, 2007), and various wall-driven gas-liquid reactors (Baier et al., 2000; Gao et al., 2015a; Haut et al., 2003; Hubacz and Wroński, 2004; Nemri et al., 2014; Ramezani et al., 2015). Mass transfer in these systems can be affected by several factors including the presence of impurities, additives, or surfactants, the latter of which has been subject to extensive research (D. Gomez-Diaz et al., 2009; Diego Gomez-Diaz et al., 2009; Hebrard et al., 2009; Jamnongwong et al., 2010; Özbek and Gayik, 2001b; Sardeing et al., 2006). Most studies have focused on bubble columns (Asgharpour et al., 2010; Chen et al., 2013; Garcia-Abuin et al., 2013; Jia et al., 2015; Koide et al., 1985; Vázquez et al., 2000), although various other reactors have also been considered (Benedek and Heideger, 1971; Moraveji et al., 2012; van der Meer et al., 1992; Zhang et al., 2013). To the best of our knowledge, there has been no study reported using a Taylor-Couette vortex reactor.

Taylor vortex flow occurs in the annular space between two concentric cylinders, with a rotating inner cylinder and a fixed outer cylinder, as shown in Figure 3.1. The flow patterns and instabilities produced have been extensively studied (Andereck et al., 1986; Bilson and Bremhorst, 2007; Dong, 2007; Donnelly, 1991; Fenstermacher et al., 1979; Lathrop et al., 1992; Pirrò and Quadrio, 2008; Pudjiono et al., 1992; Taylor, 1923; Wang et al., 2005a;

Wereley and Lueptow, 1999, 1998). Taylor vortices have been used in several varied applications such as water purification (Dutta and Ray, 2004), emulsion polymerization (Imamura et al., 1993; Kataoka et al., 1995), liquid-liquid extraction (Baier et al., 2000; Davis and Weber, 1960), pigment preparation (Kim et al., 2014), photocatalysis (Sczechowski et al., 1995), culture of animal cells (Haut et al., 2003), and cultivation of microalgae (Brown et al., 1964; Kong and Vigil, 2014; Kong et al., 2013; Oasmaa et al., 2009). Two phase Taylor-Couette flow is very different from single phase and several interesting phenomena occur with the addition of the second phase. A variety of temporal and spatial hydrodynamic structures are observed with feeding two immiscible liquids into a horizontal Taylor vortex flow cell (Baier and Graham, 2000; Campero and Vigil, 1999, 1997; Zhu and Vigil, 2001b). Introduction of a gas phase into a vertical liquid Taylor vortex flow cell dramatically decreases the drag on the rotation inner cylinder and causes nontrivial spatial distribution of gas bubbles (Chouippe et al., 2014; Disting and Balabani, 2009; Maryami et al., 2014; van Gils et al., 2013; Van Gils et al., 2011; Wongsuchoto et al., 2003b). Some recent studies have been performed in order to characterize these gas-liquid interactions in Taylor-Couette flows (Dłuska et al., 2001; Gao et al., 2015b; Hubacz and Wroński, 2004; Ramezani et al., 2015).

Interfacial surface tension between gas bubbles and the continuous liquid phase affects mass transfer, bubble size (Alves et al., 2002; Dumont et al., 2006; Gomez-Diaz et al., 2008; Jordan and Schumpe, 2001; Painmanakul et al., 2005) and coalescence and breakup of bubbles (Anastasiou et al., 2010; Chern et al., 2001; Sch et al., 2002; Walter and Blanch, 1986). Generally, the addition of surfactant reduces the size of bubbles, resulting in increased specific interfacial surface area,  $a$  (Chaumat et al., 2007; Garcia-Abuin et al., 2012, 2010; D. Gomez-Diaz et al., 2009; Hebrard et al., 2009; Özbek and Gayik, 2001b) and gas holdup (Hur et al.,

2014) while simultaneously decreasing the liquid side mass transfer coefficient,  $k_L$  (Belo et al., 2011; McClure et al., 2014). Hence, the overall effect of addition of surfactants on the gas-liquid mass transfer rate depends upon whether  $k_L$  or  $a$  is more sensitive to these additives. In general, surfactants have a much larger impact on interfacial surface area, and therefore the value of  $k_{La}$  increases with introduction of additives (Asgharpour et al., 2010; Benedek and Heideger, 1971). Examples of such surfactants in aqueous systems include alcohol (Anastasiou et al., 2010; Dumont et al., 2006; Garcia-Abuin et al., 2010; Hur et al., 2014; Jordan and Schumpe, 2001; McClure et al., 2015), glycerol (Özbek and Gayik, 2001b), the Tween family (Belo et al., 2011; Diego Gomez-Diaz et al., 2009), sodium sulphite solution (Linek et al., 2005a, 2004), ionic surfactants (Moraveji et al., 2012), and various sugars (Chern et al., 2001; Dale D. McClure et al., 2015).

Following our previous work showing the development of empirical correlations for bubble size and volumetric interphase mass transfer coefficients (Ramezani et al., 2015), this paper extends the analysis to include the effect of interfacial surface tension on the volumetric liquid side mass transfer coefficient as well as the size distribution and shapes of bubbles in a vertically oriented semi-batch gas-liquid Taylor vortex reactor. It is shown that for fixed reactor geometry (cylinder radii and length), the volumetric mass transfer coefficient and droplet diameter depend not only on the axial and azimuthal Reynolds numbers, but also on the Capillary number. These results are then compared with our previous work and conclusion are drawn.

### 3.3 Experimental Methods

#### 3.3.1 Apparatus and Operating Conditions

The apparatus used in this study is identical to the one previously used in experimental and numerical studies of the oxygen mass transfer in a range of operating conditions in a Taylor-Couette bioreactor (Ramezani et al., 2015). A drawing of the apparatus is shown in Figure 3.1, and the main features of the device include radius ratio and aspect ratio of  $\eta=r_i/r_o=0.75$  and  $\Gamma=h/(r_o-r_i)=40$  respectively. The procedure for measuring the liquid side mass transfer coefficient and bubble size and analyzing the collected data was the same as that used by Ramezani et al. (Ramezani et al., 2015), with the exception of a few modifications and improvements described below.

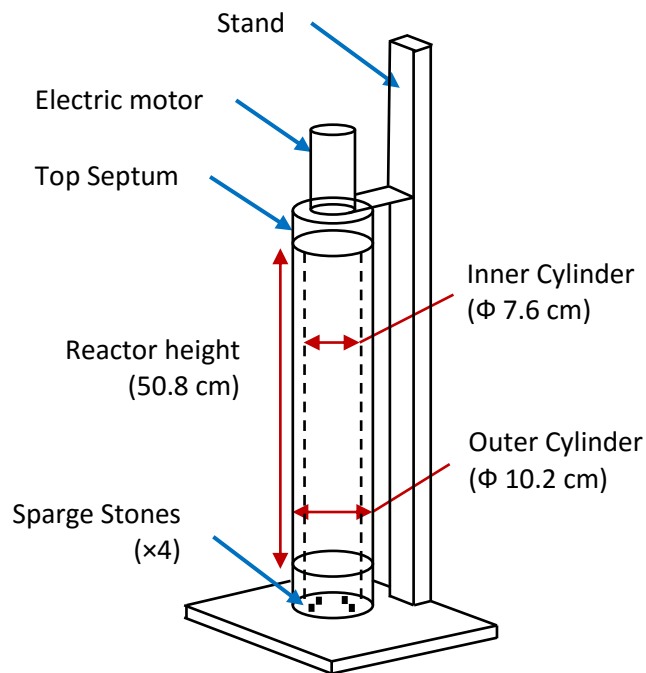


Figure 3.1 Taylor-Couette vortex reactor (Ramezani et al., 2015).

In the current study, inner cylinder rotation rates of 0 to 700 rpm were studied producing azimuthal Reynolds numbers, defined as:

$$Re_{\theta} = \frac{r_i \omega_i (r_o - r_i)}{\nu_L} \quad (3.1)$$

up to  $5.1 \times 10^4$ . For single phase flow, this range is well within the turbulent Taylor vortex flow regime (Andereck et al., 1986). The molar composition of the gas fed to the reactor was chosen to simulate air (79% nitrogen, 21% oxygen), and the total volumetric gas flow rate was varied between 100 sccm and 800 sccm. These feed rates translate to a range of 0.059-0.471 vvm (vessel volumes per minute). The axial gas Reynolds number is defined as:

$$Re_a = \frac{2u_G(r_o - r_i)}{\nu_L} \quad (3.2)$$

using the superficial gas velocity and the hydraulic diameter of the annulus. Axial Reynolds numbers ranged from 7 to 99, corresponding to superficial gas velocities of 0.46 mm/s to 3.67 mm/s. In the absence of cylinder rotation, these gas velocities correspond to the bubbly flow regime when compared to a bubble column with the same hydraulic diameter (Shah et al., 1982). A similar assumption leads to predicted gas holdups of approximately  $\varepsilon_G = 0.03-0.04$  for the highest gas flow rate studied (Campero and Vigil, 1999).

### 3.3.2 Modulation of Interfacial Surface Tension

A wide range of surfactants, including variations of Tween 80 and 60, isopropanol, and ethanol, were considered as a means for varying the gas-liquid interfacial surface tension. Preliminary tests demonstrated that powerful surfactants such as the Tween family lead to problems that make it difficult to carry out the experiments. First, foaming of such surfactants at the liquid free surface at the top of the reactor causes the concentration of the surfactant to decrease over time, particularly in the lower range of concentrations considered. Second, such surfactants require a dynamic method for measuring the effective surface tension, which in turn depends on the renewal rate of the interface (Rosso et al., 2006). Third, the hydrophobicity of these molecules causes them to migrate to the regions with an interface with air, which

results in a gradient of surfactant concentration in the reactor with higher concentration at the liquid free surface at the top. Even though the rotation of the inner cylinder and the resulting mixing inside the reactor causes slight adjustment of this effect, the uniformity of surfactant concentration throughout the reactor cannot be determined for certain. For the purpose of the current study, homogeneity of the properties of working fluids is assumed and it is important to be maintained for a proper measurement of mass transfer. Fourth, these surfactants take some time to form micelles and to attach themselves to air bubbles (Ferri and Stebe, 2000). Our preliminary experiments demonstrated that Tween does not affect bubble formation and interaction in the areas near the sparge stones. Most bubble coalescence occurs in the immediate vicinity of the sparge stones due to gas holdup in this region and because entering bubbles have a very small size. Hence, if the characteristic time scale for the surfactant to act on the bubble-liquid interface is too long, then the effect of interfacial surface tension on the mass transfer and bubble size distribution will be masked. The time scale for most surfactants to modulate the surface tension of an entering bubble is on the order of a few seconds (Ferri and Stebe, 2000). By comparison, the typical formation time of bubbles in the reactor (depending upon cylinder rotation speed and gas flow rate) is approximately a millisecond. Therefore, we conclude that using surfactants such as Tween causes formation of bubbles with practically no influence from the surfactant.

In contrast to surfactants such as Tween, mixture of alcohol in water has several advantages. The high solubility of alcohol allows for a wide range of surface tensions to be achieved, in contrast to amphiphilic surfactants. The change in surface tension is not caused by formation of micelles, and hence no dynamic behavior need be considered. Furthermore, the surface tension is spatially homogeneous. However, the relatively large mole fractions of

alcohol needed to modulate surface tension leads to changes in the liquid mixture properties. Nevertheless, since the aim is to develop empirical correlations for bubble size and interphase mass transfer coefficients, these changes in fluid properties can be accounted for by making use of dimensionless parameters. A concern arising from preliminary experiments using different alcohols was an observation of apparent inhibition of bubble coalescence - a phenomenon that has been previously reported (Hur et al., 2014; Krishna et al., 2000). For example, the presence of relatively small amounts of ethyl alcohol, even below 0.5 mass percent, in the working liquid practically prevents coalescence of gas bubbles from the moment of their introduction into the liquid through sparge stones. For example, the image on the right side of Figure 3.2 shows such bubbles for the lowest alcohol concentration studied here, and the image on the left shows the bubble in the same experimental condition using only water. The bubble sizes are clearly different in the two images, in spite of a very small change in surface tension (~1.5%). Hence, by using sparge stones to break up the entering gas into tiny bubbles, these tiny bubbles coalesce quickly and form larger bubbles, similar to the size shown in the Left side image of Figure 3.2 The presence of alcohol strongly inhibits coalescence even far downstream from the gas injection point. In order to avoid this problem, large gas bubbles were introduced into the reactor using 23G blunt needles. In this way, coalescence is avoided and bubbles reach a steady-state size via breakage mechanisms which in turn depend upon reactor operating conditions that determine the hydrodynamics. Four needles located evenly around the perimeter of the gap area between the inner and outer cylinders were installed and the inlet tubings were carefully examined and adjusted for making a uniform inlet gas flow from all the needles.



*Figure 3.2 Sample bubble images in reactor. Left: Using sparger stone in absence of alcohol / Right: Using sparger stone in presence of alcohol.*

Hence, in order to vary the gas-liquid interfacial surface tension, various mixtures of ethanol and water were used for the continuous liquid phase. Ethanol concentrations up to a mass fraction of 0.20 were employed, yielding gas-liquid interfacial surface tensions ranging between 40.6 to 72.5 mPa.s, The corresponding range of the capillary number, defined as:

$$Ca = \frac{\mu_L u_G}{\sigma} \quad (3.3)$$

is  $6.1 \times 10^{-6}$  to  $76.0 \times 10^{-6}$ . A lowest ethanol concentration of 0.46% is required for having a marked influence on the hydrodynamics (Sijacki et al., 2013). Because in some cases large mass fractions of ethanol were employed, fluid mixture properties were also affected as shown in Table 1. Properties of the water-ethanol mixture including density, viscosity, and interfacial surface tension were acquired from Khattab et. al. (Khattab et al., 2012) and the saturation concentration of air in water is calculated using the correlation of Battino et. al. (Battino et al., 1983). The diffusion coefficient of air in pure water and in pure ethanol was taken from Singh

and Prasad (Singh and Prasad, 2011), and mixture values were assumed to depend linearly on mole fraction (Wong and Himmelblau, 1964).

*Table 3.1 Properties of Ethanol-Water mixture.*

Mass fraction [%]	Mole fraction [%]	$\rho_L$ [kg/m <sup>3</sup> ]	$\mu_L$ [mPa.s]	$\sigma$ [10 <sup>-3</sup> N/m]	$D_L$ [10 <sup>-9</sup> m <sup>2</sup> /s]
0	0.0	997.7	0.96	72.5	2.01
0.46	0.18	997.3	0.97	71.5	2.01
5	2.06	993.0	1.12	61.6	1.99
20	9.78	977.1	1.68	40.6	1.92

### 3.3.3 Photographic Methods for Bubble Size Determination

A Canon DSLR camera (EOS Rebel T3i) equipped with a zoom lens (EF-S 18-55 mm) adjusted to a focal length of 31 mm was used to record images of the flow test section using a shutter speed of 1/200 s and an aperture of f/14. In order to improve the clarity of the bubble edges in the images, an indirect lighting system with multiple external flashes and reflective umbrellas was used to decrease reflections from the inner cylinder. The sharpness of the images allows for a more accurate determination of the major and minor axes of bubbles, as shown in Figure 3.3.

The detailed procedure for measuring bubbles and equations used in calculation of the bubble Sauter diameter are explained in length by Ramezani et al. (Ramezani et al., 2015) and similarly, the bubbles are assumed to take on a prolate shape for all cases with a rotating inner cylinder and an oblate shape for cases without rotation of the inner cylinder (annular bubble column). The Sauter diameter of an individual bubble is an equivalent spherical diameter that is calculated based on a volume equivalent diameter and a surface equivalent diameter

(Muroyama et al., 2012). This individual Sauter diameter is used for histogram plots and measuring the size distribution of bubbles. However, in calculations of the mass transfer, the Sauter mean diameter of all the bubbles is used.



*Figure 3.3 Sample bubble image showing major and minor axis measurements.*

### 3.3.4 Determination of Mass Transfer Coefficient

In contrast to our previous report, which used only de-ionized water for the liquid medium, several mixtures of ethanol and de-ionized water were used for this study. In order to maintain consistency of fluid properties, for a given fluid composition, the same liquid was used to perform experiments for all rotation speeds and gas flow rates considered, in contrast to preparing a new batch of working fluid for each measurement.

In addition, the experiment was run in multiple successive cycles of purging and introducing air to acquire an average for the mass transfer coefficient based on 3 successive measurements in contrast to a single measurement in the previous study. A typical plot of the dissolved oxygen concentration versus time for successive cycles is shown in Figure 3.4 Also

indicated is the portion of the data that was used for mass transfer calculations. All the measurements reported here show an  $R^2$  value of over 0.95 with most cases being above 0.99 showing a great correlation for calculation of mass transfer.

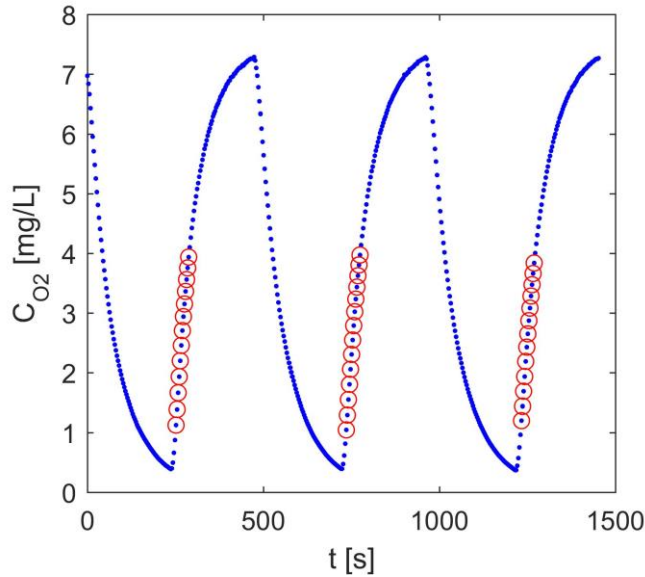


Figure 3.4 A full cycle of oxygen concentration data collection. Circles show the portion used for mass transfer calculations.

The volumetric mass transfer coefficient measurement is performed using a dynamic method based upon a time series of dissolved oxygen concentrations, assuming well-mixed fluids in the reactor. Hence, an oxygen mole balance on the liquid phase (assuming that no oxygen is dissolved in the liquid initially) leads to:

$$\ln\left(1 - \frac{C_L}{C^*}\right) = -k_L a t \quad (3.4)$$

where  $C^*$  and  $C_L$  are the oxygen concentrations in the liquid for saturated conditions and at an arbitrary time  $t$ , respectively,  $a$  is the specific gas-liquid interfacial surface area, and  $k_L$  is the liquid side volumetric mass transfer coefficient (Garcia-Ochoa and Gomez, 2009).

### 3.4 Results and Discussion

A total of 44 experimental trials were carried out, each corresponding to a specific combination of ethanol concentration (mass fractions 0, 0.0046, 0.05, 0.2), gas flow rate (100-800 sccm), and cylinder rotation speed (0-700 rpm). A range of rotational speeds from 0-700 rpm were studied with air flow rates of 100-800 sccm corresponding to 0.06 – 0.47 vvm. The superficial gas velocity varied from 3.7 mm/s.

#### 3.4.1 Bubble size and shape

Representative probability distributions for the bubble Sauter diameter are shown in Figure 3.5 for various reactor operating conditions and fluid compositions. These data are well fit by log-normal distributions, as was reported previously for semi-batch gas-liquid Taylor vortex flow (Ramezani et al., 2015). The mean of the bubble Sauter diameters varies between 2-4.5 mm for most cases with standard deviations of 0.12-1.31 mm.

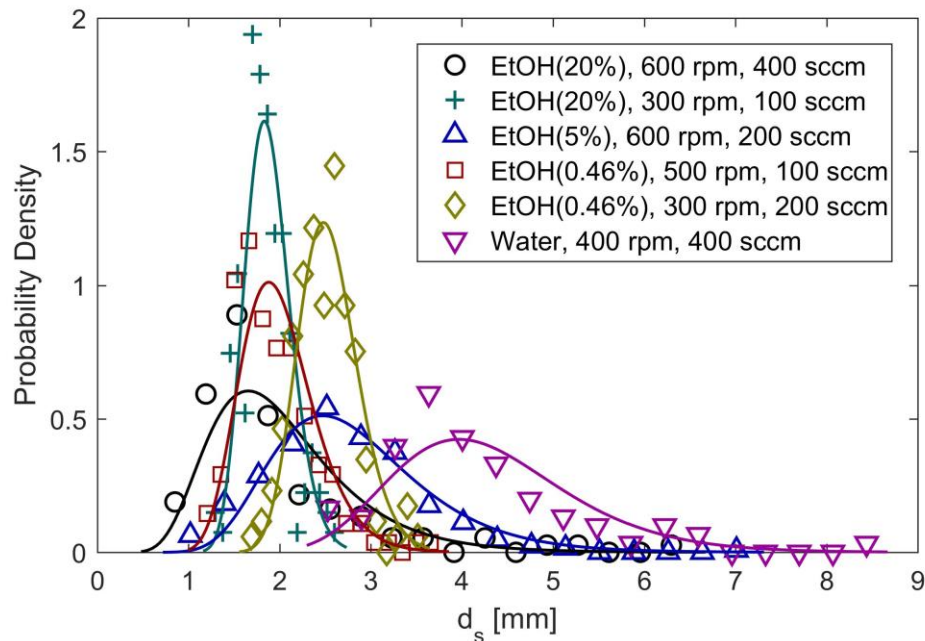


Figure 3.5 Probability density of bubble Sauter diameter for several measured cases.

Figure 3.6 shows the effect of surface tension on Sauter mean diameter for a selection of the studied cases. It is clear from the results that presence of surfactant in general causes smaller bubble sizes. For the lowest surfactant concentration, despite the surface tension being almost similar, bubble diameters are generally 10-25% smaller. This shows that independent of the effect of ethanol on the surface tension, its ability to inhibit bubble coalescence plays a major role in keeping the bubble sizes smaller. It is also evident from this figure that the interfacial surface tension below  $\sim 60$  mN/m have very minimal influence on the Sauter mean bubble diameter. There are a few cases that show slight increase in bubble size with a decrease in surface tension opposite to the general trend of most cases.

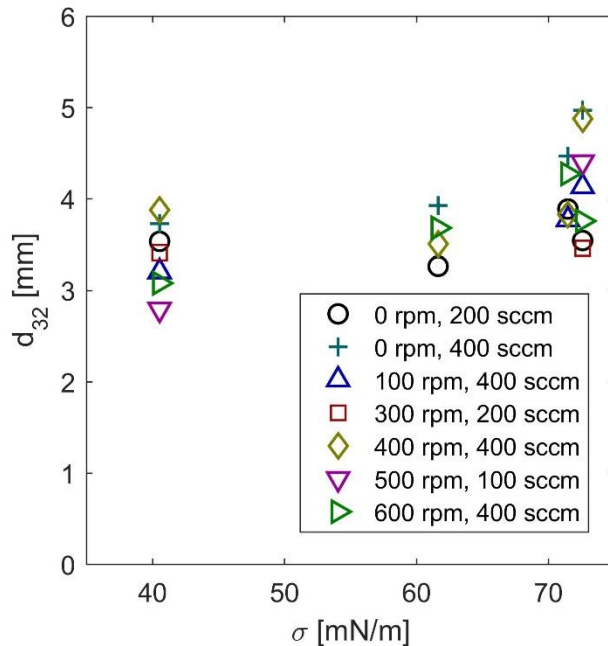


Figure 3.6 Effect of surface tension on Sauter mean bubble diameter.

It was attempted to fit several different types of functions including a power-law correlation to the available bubble size data in terms of the independent non-dimensional parameters with little success. The correlation for the best fit was found as given in Eq. (5).

This correlation has as  $R^2$  value of 0.540 and a mean error of 5.6%.

$$\frac{d_{32}}{r_o - r_i} = 1.59 \times 10^{-3} \text{Re}_a^{0.301} (\text{Re}_\theta + 1.13 \times 10^5)^{0.324} \text{Ca}^{-0.030} \quad (5)$$

A representation of the performance of this correlation is given in Figure 3.7. It can be observed that this correlation can provide a good estimate for the bubble size even though individual correlation terms specially the azimuthal Reynolds number show relatively poor performance. Further study of the details of the bubble behavior in this reactor is undergoing and preliminary results show that the bubble size variation from the bottom to the top of the reactor can be significant in higher rotation speeds. Even though using the Sauter mean diameter for the purpose of mass transfer measurement is accurate enough, this value does not accurately represent the complex evolution of bubble size in this reactor. In order to provide a proper measurement of bubble size in a Taylor-Couette reactor, it is necessary to measure bubble size as a function of the reactor height and make an attempt for providing separate correlations for initial and final bubble size. Such detailed measurement of bubble size is beyond the scope of the current study.

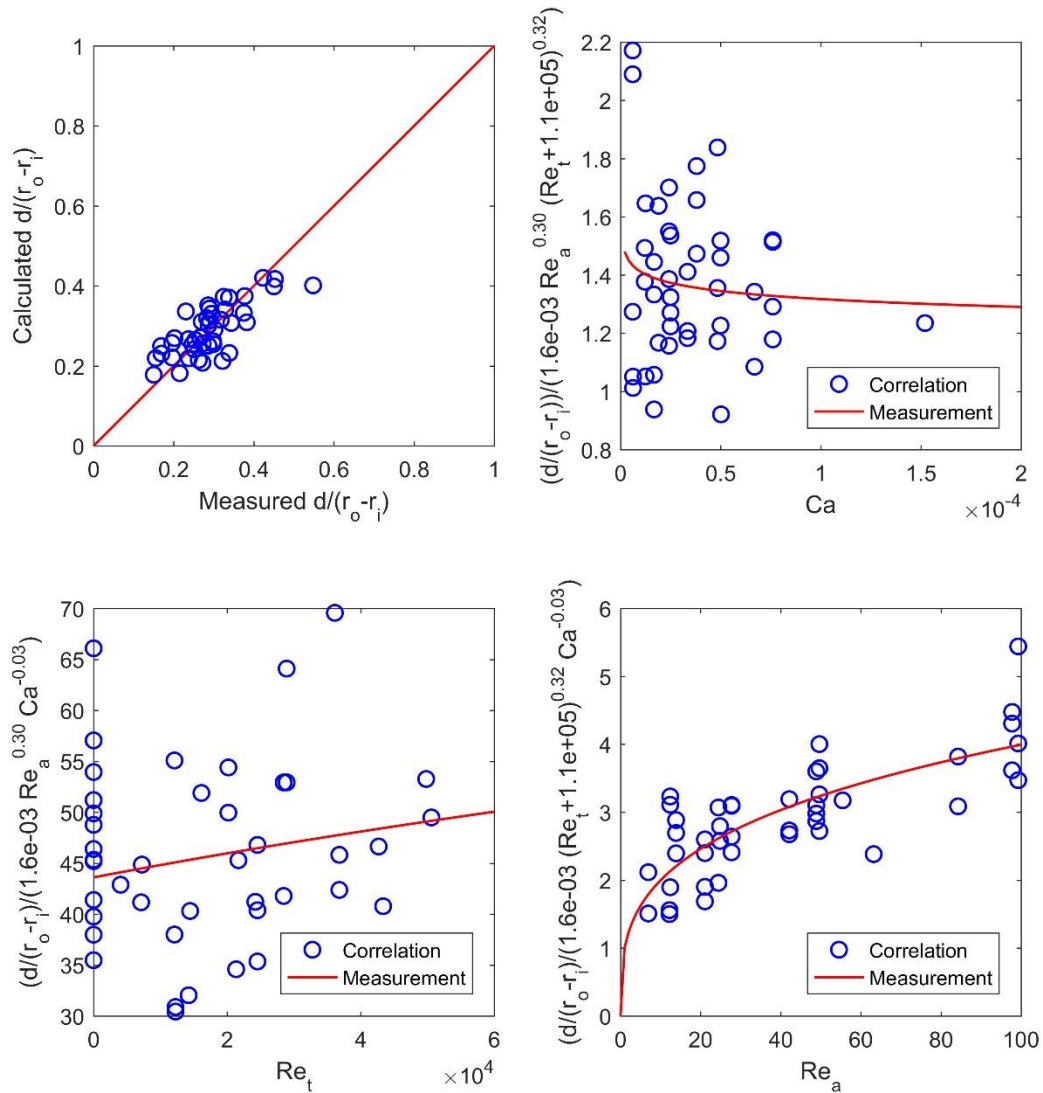


Figure 3.7 Performance of the bubble Sauter diameter correlation.

In addition to the size of the bubbles, it was attempted to characterize their shape assuming them to take on the shape of oblate spheroids for non-rotating cases and prolate spheroids for rotating cases (Ramezani et al., 2015). The average ellipticity of bubbles as a function of the interfacial surface tension is shown in Figure 3.8 for several of the measured cases. It can be seen from this figure that bubbles have on average an ellipticity of 0.5-0.8 that corresponds to an aspect ratio of 1.2-2.0. The lowest studied ethanol concentration generally shows slightly less elliptical bubbles compared to the water only measurements. Even though

there is no clear trend of how average ellipticity is affected by surface tension, it is important to note that all the measured cases show that bubbles on average are far from being spherical.

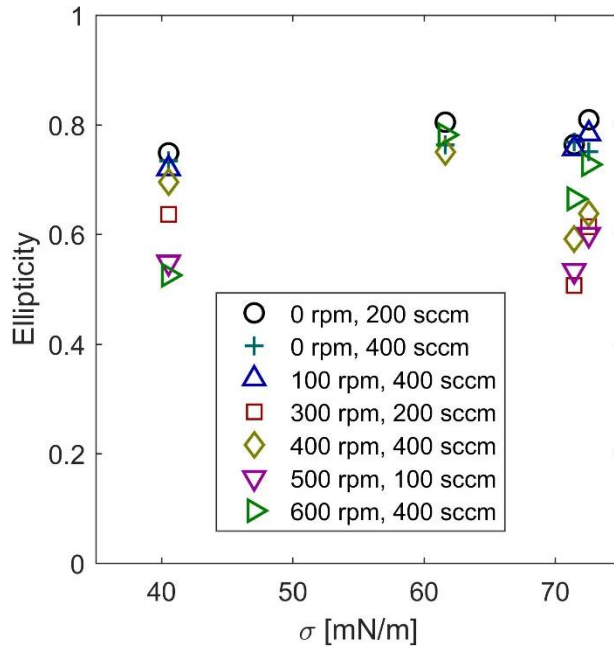


Figure 3.8 Effect of surface tension on average ellipticity.

### 3.4.2 Volumetric Mass Transfer Coefficient

A quick comparison of the  $k_{LA}$  values from current study with that of Ramezani et al (Ramezani et al., 2015) for the water only experiments is shown in Figure 3.9 and Figure 3.10 using plots of the volumetric mass transfer coefficient in terms of the gas flow rate and rotational speed, respectively. Both plots show the current data with the symbols of bigger size using the same shape as the corresponding series.

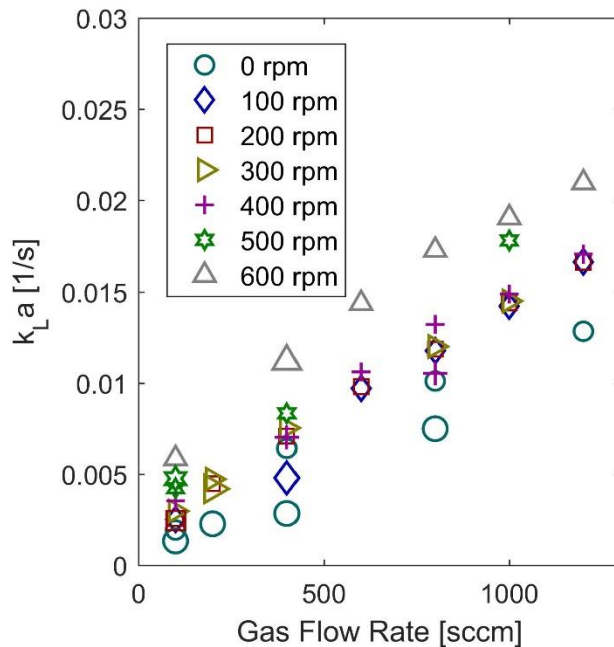


Figure 3.9 Comparison of volumetric mass transfer coefficient in terms of gas flow rate (Ramezani et al., 2015).

Figure 3.9 shows that with similar rotational speeds current data lie within the trend of previously reported experiments except for the no rotation and 100 rpm cases. At higher rotation speeds, the bubble size grows very rapidly right after the injection into the reactor whereas the lower speeds cause a gradual increase in the size of bubbles throughout the reactor. When using needles, the initial bubbles are much larger comparing to the sparger stones even though the average and final bubble size are fairly similar. The rapid growth of the size of bubbles in higher rotational speeds causes the initial transition of bubble size to have negligible effect on the overall mass transfer. However, with lower rotational speeds and gradual growth of the bubbles, using sparger stones causes smaller bubbles to exist in a larger portion of the reactor and causes slightly higher interfacial mass transfer area. Hence the cases with needle show slightly lower mass transfer rate.

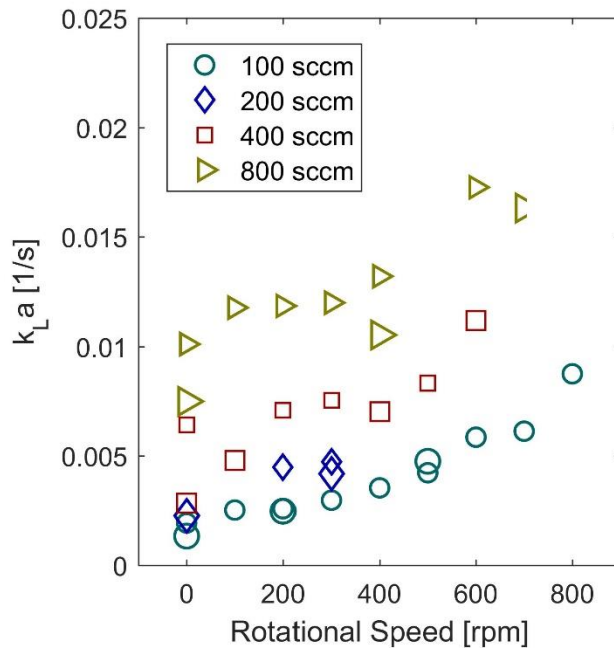


Figure 3.10 Comparison of volumetric mass transfer coefficient in terms of rotational speed (Ramezani et al., 2015).

Figure 3.10 shows at lower gas flow rates the current data lie fairly well within the trend of previously reported data whereas the higher gas flow rates show lower overall mass transfer rate in the current study. The movement of bubbles inside the reactor is highly affected by the azimuthal rotation of the inner cylinder and the Taylor vortices. When using the sparger stones at the inlet, bubbles take place at the sparger surface and are almost stagnant before getting detached due to their size or the shearing flow. When using the needles at lower flow rate, an almost similar behavior in bubble departure from inlet occurs with bubbles getting detached and carried away by the liquid flow. In contrast, at higher gas flow rates using needles, a piercing jet of the gas phase penetrates into the liquid flow that disrupts the flow up to a certain height where it loses its momentum. This initial jet region has the characteristic of highly concentrated gas phase that is less mixed with the liquid that causes a lower mass transfer rate. It is estimated that for the current reactor at highest gas flow rates, a maximum

of a quarter of the reactor length is affected by this jet penetration resulting in the lower mass transfer rates that can be seen in Figure 3.10.

Figure 3.11 shows a plot of mass transfer coefficient versus the interfacial surface tension for several of the measured cases separated by the rotational speed and gas flow rate. It was observed that addition of surfactant generally increases the mass transfer coefficient. Most of the studied cases show a spike in the value of  $k_{La}$  at the lowest ethanol concentration comparing to the water only cases. Further addition of ethanol has a lower effect on the value of mass transfer coefficient with some cases having slightly higher and some having slightly lower  $k_{La}$  values at 5% ethanol concentration comparing to 0.46%. Extending to higher concentrations of ethanol causes even smaller variation of  $k_{La}$ .

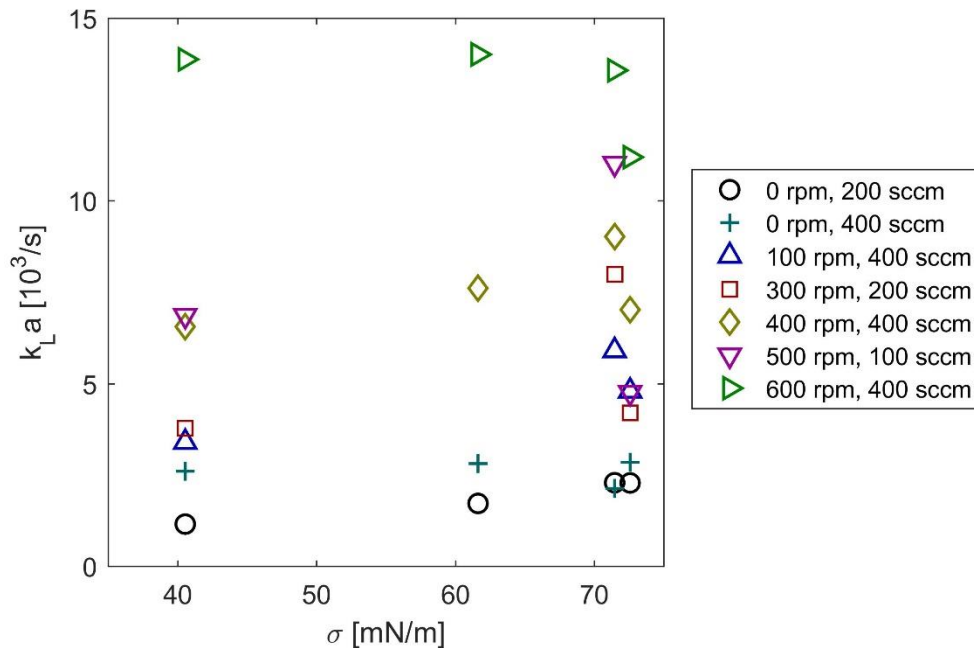


Figure 3.11 Effect of surface tension on mass transfer coefficient.

A power law correlation for the Sherwood number was developed in terms of the azimuthal and axial Reynolds numbers as well as the capillary number. This correlation has an  $R^2$  value of 0.957 and a mean error of 8.5% as is given in Eq. (6).

$$Sh = 4.19 \times 10^{-3} Re_a^{0.805} (Re_t + 1.22 \times 10^4)^{0.941} Ca^{0.312} \quad (3.5)$$

A visualization of the effect of individual terms in this correlation as well as the performance of correlation are given in Figure 3.12. It should be noted that the Sherwood number is a characterization of both mass transfer rate and average bubble size as defined:

$$Sh = \frac{k_L a d_{32}^2}{D_L} \quad (3.6)$$

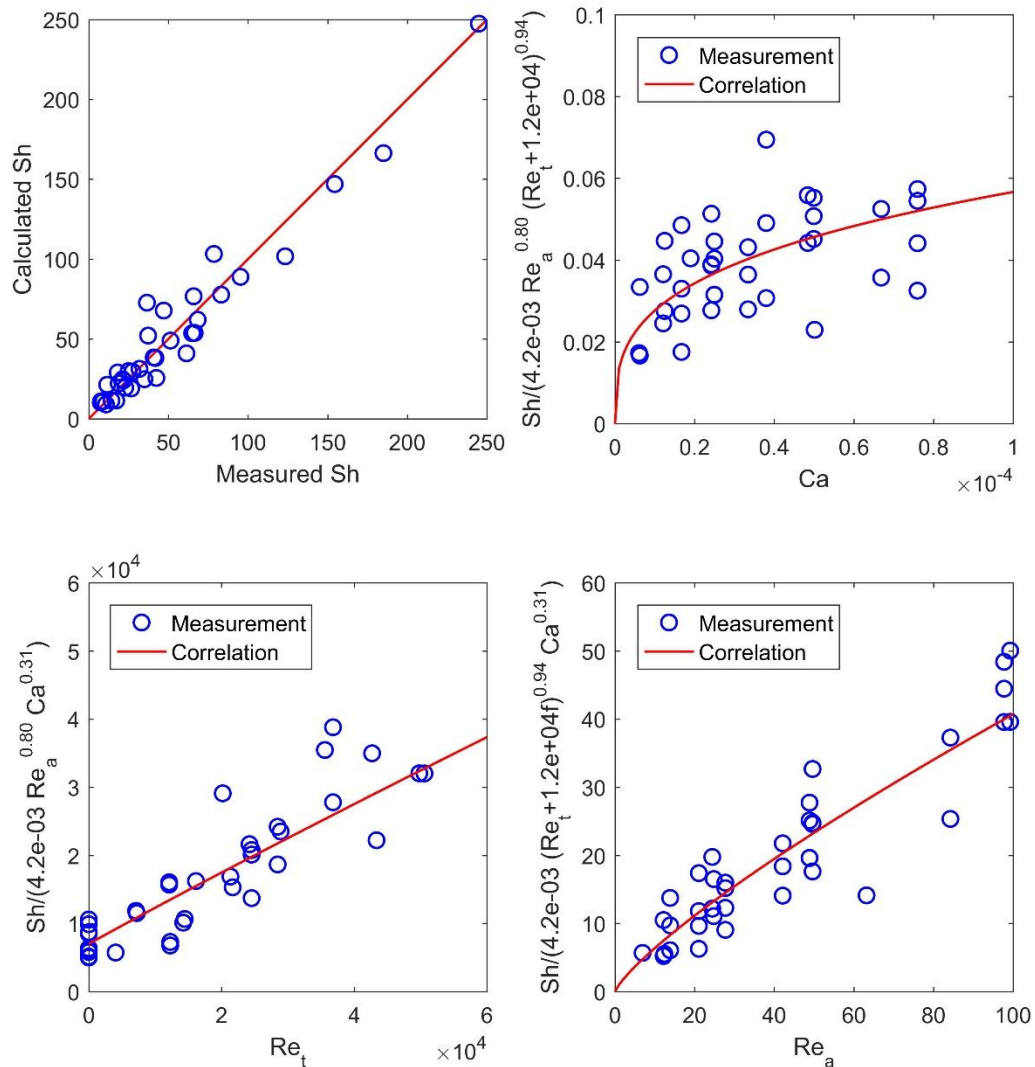


Figure 3.12 Performance of the mass transfer correlation.

### 3.5 Conclusion

Experimental measurements were performed to study the effect of interfacial surface tension on liquid phase volumetric mass transfer coefficient in a vertically oriented semi-batch Taylor-Couette reactor. Bubble size and shape of the secondary gas phase were also measured and the influence of interfacial surface tension was studied. Ethanol was used as the surfactant of choice and experiments were done at several combinations of rotational speed, gas flow rate, and surfactant concentration.

Bubble size distributions were found to show a log-normal distribution and the Sauter mean diameter was shown to generally decrease with higher concentrations of ethanol corresponding to lower interfacial surface tension. This effect is non-linear with higher reduction of the bubble size at lower concentrations of surfactant. An empirical correlation for calculation of the Sauter mean bubble diameter as a function of azimuthal and axial Reynolds numbers and Capillary number. Bubbles were found to have an average ellipticity of 1.2-2.0 even though there seems to be no apparent correlation of ellipticity with the parameters studied here.

Mass transfer coefficients for cases with no surfactant were compared with our previous study and the effect of using needles rather than sparge stones for gas inlet was discussed. It was observed that introduction of the surfactant generally causes an increase in mass transfer coefficient at lower concentrations and higher concentrations of surfactant has little impact on mass transfer. A correlation was proposed for calculation of the Sherwood number in terms of azimuthal and axial Reynolds numbers and Capillary number.

### 3.6 Acknowledgement

We gratefully acknowledge financial support for this work from the National Science Foundation (CBET-1236676). We also appreciate great discussions and helpful insight from our colleagues, Bo Kong and Xi Gao.

## CHAPTER 4

AN ADAPTIVE MODEL FOR GAS–LIQUID MASS TRANSFER IN A TAYLOR  
VORTEX REACTOR

This chapter is an article published in International Journal of Heat and Mass Transfer (Gao et al., 2015a). My contribution is limited to providing the experimental results.

## 4.1 Abstract

Gas–liquid Taylor–Couette flow devices have attracted interest for use as chemical and biological reactors, and consequently the accurate prediction of interphase mass transfer coefficients is crucial for their design and optimization. However, gas–liquid mass transport in these systems depends on many factors such as the local velocity field, turbulent energy dissipation rate, and the spatial distribution and size of bubbles, which in turn have complicated dependencies on process, geometric, and hydrodynamic parameters. Here we overcome these problems by employing a recently developed and validated Eulerian two-phase CFD model to compute local values of the mass transfer coefficient based upon the Higbie theory. This approach requires good estimates for mass transfer exposure times, and these are obtained by using a novel approach that automatically selects the appropriate expression (either the penetration model or eddy cell model) based upon local flow conditions. By comparing the simulation predictions with data from corresponding oxygen mass transfer experiments, it is demonstrated that this adaptive mass transfer model provides an excellent description for both the local and global mass transfer of oxygen in a semibatch gas–liquid Taylor–Couette reactor for a wide range of azimuthal Reynolds numbers and axial gas flow rates.

## 4.2 Introduction

Interphase mass transfer plays a crucial role in the design, scale-up and optimization of multiphase chemical and biological reactors. As a result, considerable effort has been expended to develop reliable correlations for estimating interphase mass transfer coefficients. For gas–liquid systems, it is usually assumed that the liquid side mass transfer resistance at gas–liquid interfaces limits interphase mass transport, and therefore gas side mass transfer resistance is neglected (Deckwer et al., 1974). Hence, the liquid side volumetric mass transfer coefficient ( $k_{La}$ ) is used to compute the overall mass transfer rate across a gas–liquid interface. However, it can be difficult to estimate  $k_{La}$  because of the many factors affecting this quantity, such as gas holdup and bubble size, slip velocity, and turbulent energy dissipation rate. These factors in turn depend non-trivially on reactor operating conditions, geometry, and physical properties of the gas and liquid phases. Some dependencies of the volumetric mass transfer coefficient on hydrodynamic, operating, and geometric parameters are illustrated in Figure 4.1.

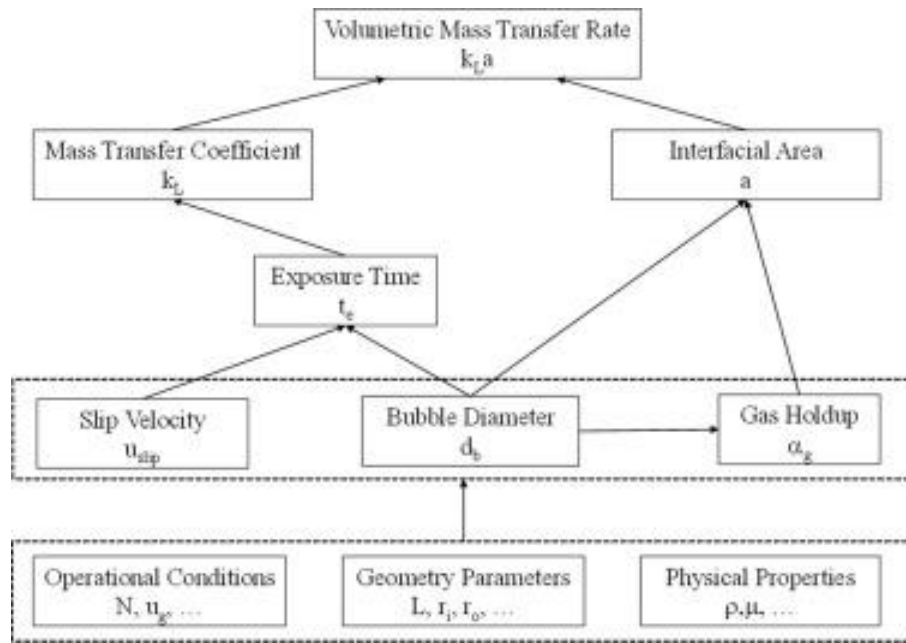


Figure 4.1 Illustration of the relationships between volumetric mass transfer coefficient and various geometric, operational, and hydrodynamic parameters.

Although numerous empirical correlations have been developed for gas–liquid mass transfer in bubble columns (Colombet et al., 2011; Gourich et al., 2006; Kawase et al., 1987; Muroyama et al., 2013), airlift reactors (Cockx et al., 2001; Huang et al., 2010; Kawase and Hashiguchi, 1996), and stirred tanks (Garcia-Ochoa and Gomez, 2005, 2004; García-Ochoa and Gómez, 1998; Özbek and Gayik, 2001a), comparatively little is known concerning interphase mass transfer in Taylor–Couette flow cells (Dłuska et al., 2004, 2001; Kadam et al., 2008; Wroński et al., 1999), which have recently gained interest for use as bioreactors (Haut et al., 2003; Kliphuis et al., 2010; Kong and Vigil, 2014, 2013; Kong et al., 2013; Qiao et al., 2014b; Sorg et al., 2011; Zhu et al., 2010). These devices, which consist of fluids confined in the annular space between two coaxial cylinders (see Figure 4.2) with the inner cylinder undergoing rotation, can be used to generate pairs of toroidal vortices with mixing characteristics advantageous for culturing a variety of microorganisms (Haut et al., 2003; Kong and Vigil, 2014; Kong et al., 2013; Qiao et al., 2014b; Zhu et al., 2010). Specifically, as the

inner cylinder rotation speed increases above a critical value that depends upon the reactor geometry and fluid properties, the fluid undergoes transition from laminar Couette flow (circular flow with only an azimuthal component) to laminar Taylor vortex flow. Subsequent increases in cylinder rotation speed lead to higher order instabilities such as wavy vortex flow, modulated wavy vortex flow, and turbulent Taylor vortex flow (Andereck et al., 1986; Coles, 1964; Wang et al., 2005a, 2005b).

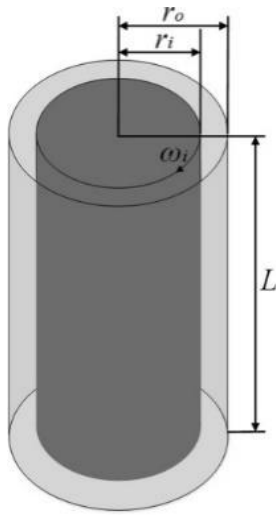


Figure 4.2 Configuration of a Taylor vortex reactor.

Although a large literature concerning single phase Taylor vortex flow has been built over many years, far less is understood concerning multiphase Taylor vortex flow, particularly with respect to mass transport in such systems. The addition of a second fluid phase leads to instabilities and flow patterns not observed in single-phase flow (e.g. phase inversions and nonhomogeneous distribution of fluid phases) (Joseph and Preziosi, 2006; Joseph et al., 1984; Renardy and Joseph, 1985; Zhu and Vigil, 2001a; Zhu et al., 2000). The available information for interphase mass transport in two-phase Taylor–Couette flow is even more limited, and until now, no computational or theoretical models for interphase mass transfer have been developed for this system. Most of what has previously been reported concerning interphase mass transfer

in Taylor–Couette flow is attributable to work performed by Wroński et al. (Wroński et al., 1999) and Dłuska et al. (Dłuska et al., 2004, 2001), who carried out experiments in a continuously-fed horizontally-oriented gas–liquid Taylor–Couette reactor and observed volumetric mass transfer coefficients with values on the order of  $0.1 \text{ s}^{-1}$ . However, the flow patterns generated in a horizontal gas–liquid reactor are significantly different from those that are produced in a vertically oriented reactor, because axial symmetry is destroyed in a horizontal reactor by the vertical gravity field that gives rise to a non-axisymmetric buoyant force.

In contrast to horizontally oriented gas–liquid Taylor–Couette reactors, the buoyant force acting on gas bubbles is parallel to the cylinder axis in vertically oriented reactors. As a result, effluent gas can easily be separated from the liquid phase by feeding gas through the bottom of the reactor and by providing sufficient head space for bubbles to rupture as they emerge from the liquid free surface at the top of the reactor. Such a configuration is particularly useful for delivery of carbon dioxide and removal of oxygen during the culture of phototrophic microorganisms. Interest in vertically oriented gas–liquid Taylor vortex reactors has also been driven by the discovery of the existence of nontrivial bubble distributions and dramatic drag reduction on the rotating inner cylinder (Chouippe et al., 2014; Maryami et al., 2014; van Gils et al., 2013; Van Gils et al., 2011).

Recently the authors carried out oxygen transport experiments in a vertical gas–liquid Taylor–Couette reactor (Ramezani et al., 2015). They found that gas–liquid mass transfer coefficients in the vertical reactor were significantly smaller than those reported for horizontal reactors. In addition, the authors developed empirical correlations for the mass transfer coefficient and the mean bubble diameter as functions of the liquid azimuthal Reynolds number

and the gas axial Reynolds number. While these correlations are useful for understanding the relative contributions of the azimuthal and axial flows in determining the magnitude of mass transfer coefficients, they cannot easily be generalized because (a) Taylor vortex flow patterns cannot be predicted based solely upon axial and azimuthal Reynolds numbers (they also depend upon reactor geometry) and (b) Taylor vortex flow is known to exhibit flow pattern multiplicity, depending upon flow history (Andereck et al., 1986).

In view of the above discussion, it is evident that the prediction of interphase mass transport coefficients for arbitrary Taylor–Couette reactor geometries and operating conditions requires an approach that incorporates details of the fluid flow. To that end, and by making use of our recently-developed computational fluid dynamics simulations for two-phase Taylor vortex flow (Gao et al., 2015b), in this work we compute interphase mass transfer coefficients by integrating local fluid velocity and phase distribution information into well-known theoretical models for interfacial mass transport. This method for computing mass transfer coefficients is then validated by comparing model predictions against our existing experimental data for interphase mass transport in a vertical Taylor–Couette gas–liquid reactor (Ramezani et al., 2015). Indeed, by properly selecting the mass transport model appropriate to the fluid flow regime, we demonstrate that this computational approach is capable of reproducing experimental data with high accuracy. Consequently, by making use of information obtained from the computational fluid dynamics (CFD) simulations that is difficult to obtain experimentally, we are able to identify the mechanisms that most strongly impact interphase mass transfer in vertical gas–liquid Taylor–Couette devices.

The remainder of the paper is organized as follows. In Sections 4.3 and 4.4 we present the model equations and computational details for both the CFD simulations and the mass

transfer coefficient calculations. In Section 4.5 we validate the computational approach for the prediction of interphase mass transport coefficients by comparing simulation results with experimental data. The computational results are also discussed in greater detail, including consideration of factors such as gas spatial distribution and fluid flow in regions with high bubble concentrations. General conclusions are presented in Section 4.6 .

### 4.3 Model equations

#### 4.3.1 CFD model for bubbly Taylor–Couette flow

In this work, the two-phase fluid flow was modeled using an Eulerian–Eulerian approach that we recently employed and validated for bubbly Taylor–Couette flow (Gao et al., 2015b). The flow was assumed to be axisymmetric (Gao et al., 2015b; Sathe et al., 2010) so that the quasi-two-dimensional mass, momentum, and species transport equations include an axisymmetric azimuthal velocity component:

$$\frac{\partial}{\partial t} (\alpha_k \rho_k) + \nabla \cdot (\alpha_k \rho_k \vec{u}_k) = S_{pk} \quad (4.1)$$

$$\begin{aligned} \frac{\partial}{\partial t} (\alpha_k \rho_k \vec{u}_k) + \nabla \cdot (\alpha_k \rho_k \vec{u}_k \vec{u}_k) = & -\alpha_k \nabla p + \nabla \cdot (\bar{\bar{\tau}}_k + \bar{\bar{\tau}}_k^{Re}) + S_{pk} \vec{u}_{pk} \\ & + \alpha_k \rho_k \vec{g} + \vec{F}_{Ik} \end{aligned} \quad (4.2)$$

$$\frac{\partial}{\partial t} (\alpha_k \rho_k Y_k^i) + \nabla \cdot (\alpha_k \rho_k \vec{u}_k Y_k^i) = -\nabla \cdot (\alpha_k \vec{j}_k^i) + S_{pk}^i \quad (4.3)$$

Here,  $\alpha_k$  and  $\vec{u}_k$  are the phase volume fraction and the phase velocity, respectively.  $Y_k^i$  is the mass fraction of species  $i$  in phase  $k$ . The term  $S_{pk}$  is the rate of mass transfer from phase  $p$  to phase  $k$ . The phase stress and Reynolds stress tensors are represented by  $\bar{\bar{\tau}}_k$  and  $\bar{\bar{\tau}}_k^{Re}$ , respectively.  $\vec{j}_k^i$  and  $S_{pk}^i$  represent the diffusive flux and the net rate of appearance of species  $i$

due to interphase mass transfer. The term  $F_{lk}$  is the interphase momentum exchange term, which can be decomposed into at least five independent interphase forces (Gao et al., 2015b, 2013):

$$\vec{F}_{lk} = \vec{F}_D + \vec{F}_L + \vec{F}_{VM} + \vec{F}_W + \vec{F}_T \quad (4.4)$$

These interphase forces represent drag, lift, virtual mass, wall lubrication, and turbulent dispersion, respectively. The constitutive relations and model constants are summarized in Table 4.1 and Table 4.2, respectively. The rationale for the selection of these five interphase forces is as follows. In a recent report on simulation of turbulent gas–liquid Taylor–Couette flow, it was demonstrated that the radial bubble distribution depends primarily upon the competition between the radial pressure gradient, the turbulent dispersion force, and to a lesser extent wall lubrication forces (Gao et al., 2015b). However, because the axial motion of bubbles is driven by buoyancy, it can be expected that the same interphase forces important for accurately simulating bubble columns, namely drag, virtual mass, and lift forces, must also be included in the analysis (Monahan and Fox, 2007). A fuller discussion of various interphase force terms can be found in the recent review article by Buffo and Marchisio (Buffo and Marchisio, 2014).

Table 4.1 Constitutive relations for bubbly Taylor–Couette two-fluid model (Gao et al., 2015b, 2013).

Drag force (TOMIYAMA et al., 1998)	$\vec{F}_{Dg} = -\vec{F}_{DI} = \frac{3}{4} \alpha_g \alpha_l \frac{\rho_l}{d_b} C_D  \vec{u}_g - \vec{u}_l  (\vec{u}_l - \vec{u}_g)$
	$C_D = \max \left( \min \left( \frac{24}{Re_b} (1 + Re_b^{0.687}), \frac{72}{Re_b} \right), \frac{8Eo}{3(Eo+4)} \right)$
Lift force (Drew and Lahey, 1993)	$\vec{F}_{Lg} = -\vec{F}_{LI} = -C_L \alpha_g \rho_l (\vec{u}_l - \vec{u}_g) \times (\nabla \times \vec{u}_l)$
Virtual mass force (Antal et al., 1991)	$\vec{F}_{VMg} = -\vec{F}_{VMI} = -C_{VM} \alpha_g \rho_l \left[ \frac{d}{dt} (\vec{u}_l - \vec{u}_g) + (\vec{u}_l \cdot \nabla \vec{u}_l - \vec{u}_g \cdot \nabla \vec{u}_g) \right]$
Wall lubrication force (Antal et al., 1991)	$\vec{F}_{Wg} = -\vec{F}_{WI} = -\frac{\alpha_g \rho_l  \vec{u}_g - \vec{u}_l ^2}{d_b} \max \left[ 0, (C_1 + C_2 \frac{d_b}{y}) \right] \vec{n}_r$
Turbulent dispersion force (Behzadi et al., 2004; Huang et al., 2010; Talvy et al., 2007)	$\vec{F}_{Tg} = -\vec{F}_{TI} = -\rho_l \overline{u'_g u'_l} \nabla \alpha_g = -C_T \rho_l k_l \nabla \alpha_g$

Table 4.2 Constants in bubbly Taylor–Couette two-fluid model (Gao et al., 2015b).

$C_L$	$C_{VM}$	$C_1$	$C_2$	$C_T$
0.02	0.5	-0.01	0.05	2

The source terms attributable to interphase mass transport,  $S_{pk}$ , depend upon the specific physical system under consideration. In this work we seek to validate our computational approach by comparing simulation predictions with our experiments previously reported (Ramezani et al., 2015). In the experiments, the feed liquid and gas phases consisted of water and a binary mixture of oxygen and nitrogen in proportions that approximate the composition of dry air, and the rate of transport of oxygen from the gas bubbles to the water phase was determined from temporal measurements of dissolved oxygen concentration in the liquid phase. Similarly, in this simulation work bubbles are assumed to be dry and the effect of water vapor on bubble physical properties and interfacial mass transfer is neglected because the saturation pressure of water vapor in the bubbles at room temperature (2310 Pa) is much smaller than the partial pressures of oxygen and nitrogen. Hence only the interphase transport of oxygen and nitrogen was considered at the bubble–liquid interface, governed by the following equation:

$$R_{gl}^i = k_L a (c_{l,*}^i - c_l^i), \quad i = \text{O}_2, \text{N}_2 \quad (4.5)$$

where  $R_{gl}^i$  is the interphase mass transfer rate of species  $i$ ,  $c_{l,*}^i = p_i/H_i$ ,  $H_i$  is the Henry's Law constant for species  $i$ ,  $k_L a$  is the volumetric mass transfer coefficient, and  $a$  is the specific interfacial area,

$$a = \frac{6\alpha_g}{d_b(1 - \alpha_g)}. \quad (4.6)$$

Thus, the total volumetric mass transfer rate can be expressed as

$$S_{gl} = \sum_{i=1}^I S_{gl}^i = - \sum_{i=1}^I \alpha_g R_{gl}^i M_w^i, \quad (4.7)$$

where  $M_w^i$  is the molecular weight of species  $i$ . Although tracking of interphase nitrogen transport was included for comprehensiveness, simulations performed with and without nitrogen transport demonstrated that no difference was found in the predictions, due to the low solubility of nitrogen in water. Consequently, it is not necessary to include interphase nitrogen transport in the model equations. Lastly, we note that care must be taken in the use of Eq. (3.6) for bubble populations with non-monodisperse distributions. In such cases, it is necessary to use the Sauter mean bubble diameter for  $d_b$ .

### 4.3.2 Turbulence modeling

In this work, the standard  $k$ - $\omega$  model was employed to simulate turbulence, as this method has been shown to accurately predict velocity fields, global gas holdup, and the spatial bubble distribution in turbulent gas–liquid Taylor–Couette flow (Gao et al., 2015b)s. Only liquid phase turbulence is considered, since the bubble phase volume fraction is very low (<2%). Indeed, we performed simulations that include bubble induced turbulence (by embedding the Sato bubble induced turbulence model into the standard turbulence model (see Sato and Sekoguchi (Sato and Sekoguchi, 1975) for details) and found no significant difference in the predictions compared to cases simulated without bubble induced turbulence. For the same reason, bubble–bubble interactions were also neglected. The turbulent kinetic energy ( $k_l$ ) and the specific dissipation rate ( $\omega_l$ ) are governed by the following transport equations (Wilcox, 1993):

$$\frac{\partial}{\partial t} (\alpha_l \rho_l k_l) + \nabla \cdot (\alpha_l \rho_l k_l \vec{u}_l) = \nabla \cdot \left( \alpha_l \left( \mu_l + \frac{\mu_{l,t}}{\sigma_k} \right) \nabla k_l \right) + \alpha_l (G_k - Y_k) \quad (4.8)$$

$$\frac{\partial}{\partial t} (\alpha_l \rho_l \omega_l) + \nabla \cdot (\alpha_l \rho_l \omega_l \vec{u}_l) = \nabla \cdot \left( \alpha_l \left( \mu_l + \frac{\mu_{l,t}}{\sigma_\omega} \right) \nabla \omega_l \right) + \alpha_l (G_\omega - Y_\omega) \quad (4.9)$$

where  $G_k$  and  $Y_k$  represent the generation and dissipation of turbulent kinetic energy, and  $G_\omega$  and  $Y_\omega$  represent the generation and dissipation of  $\omega$ , respectively. The terms  $\sigma_k$  and  $\sigma_\omega$  represent the turbulent Prandtl numbers for  $k$  and  $\omega$ , respectively, and are both taken to be equal to 2.0. The turbulent viscosity  $\mu_{l,t}$  depends upon  $k_l$  and  $\omega_l$  as follows:

$$\mu_{l,t} = \frac{\rho_l k_l}{\omega_l}. \quad (4.10)$$

### 4.3.3 Mass transfer models

Commonly employed models for the prediction of the liquid-side mass transport coefficient for gas bubbles in a continuous liquid phase include the penetration (Higbie, 1935), eddy cell (Lamont and Scott, 1970) and laminar boundary layer models (Griffith, 1960). Thorough overviews of these and other models can be found in Huang et al. (Huang et al., 2010) and Garcia-Ochoa and Gomez (Garcia-Ochoa and Gomez, 2009). The laminar boundary layer model is written as

$$k_L = C \sqrt{\frac{u_{\text{slip}}}{d_b}} D_L^{2/3} \nu_l^{-1/6}, \quad (4.11)$$

where the slip velocity is defined as  $u_{\text{slip}} = |\vec{u}_g - \vec{u}_l|$ ,  $d_b$  is the bubble diameter,  $D_L$  is the diffusivity of the solute in the liquid phase,  $\nu_l$  is the kinematic viscosity of the liquid, and  $C$  is a constant. Different values of  $C$  have been reported including 0.6 (Huang et al., 2010) and (Lochiel and Calderbank, 1964) and 0.42 (Griffith, 1960) and (Linek et al., 2004). The laminar boundary layer model can be applied only for rigid bubbles with small diameter ( $d_b < 1$  mm) or bubbles with completely immobile surface due to contamination (Alves et al., 2006). Some authors have found that the laminar boundary layer model underpredicts the mass transfer coefficient when it is applied to bubble columns or stirred tanks (Huang et al., 2010).

The penetration theory proposed by Higbie (Higbie, 1935) assumes that bubble surfaces are immobile, but it accounts for unsteady diffusion of gas into the liquid at the gas–liquid interface by introducing a characteristic gas–liquid exposure time, leading to the following expression:

$$k_L = \sqrt{\frac{4D_L}{\pi t_e}} \quad (4.12)$$

An estimate is needed for the exposure time, given by  $t_e = d_b/F^2 u_{\text{slip}}$ , where  $u_{\text{slip}}$  is the slip velocity,  $d_b$  is the bubble diameter, and where  $F$  is a constant. Substitution of the exposure time into Eq. (12) leads to

$$k_L = F \sqrt{\frac{4D_L u_{\text{slip}}}{\pi d_b}} \quad (4.13)$$

In the Higbie penetration theory for a single bubble, the constant  $F$  is taken as unity, whereas smaller values have been used by investigators when considering bubble swarms and high gas volume fractions. For instance, Wang et al. (Wang and Wang, 2007) found that the volumetric mass transfer rate in a bubble column can be well predicted using  $F=0.8$ .

The penetration theory model is known to underpredict mass transfer for highly turbulent flows, and Eq. 12 implies that this is caused by an overestimation of the exposure time. Indeed, several experimental studies of gas–liquid transport in turbulent flow have revealed that the liquid-side mass transfer is controlled by interfacial surface renewal by small scale eddies rather than by any measure of the mean flow of the liquid relative to the bubbles, such as the slip velocity (Lamont and Scott, 1970). As a result, for highly turbulent flow it is more appropriate to estimate the characteristic gas–liquid exposure time using the Kolmogorov theory of isotropic turbulence, which leads to the following eddy cell model:

$$k_L = K \sqrt{\frac{4D_L}{\pi} \left(\frac{\varepsilon_l}{v_l}\right)^{1/2}} = K' \sqrt{D_L \left(\frac{\varepsilon_l}{v_l}\right)^{1/2}}. \quad (4.14)$$

In the above equation,  $\varepsilon_l$  represents the liquid turbulence dissipation rate. Various values of the model constant  $\hat{K} = (4/\pi)^{1/2}K$  have been suggested in the literature, e.g.  $(4/\pi)^{1/2}$  (Kawase et al., 1987), 0.592 (Alves et al., 2006), 0.4 (Lamont and Scott, 1970), 0.301 (Kawase and Hashiguchi, 1996), 0.523 (Linek et al., 2004), 0.27 (Wang and Wang, 2007). Wang (Wang and Wang, 2007) has hypothesized that the inconsistency of the various estimates for  $K'$  stem from two causes including (1) the difficulty in accurately calculating turbulent dissipation rates and (2) lack of consideration of the bubble swarm effect on mass transfer.

Although the various mass transfer models discussed above find wide usage, none are appropriate for simulating all of the local conditions and flow patterns that arise in Taylor–Couette devices. Specifically, the assumptions associated with the classical penetration theory model are inconsistent with turbulent flow and lead to an overestimation of the exposure time at high cylinder rotation speeds, whereas the eddy cell model overpredicts exposure time for low dissipation rates at low rotation speeds. For this reason, we introduce an adaptive mass transfer model that combines the strengths of both models and that can be used over a wide range of Reynolds numbers and at all locations in the reactor. Specifically, by computing the local exposure time for both models, the most appropriate model for given flow conditions can be selected by choosing the one that predicts the smallest exposure time. i.e.,

$$t_e = \min \left( \frac{1}{F^2} \frac{d_b}{u_{\text{slip}}}, \frac{1}{K^2} \sqrt{\frac{v_l}{\varepsilon_l}} \right). \quad (4.15)$$

Here,  $F$  and  $K$  are adjustable constants that are needed to account for the fact that the slip velocity is sensitive to the drag model used and the turbulence dissipation rate is sensitive

to the turbulence model employed. Consequently, the adaptive mass transfer model used in this work can be expressed as follows:

$$k_L = \max \left( F \sqrt{\frac{4D_L}{\pi} \frac{u_{\text{slip}}}{d_b}}, K \sqrt{\frac{4D_L}{\pi} \left( \frac{\varepsilon}{\nu_l} \right)^{1/2}} \right). \quad (4.16)$$

In order to make use of the penetration model, the eddy cell model, or the adaptive model described above, it is necessary to choose values for the model constants  $F$  and  $K$ . Although the range of previously reported values for  $F$  and  $K$  is not large, we have chosen to fit these parameters by making use of measurements reported in our experimental investigation of oxygen mass transport in gas–liquid Taylor–Couette (Ramezani et al., 2015), which is described in more detail in Section 4.5.1 . After testing several values for both  $F$  and  $K$ , these constants were taken to be  $F=1.2$  and  $K=0.35$ . These values are consistent with those used by other investigators, as was discussed previously.

#### 4.4 Simulation approach and computational details

##### 4.4.1 Overview of computational approach

As was previously mentioned, the overall strategy for computing interphase mass transfer coefficients consists of 1) performing two-phase CFD simulations in order to compute instantaneous and time-averaged velocity fields and fluid phase distributions, and 2) computing local interphase mass transfer coefficients  $k_L$  from Eq. 3.16 by using flow field predictions to estimate turbulence energy dissipation rates ( $\varepsilon$ ) and slip velocities  $u_{\text{slip}} = |\vec{u}_g - \vec{u}_l|$ . It should be noted that the Eulerian CFD approach used here requires foreknowledge of the mean gas bubble diameter, as this quantity is needed to compute components of the interfacial momentum exchange rate  $F_{lk}$ , such as drag and virtual mass. Furthermore, once the

mean bubble diameter is specified and the resulting gas holdup is computed, the specific surface area can also be computed from Eq. 3.6, and subsequently interphase mass transfer rates can be determined. For this reason, and also to validate the computational approach with experiments, the simulations reported here were performed using the same geometry and fluids corresponding to the experimental conditions used by Ramezani et al. (Ramezani et al., 2015), who developed the following correlations for the volumetric mass transfer coefficient and mean bubble size in a vertical gas–liquid Taylor–Couette reactor:

$$\text{Sh} = \frac{k_L a d_b^2}{D_L} = 1.45 \times 10^{-7} \text{Re}_a^{0.83} \left( \text{Re}_\theta + 1.47 \times 10^4 \right)^{1.61} \quad (4.17)$$

$$\frac{d_b}{r_o - r_i} = 1.0 \times 10^{-5} \text{Re}_a^{0.11} \left( \text{Re}_\theta + 3.3 \times 10^4 \right)^{0.91} \quad (4.18)$$

In the above expressions  $d_b$  is the Sauter mean diameter,  $\text{Re}_a$  is the axial Reynolds number based upon the gas flow rate, and  $\text{Re}_\theta$  is the azimuthal Reynolds number based upon the liquid phase fluid properties. Hence, the mean bubble sizes needed to carry out the CFD simulations were obtained from Eq. 3.18, and the resulting simulation predictions for  $k_L$  were compared against those given by Eq. 3.17.

#### 4.4.2 Computational domain and boundary conditions

A schematic of the Taylor–Couette apparatus used in the experiments of Ramezani et al. (Ramezani et al., 2015) and in the simulations presented here is shown in Figure 4.3. The rotating inner cylinder has an outer radius of 3.81 cm and the fixed transparent acrylic outer cylinder has an inner radius of 5.08 cm, resulting in a gap width of 1.27 cm. The length of the reactor is 50.8 cm and the reactor is filled to a height of  $h=48$  cm, thus the total liquid working volume within the reactor is 1.70 L. The corresponding radius ratio and aspect ratio of the apparatus are given by  $\eta=r_i/r_o=0.75$  and  $\Gamma=h/(r_o-r_i)=40$ , respectively.

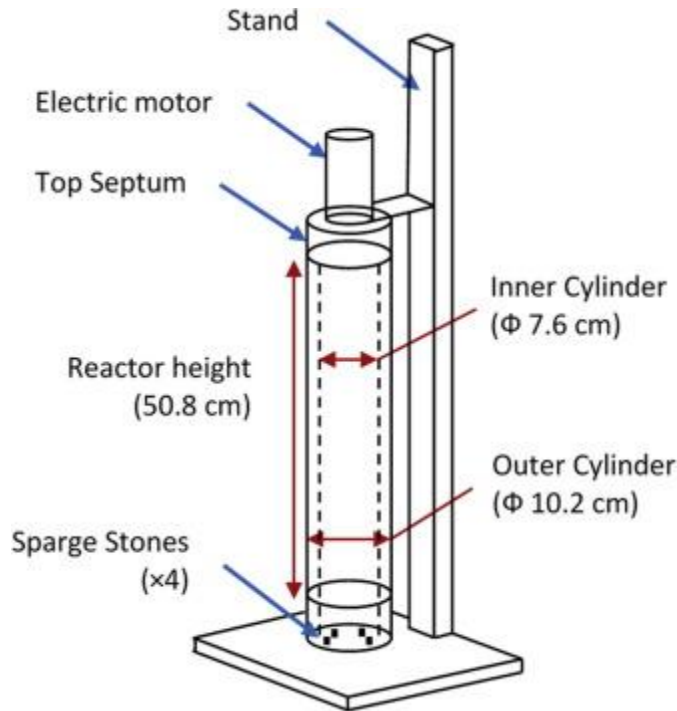


Figure 4.3 Schematic of Taylor–Couette bioreactor used for mass transfer experiments (Ramezani et al., 2015).

A non-uniform rectangular mesh was employed to simulate the annular flow chamber, and three progressively finer mesh resolutions ( $20 \times 240$ ,  $32 \times 480$ ,  $50 \times 720$ ) radial $\times$ axial nodes were tested until a grid-independent solution was obtained. Because no differences were observed in the solution between the two finest grids tested, all subsequent computations were performed using the  $32 \times 480$  mesh. It should be noted that in the near-wall regions a finer grid spacing was used (8 grid points within 2.5 mm of either wall) to capture steep gradients associated with the no-slip boundary conditions. The first layer of grid points was located within the viscous sublayer at wall units  $y^+ = 3.3$  and 5.0 for the inner and outer cylinders, respectively.

The reactor operated in a semi-batch mode with continuous flow of gas and no feed or removal of liquid. The gas inlet was modeled as a narrow channel with a width of 10 mm near the outer wall at the bottom of the reactor to mimic the feed conditions in the experiment. The

boundary at the top of the annular fluid mixture was treated as a gas outflow boundary to simulate the liquid free surface in contact with a head space. In summary, the boundary conditions used were as follows. No-slip conditions were used at solid boundaries, and the azimuthal velocity of the inner cylinder was chosen to match experimental conditions. A fixed gas velocity was prescribed at the gas inlet at the bottom of the reactor and by specifying an inlet bubble volume fraction of 0.05. Pressure outlet boundary conditions were used for both fluid phases.

Simulations were initialized assuming that only the liquid phase occupied the annular flow chamber so that  $\alpha_g=0$ . Subsequently, the momentum, mass, and species conservation equations described above were solved in double precision using the commercial finite volume CFD code, ANSYS FLUENT 14.5 (Ansys Inc., US). The interphase mass transfer model was embedded into the CFD code with the aid of user defined functions (UDFs). The pressure–velocity coupling was resolved using the SIMPLE algorithm (Patankar, 1980). Transient CFD simulations were carried out using a time step of  $5 \times 10^{-4}$  s. Generally, 30–60 s of simulated physical time was required to reach a quasi-steady state wherein the global gas volume fraction did not change with time.

#### 4.5 Results and discussion

In our previous work (Gao et al., 2015b), the two-fluid model described in Section 4.3 was validated by direct comparison of simulated results with velocity and phase distribution data from experiments performed by Murai et. al. (Murai et al., 2005), who carried out studies of a vertical semibatch gas–liquid Taylor–Couette reactor. Consequently, we focus here on model predictions for mass transfer calculations.

#### 4.5.1 Selection of mass transfer model parameters

As was mentioned in Section 4.3.3 , the penetration, eddy cell, and adaptive mass transfer models require specification of the model constants  $F$  and  $K$ . The values used here ( $F=1.2$ ,  $K=0.35$ ) were obtained by fitting simulation predictions for the penetration and eddy cell models to data from corresponding experiments described in our earlier work (Ramezani et al., 2015). Specifically, in order to select the optimal value of  $F$ , simulations of gas–liquid oxygen mass transfer using the penetration model (3.13) were performed for several values of  $F$  and for the lowest rotation speed considered, and the volumetric averaged values of  $k_{LA}$  were compared with experimentally determined values. A similar procedure was used to select the optimal value of  $K$ , except that simulations were performed using the eddy cell mass transfer model (3.14) and compared with data from experiments performed at the highest rotation speeds considered.

#### 4.5.2 Validation of adaptive mass transfer model

Axially averaged plots of the radial distribution of the simulated volumetric mass transfer coefficient using different theoretical models are shown in Figure 4.4(a). Specifically, calculations were performed using the laminar boundary layer (Eq. 3.11), penetration (Eq. 3.13), eddy cell (Eq. 3.14), and adaptive (Eq. 3.16) models. It can be seen from these plots that interphase mass transfer is virtually non-existent in the reactor except near the inner cylinder, because that region is where most of the gas is located (Figure 4.4(b)).

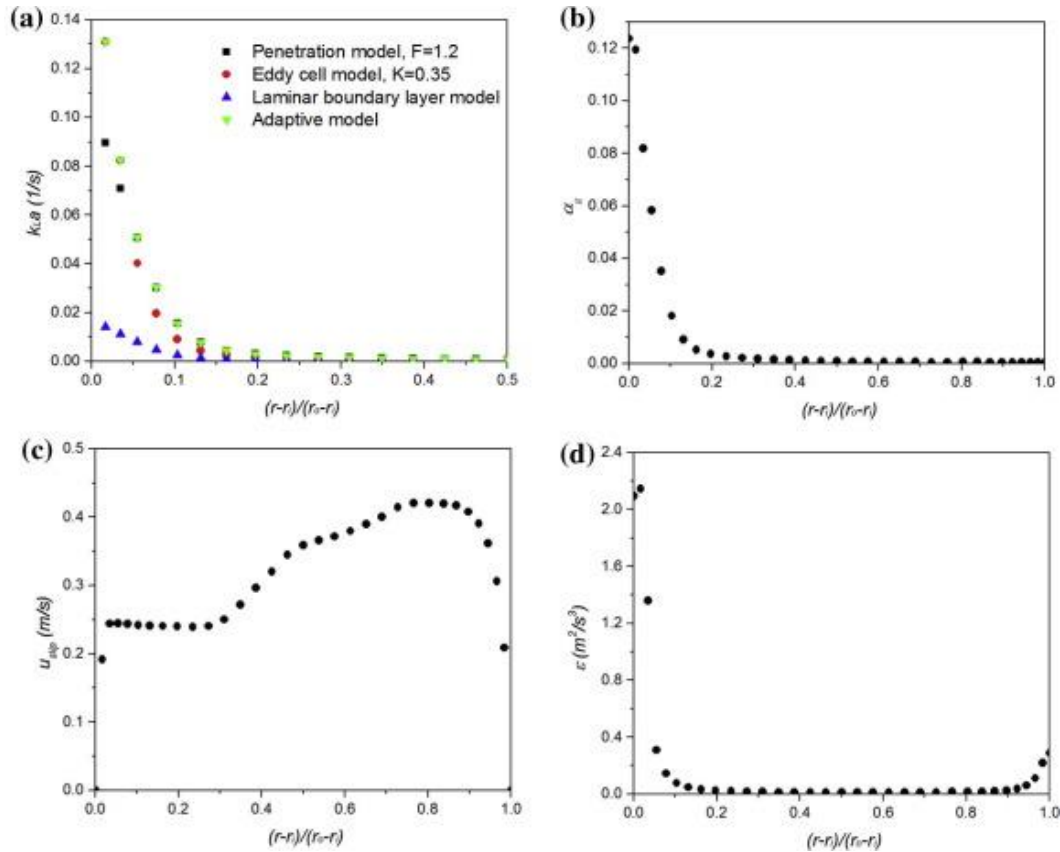


Figure 4.4 Axially averaged radial distributions of (a) volumetric mass transfer coefficient (1/s), (b) gas volume fraction, (c) slip velocity (m/s), and (d) turbulence dissipation rate ( $m^2/s^3$ ) for rotation speed and gas flow rate of 300 rpm and 0.235 vvm, respectively.

Comparison of the simulated spatially averaged volumetric mass transfer coefficient with experimental data is shown in Figure 4.5 and Figure 4.6 for various rotation speeds and gas flow rates. Examination of the data presented in Figure 4.5 suggests that  $k_{LA}$  is relatively insensitive to rotation speed for speeds lower than 300 rpm, but increases monotonically at higher rotation speeds. In contrast, Figure 4.6 demonstrates that the volumetric mass transfer coefficient increases with increasing gas flow rate over the entire range of cylinder speeds studied. In all cases considered, mass transfer coefficients computed using the laminar boundary layer model are significantly lower than the corresponding experimental values, as is expected since the flow conditions do not satisfy the laminar boundary layer model

assumptions. As expected, the penetration model, which relies on slip velocity to estimate characteristic gas–liquid exposure time, produces values of  $k_L a$  very close to experimental values observed at low rotation speeds, whereas it fails at the higher rotation speeds studied. In contrast, the eddy cell model is more accurate for high cylinder rotation speeds but produces values that are too low at the lower rotation speeds. These results are consistent with findings of Alves et al. (Alves et al., 2006), who showed that the penetration model can be used to calculate bubble mass transfer coefficients for turbulent dissipation rates up to at least  $\varepsilon \approx 0.04 \text{ m}^2/\text{s}^3$ . For the calculations presented in Figure 4.5 and Figure 4.6, the penetration model becomes inaccurate for spatially averaged turbulent dissipation rates larger than approximately  $0.1 \text{ m}^2/\text{s}^3$ . Fortunately, the eddy cell model accurately predicts the volumetric mass transfer coefficient when the turbulent dissipation rate is larger than  $0.1 \text{ m}^2/\text{s}^3$ . Consequently, the proposed adaptive mass transfer model (Eq. 3.16) combines the advantages of both the penetration and eddy cell models in order to produce good global predictions over a wide range of turbulent flow conditions by automatically selecting the most appropriate mass transfer model for local conditions. A few exceptions occur at high rotation speeds and low gas flow rates, where the penetration model appears to perform slightly better than the adaptive model. Further experiments under these conditions will be needed in order to determine if the selection criterion of the adaptive model can be improved, for example by accounting for the local gas holdup.

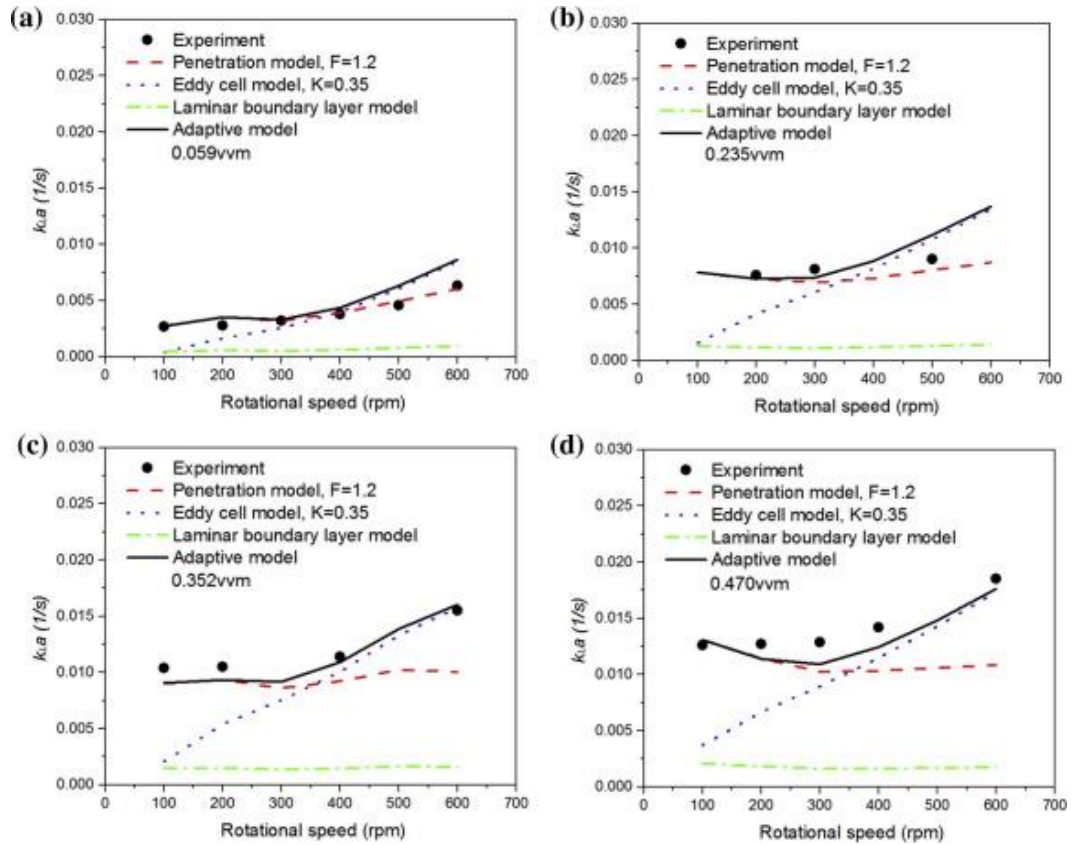


Figure 4.5 Comparison of predicted average volumetric mass transfer rate by different mass transfer models with experimental data under different rotational speeds.

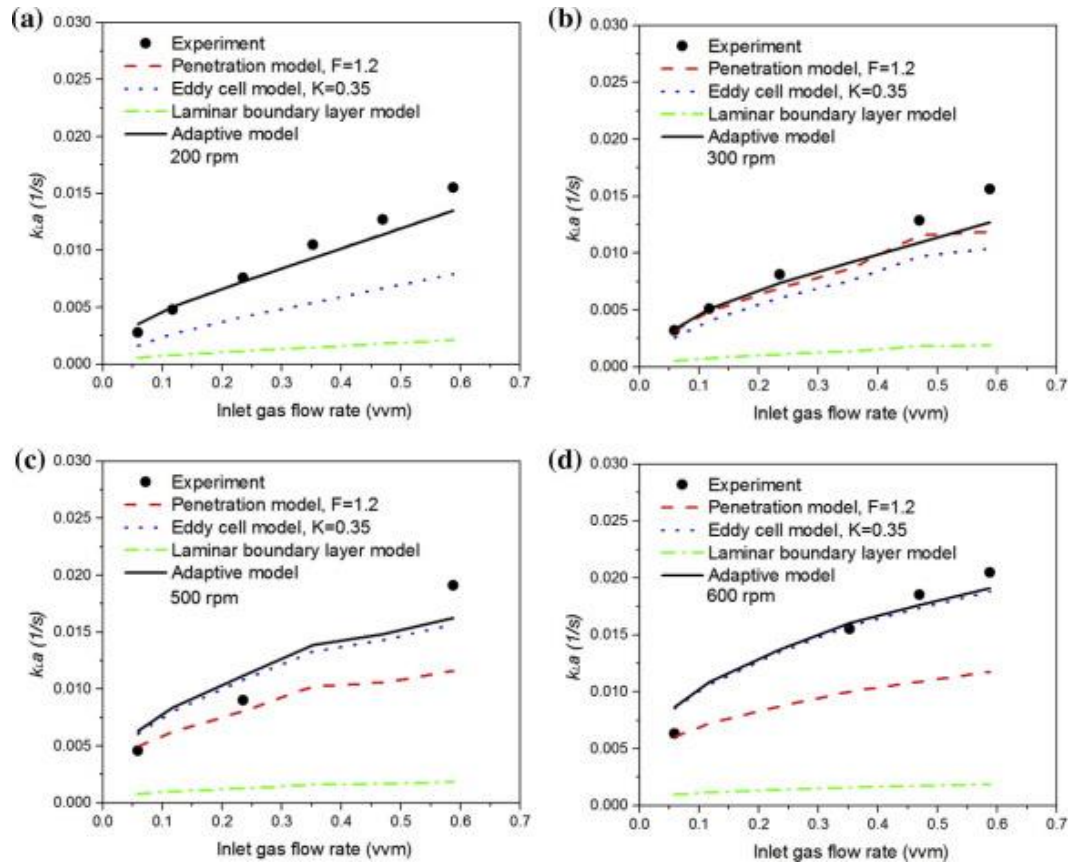


Figure 4.6 Comparison of predicted average volumetric mass transfer rate by different mass transfer models with experimental data under different inlet gas flow rates.

Although the comparison of experimental measurements with predictions based upon the adaptive mass transport model combined with CFD simulations provide evidence for the validity of the modeling approach used here, it is possible to further validate the model by comparing simulation predictions with raw experimental results. For example, in the work of Ramezani et al. (Ramezani et al., 2015), values of  $k_{LA}$  were determined by measuring dissolved oxygen in the liquid phase in response to a step change in the feed gas composition. Simulation of the evolution of dissolved oxygen concentration for one of these experiments (by including species transport equations in the CFD simulations) is shown in Figure 4.7 and compared directly to the experimental measurements. Because of startup transients associated with the experimental protocol (more fully described in (Ramezani et al., 2015)), there is a brief

induction period before dissolved oxygen is detected by the oxygen sensor. This startup transient is not observed in the simulations because mass transfer was enabled only after the two-phase fluid flow reached a steady state. In spite of these important differences, the predictions are in remarkably good agreement with the experiments.

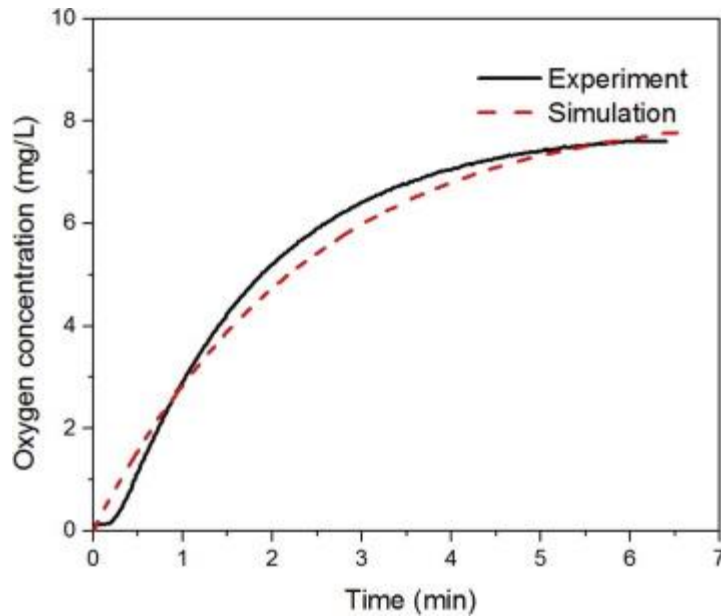


Figure 4.7 Comparison of simulated instantaneous liquid phase oxygen concentration with experimental data of a specific case (0.235 vvm, 300 rpm) at an axial location of 12.7 cm from the bottom of the reactor and near the outer cylinder wall.

We also note that Ramezani et al. (Ramezani et al., 2015) assumed (and confirmed by experiments) that the bulk liquid phase was sufficiently well mixed so that the dissolved oxygen concentration was essentially spatially uniform and therefore dissolved oxygen measurements at a single point are sufficient for determining the global value of  $k_{LA}$ . Indeed, the simulation of these experiments predicts spatial homogeneity in the distribution of oxygen in the liquid phase (not shown).

### 4.5.3 Factors influencing mass transfer rate

For the mass transfer models considered here,  $k_L$  and  $a$  are most directly impacted by slip velocity, dissipation rate and bubble diameter. These quantities in turn are determined by system operating conditions, geometrical parameters, and physical properties, as shown in Figure 4.1. Here, we discuss the impact of several factors, including quantities that are difficult to obtain from experiments but that are accessible from CFD calculations.

As was discussed previously, a priori knowledge concerning bubble diameter is required to carry out the computations. Specifically, the Sauter mean bubble diameter was estimated using the empirical correlation given by Eq. 3.18 (Ramezani et al., 2015), which depends upon both the azimuthal and axial Reynolds numbers. From this equation, it is evident that the azimuthal Reynolds number (cylinder rotation speed) has a stronger effect on bubble diameter than does the axial Reynolds number (gas flow rate). For example, a fivefold increase in rotation speed produces an increase in bubble diameter of  $\approx 50\%$ , whereas a fivefold increase in gas feed rate only results in a bubble diameter increase of  $\approx 20\%$ . These dependencies in turn have a direct effect on the specific interfacial area  $a$ , as well as indirect effects on  $k_L$  (for example by impacting the bubble drag force and slip velocity).

Figure 4.4 shows axially averaged plots for the radial distribution of gas volume fraction, slip velocity, and turbulence dissipation rate for a specific gas flow rate and rotation speed (0.235 vvm, 300 rpm), but these results are representative of all the conditions studied here. As can be seen in Figure 4.4(c), the largest slip velocities occur near the outer cylinder wall. This phenomenon can be explained by the fact that most of the gas is concentrated near the inner cylinder wall (see Figure 4.4(b)). The rising gas near the inner cylinder entrains liquid, which recirculates toward the bottom of the reactor near the gas-depleted outer cylinder. As a

result, the slip velocity near the outer cylinder is quite large, but there are very few bubbles in this region.

The dependence of the volume averaged (global) slip velocity on gas flow rate and cylinder rotation speed is depicted in Figure 4.8. Surprisingly, this quantity decreases with increasing gas flow rate. While this result may be counter-intuitive, several factors should be considered when interpreting this result. For example, the slip velocity depends upon the bubble drag. The Tomiyama drag model (TOMIYAMA et al., 1998) used here in turn has a very complicated dependence on gas flow rate, particularly as it impacts bubble diameter (Ramezani et al., 2015). In addition, gas flow rate can lead to significant changes in the flow patterns, including stretching the vortex axial wavelength (Gao et al., 2015b).

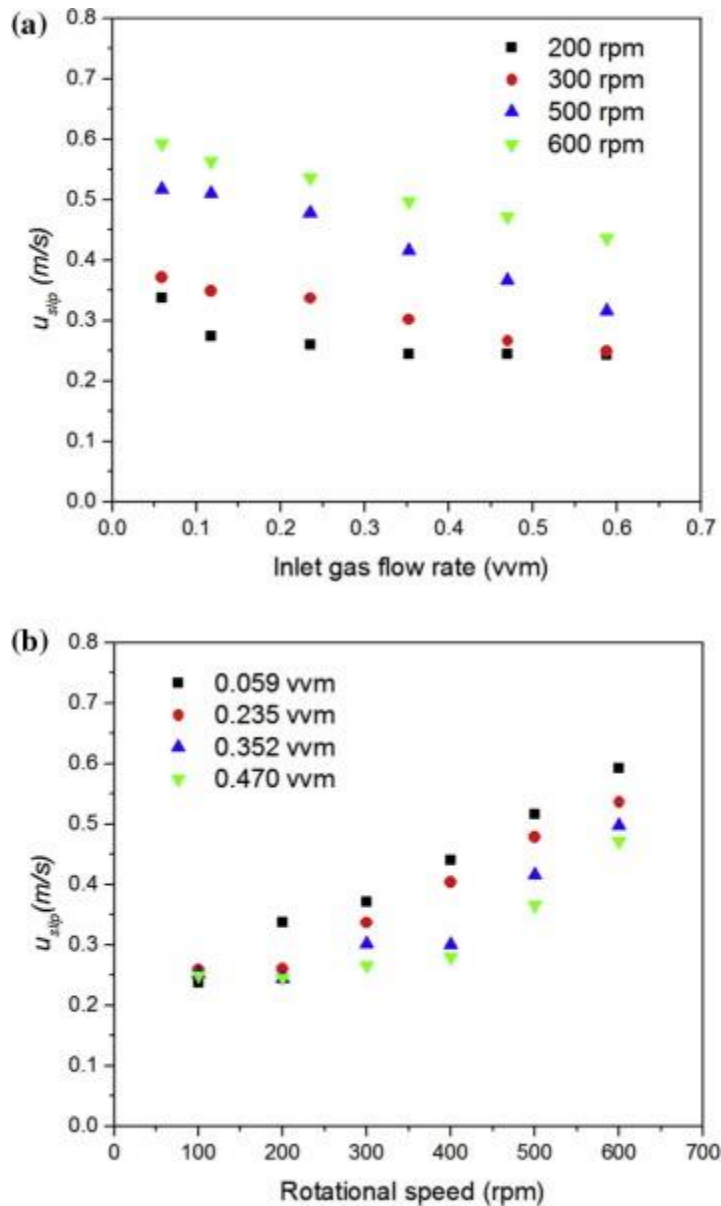


Figure 4.8 Global slip velocity as a function of inlet gas flow rate and cylinder rotation speed.

The global volume averaged turbulent kinetic energy dissipation rate is plotted in Figure 4.9 for various rotation speeds and gas flow rates, and it is apparent that this quantity is insensitive to the gas flow rate. While such a result may not be surprising since the gas phase is neglected in the turbulence model and bubble induced turbulence is not considered (due to the low gas holdup), the presence of gas could be expected to indirectly impact the dissipation rate since the liquid velocity field is influenced by the presence of gas bubbles. In contrast,  $\varepsilon$

increases rapidly with cylinder rotation speeds above 300 rpm. Furthermore, the turbulence dissipation rate is much larger near the cylinder walls than in the middle of the annulus, as is evident from Figure 4.4(d).

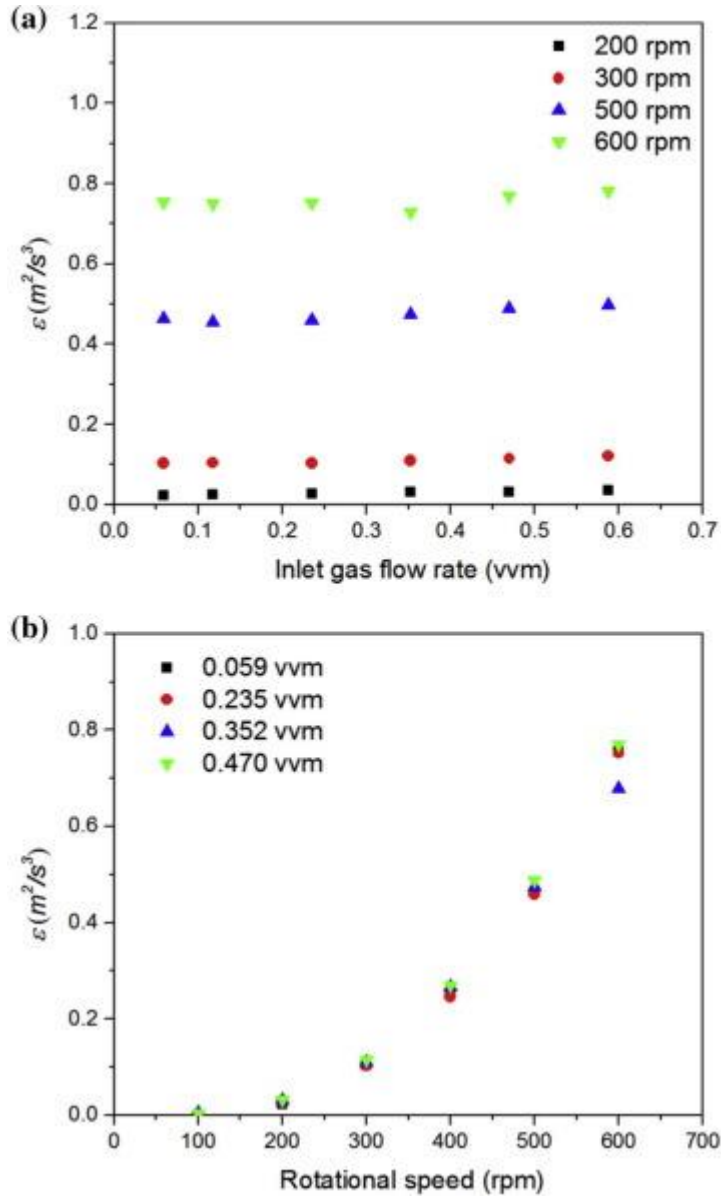


Figure 4.9 Global turbulent dissipation rate as a function of inlet gas flow rate and cylinder rotation speed.

The simulated global gas holdup, which was obtained by spatial averaging, is shown in Figure 4.10 for the case of no cylinder rotation, and these results are compared with

experimental data from our previous work (Ramezani et al., 2015). Although the predicted gas holdup agrees well with the experimental data for a wide range of inlet gas flow rates tested, the simulated gas holdup is slightly but consistently lower than the experimental data, particularly at the higher gas flow rates considered. This discrepancy can probably be attributed to one or both of two causes, including 1) errors in estimates of the bubble diameter in Eq. 3.18 at high gas flow rates, due to the fact that in such cases individual bubbles are difficult to distinguish because of the presence of bubble swarms (Ramezani et al., 2015) and 2) errors associated with the drag model when bubble swarms are present. Indeed, the Tomiyama (TOMIYAMA et al., 1998) drag model used in this study was developed for single bubbles rather than for bubble swarms, and subsequent studies of drag on bubble swarms in bubble columns (Simonnet et al., 2007) and (Roghair et al., 2013) have demonstrated that corrections are required, although no such correction currently exists for gas–liquid Taylor–Couette flow.

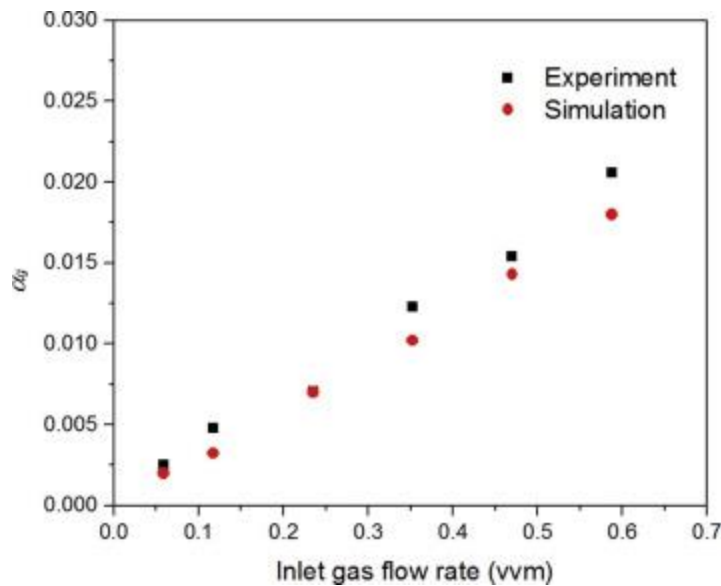


Figure 4.10 Comparison of simulated volume averaged gas holdup with experimental data for the case of no cylinder rotation.

For cases with rotation of the inner cylinder (turbulent Taylor–Couette flow), the predicted global gas holdup is shown in Figure 4.11 for various gas flow rates and rotation speeds. No experimental data are available for comparison, because the liquid free surface at the top of the reactor has a complex topography when the inner cylinder rotates, and therefore it is difficult to accurately measure global gas holdup. It can be seen from Figure 4.11(a) that for constant cylinder rotation speed, gas holdup increases approximately linearly with the inlet gas flow rate. In contrast, for fixed inlet gas flow rate, the gas holdup is relatively insensitive to rotation speeds below 300 rpm ( $Re_{\theta}=15200$ ), whereas it increases approximately linearly for rotation speeds above this value.

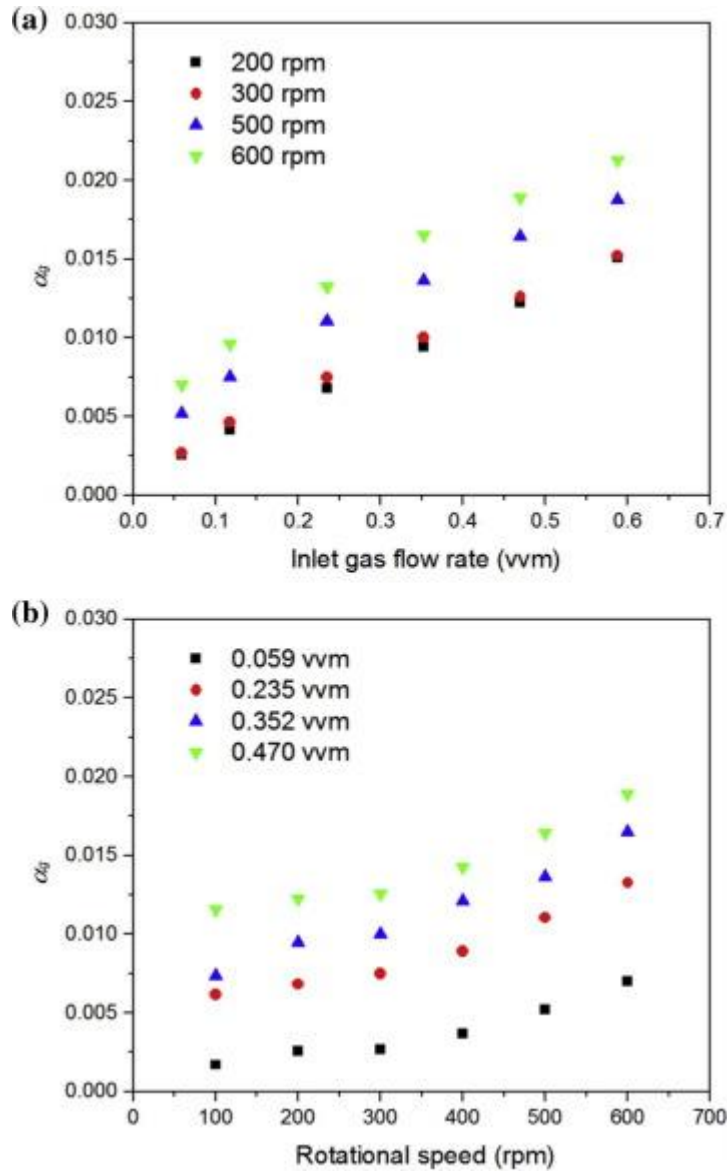


Figure 4.11 Predicted global volume averaged gas fraction as a function of inlet gas flow rate and rotational speed.

In view of the non-uniform spatial distribution of slip velocity and turbulent kinetic energy dissipation, it is important to understand not only how the global gas holdup depends upon operating parameters, but also how the spatial distribution of gas is affected. Returning to Figure 4.4(a), this plot demonstrates that bubbles concentrate near the inner cylinder wall, driven by the strong centrifugal force (Gao et al., 2015b), as was discussed previously. Note

that Fig. 4(d) shows that this region is also characterized by high dissipation rates. The same results occur for the other flow conditions studied with cylinder rotation, and together these findings demonstrate that interphase mass transport is mainly confined to the region near the inner cylinder, which is discussed further in the next section.

#### 4.5.4 Mass transfer coefficients and interfacial area

Although globally averaged values of  $k_L a$  were computed in order to compare model predictions to experimental findings, a deeper understanding of the relationship between this quantity and reactor operating conditions can be obtained by examining the local and global dependencies of the specific interfacial area,  $a$ , and the mass transfer coefficient,  $k_L$ , individually. For example, typical local values of the mass transfer coefficient  $k_L$  computed using the adaptive model are shown in the spatial contour plot in Figure 4.12(a), whereas the local specific interfacial area  $a$ , which was computed based upon knowledge of the gas spatial distribution and the mean bubble diameter, is presented in Figure 4.12(b). Figure 4.12(a) and Figure 4.12(b) demonstrate that the mass transfer coefficient is much more uniformly distributed (although there are enhancements near both cylinders) than is the specific interfacial area, because the latter quantity depends upon the local gas volume fraction. The enhanced values of the mass transfer coefficient near the inner and outer cylinders reflect the corresponding distributions of turbulent energy dissipation rate and slip velocity discussed previously and depicted in Figure 4.4.

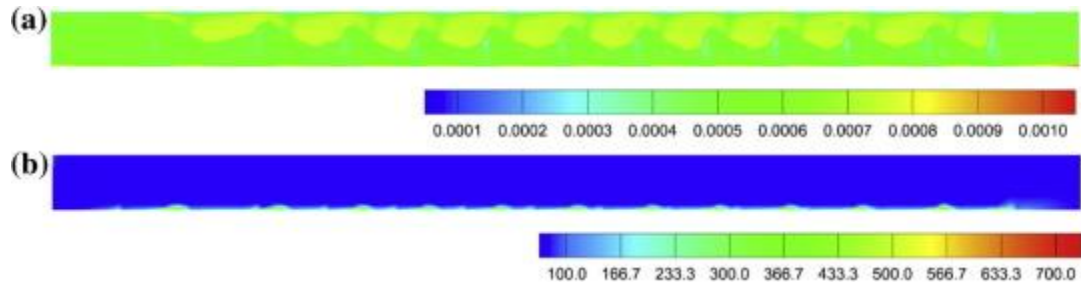


Figure 4.12 Contour plots of (a) mass transfer coefficient  $k_L$  (m/s) predicted by the adaptive mode and (b) specific interfacial area  $a$  ( $m^2/m^3$ ) for a gas flow rate of 0.235 vvm and cylinder rotation speed of 300 rpm. In each plot, the inner cylinder wall is represented by the bottom boundary and the outer cylinder wall is represented by the top boundary.

The effect of inlet gas flow rates and rotation speeds on the global spatially averaged values of the mass transfer coefficient and the interfacial area are shown in Figure 4.13 and Figure 4.14. Interestingly, the global mass transfer coefficient decreases with increasing gas flow rate at constant cylinder rotation speed. This result can be understood by considering how increased gas flow rate impacts local mass transfer coefficients, which are computed using Eq. 3.16. In particular, we note that for regions with high turbulence dissipation rates,  $k_L$  is governed by the eddy cell model, which is essentially independent of the gas flow rate because the turbulence dissipation rate is insensitive to gas flow rate (Figure 4.9(a)) for the conditions studied. In regions with low dissipation rates,  $k_L$  is governed by the penetration theory model, which has a more complicated dependence on gas flow rate. Specifically, as was discussed previously the slip velocity decreases while bubble diameter increases with increasing gas flow rate, thereby causing the local value of  $k_L$  to decrease. Hence, increasing the feed gas flow rate leads to reduced local values of the mass transfer coefficient in regions governed by the penetration theory model and unchanged values in high dissipation rate regions governed by the eddy cell model, thereby leading to an overall decrease in the global mass transfer coefficient.

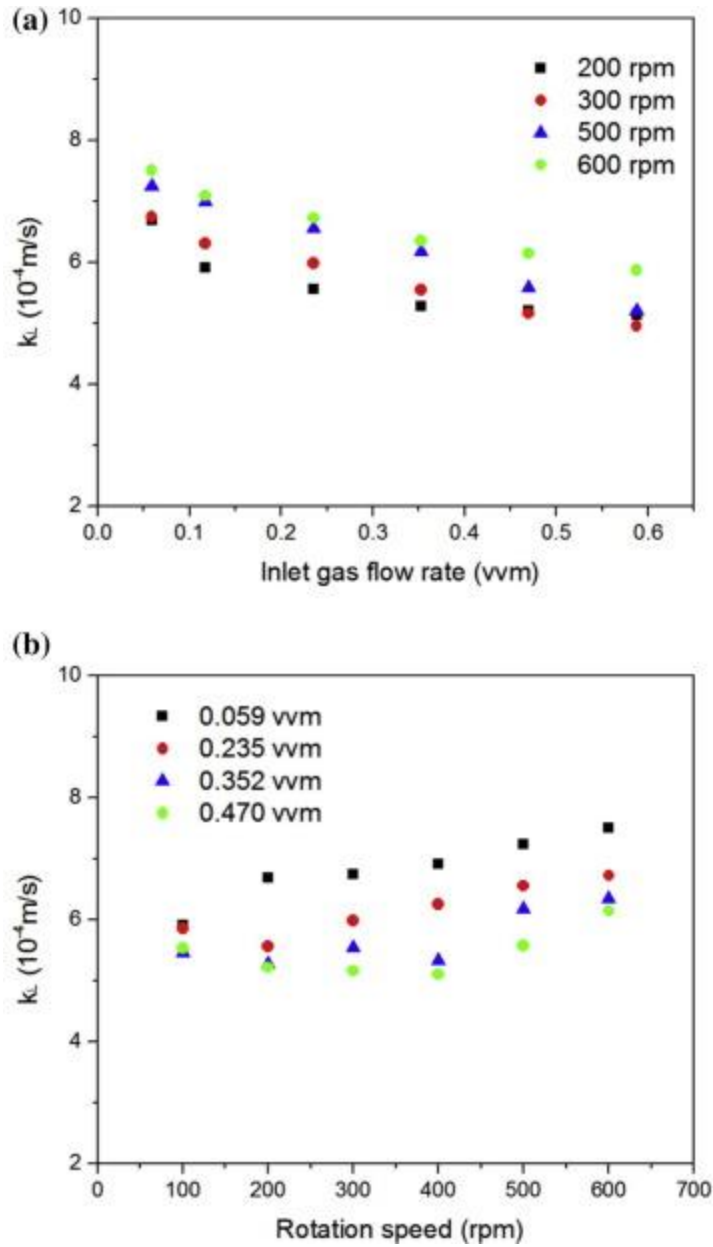


Figure 4.13 Predicted average mass transfer coefficients by the adaptive mass transfer model under different rotational speeds and inlet gas flow rates.

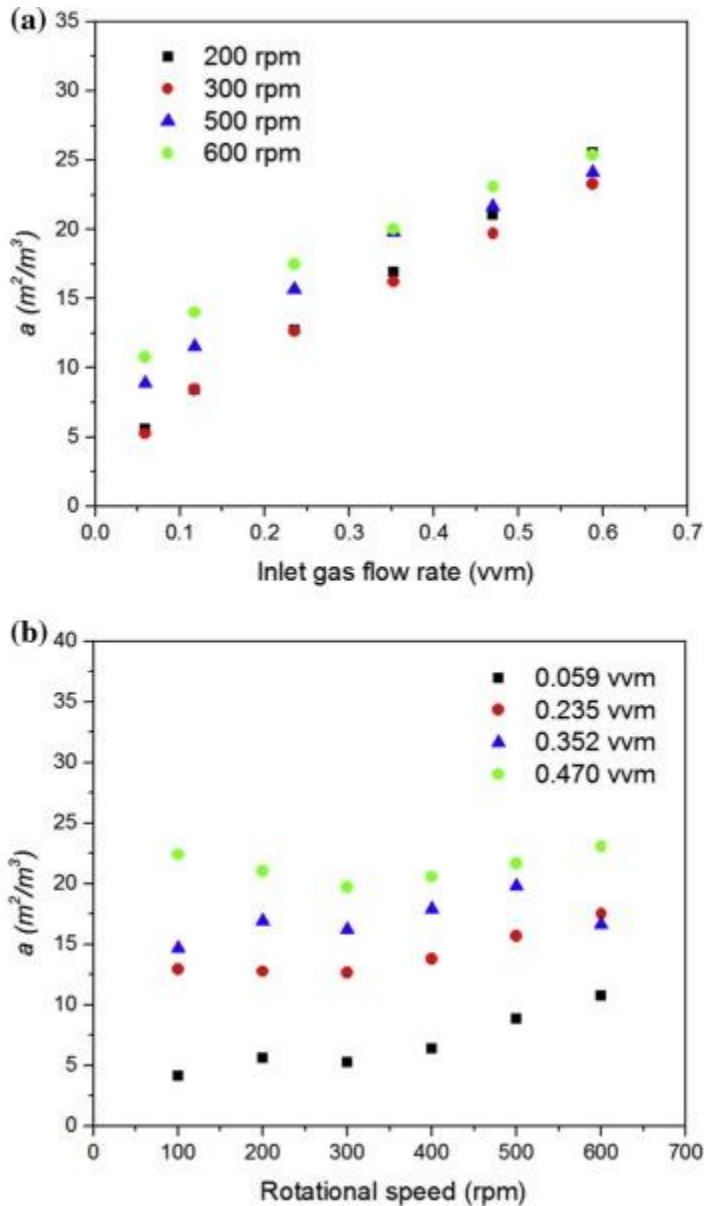


Figure 4.14 Predicted specific interfacial area as a function of cylinder gas flow rate and cylinder rotation speed.

Figure 4.14 demonstrates that specific interfacial area, which depends upon both the gas holdup and bubble diameter, increases rapidly with gas flow rate. In contrast, for cylinder rotation speeds less than 300 rpm, the specific interfacial area is insensitive to rotation speed. Above 300 rpm, the specific interfacial area increases weakly with rotation speed. In view of the results shown in Figure 4.13 and Figure 4.14, the monotonic increase of the volumetric

mass transfer coefficient  $k_{LA}$  with gas flow rate, which was also observed in corresponding experimental work (Ramezani et al., 2015) and reflected in Eq. 3.17, is a result of the rapid increase in specific interfacial area,  $a$ , even while  $k_L$  decreases with increasing gas flow rate. In contrast to the dependence on gas flow rate,  $k_{LA}$  is essentially independent of cylinder rotation rate for cylinder speeds below 300 rpm, but at higher speeds increases rapidly due to increases in both  $k_L$  and  $a$ . This more complicated dependence of  $k_{LA}$  on cylinder rotation speed is also mirrored and confirmed by Eq. 3.17.

#### 4.6 Conclusions

Gas–liquid mass transfer in a Taylor vortex reactor was simulated by using a two-fluid CFD model to obtain local phase distribution and velocity field information, which is then used to select an appropriate mass transfer model for computing the volumetric mass transfer coefficient,  $k_{LA}$ . The two-fluid model, which was previously validated by comparing velocity and phase distribution predictions with experimental measurements in a vertically oriented semibatch gas–liquid Taylor vortex flow device (Gao et al., 2015b), accounts for two-way coupling of several interphase forces including drag, virtual mass, lift, wall lubrication, and turbulent dispersion. The mass transfer model is based upon the Higbie theory, but automatically adapts to the local hydrodynamic environment by computing exposure time using either the penetration theory or eddy cell model based upon the turbulence dissipation rate. This adaptive approach was shown to provide much more accurate predictions for the volumetric mass transfer coefficient than does either model used alone.

After developing the approach described above, the effects of several important operating conditions on local and global mass transfer coefficients were explored. For all flow conditions studied, gas bubbles congregate near the inner cylinder, and therefore most

interphase mass transfer also is located near the inner cylinder wall. The cylinder rotation speed, in contrast to the gas feed flow rate, strongly impacts the bubble diameter, slip velocity, and turbulence dissipation rate. The gas flow rate has a greater effect than the cylinder speed on gas holdup,  $\alpha_g$ , but because the holdup is small (<2%) even for the highest gas flow rates studied, the rate of interphase mass transfer in general depends more strongly on the azimuthal Reynolds number, in agreement with experimental findings for this system (Ramezani et al., 2015).

Further evidence for the validity of the modeling approach described here was obtained by comparing simulation predictions with experimental measurements for the temporal evolution of the concentration of dissolved oxygen at a specific location in the reactor in response to a step change in feed gas composition. A key assumption in determining mass transfer coefficients from the experimental measurements is that the liquid mixing time is short compared to the characteristic mass transfer time. The simulations support this assumption, and consequently the hypothesis that measurements at a single location in the reactor are sufficient for determining the mass transfer coefficient appears to be justified. Lastly, we note that determination of  $k_{LA}$  from experimental data at a single location also requires that the local liquid saturation concentration does not depend upon position (gas partial pressure) and only depends upon temperature. Such an assumption can be justified if the gas phase partial pressures do not vary strongly with position. In the CFD model presented here, no assumption of spatial homogeneity in the distribution of the gas phase partial pressures is invoked, and the saturation concentration  $c_{l,*}$  in Eq. 3.5 was computed locally. However, because oxygen is in great excess, the value of  $c_{l,*}$  is practically constant at all positions in the reactor, consistent with the assumption used to compute  $k_{LA}$  from the experimental data.

#### 4.7 Acknowledgments

Financial support was provided for this work by National Science Foundation Grant CBET-1236676.

## CHAPTER 5

## EXPERIMENTAL INVESTIGATION OF HYDRODYNAMIC FLUID-PARTICLE INTERACTIONS USING VELOCITY FIELD COMPARISON OF A FIXED TRAIN OF SPHERICAL PARTICLES INSIDE A SQUARE DUCT

This chapter is a manuscript under preparation for submission to Experiments in Fluids. I am the main contributor to this work.

## 5.1 Abstract

Particle Image Velocimetry (PIV) was used to measure the velocity field around a train of spherical particles inside a square duct at a Reynolds number of 100 based on the particle diameter. Various arrangements with 1, 3, and 5 particles and distance over diameter ratio of  $d/D$  of 1.38, 1.73, 2.19, 2.76, and 4.38 were studied. Temporal and spatio-temporal average of the data was shown and it was observed that the number of spheres in the arrangement barely affects the velocity field for trains with multiple spheres. It was also shown that the first sphere in the arrangement has a very different interaction with the fluid compared to the rest of the particles. It was observed that the smallest distance over diameter ratio studied here has negligible fluid penetration between the particles suggesting that the fluid interacts with the train as a cluster of particles rather than individual spheres whereas the higher particle distances allow interaction of fluid with individual particles.

## 5.2 Introduction

A fundamental understanding of multiphase flow systems requires the study of relatively complex phenomena that takes place in the micro scale. In particular to the fluid-

solid two-phase systems are effects of the fluid phase hydrodynamic (Lim et al., 1995; Mehrabadi et al., 2015) on aggregation and diffusion of solid particles, interactions of the solid phase such as elasticity and friction (Mehrabadi et al., 2012), electrostatic charges, and shape of the solid phase particles. In particular, two-phase fluid-solid flow is encountered in a variety of industrial applications (Dai and Grace, 2010; Wang et al., 2004) and perhaps the oldest one is Fluid Catalytic Cracking (FCC). Production of different monomers and polymers, Chemical Looping Combustion (CLC), pyrolysis of biomass, and gasifier plants also face similar flow systems. Design of any laboratory scale apparatus or industry scale plant requires numerical simulations which usually is performed by using two-fluid models or point-particle schemes. Use of the density-weighted average equations or point-particle assumption of these schemes bring about unknown source terms that require to be implemented in terms of closure models. A successful numerical simulation may need to predict working parameters such as flow rate, pressure drop, bed height, particle carry-over, clustering or preferential accumulation, fluid entrainment, and particle attrition.

In the study of multiphase flows, understanding the mesoscale and microscale phenomena involves studying the interaction of the dispersed phase with the continuous phase and also the interactions of the dispersed phase in presence of the continuous phase. In the context of solid-fluid two phase flows, there are several studies that are used as benchmark for validation of numerical simulations that involve flow around single bluff bodies (Achenbach, 1974; Sakamoto and Haniu, 1995; Sakamoto et al., 1990, 1989; Taneda S, 1956; Taneda, 1959), or some cases with flow around multiple bodies (Tsuji et al., 1982).

Microscale numerical simulations of multiphase flow that are validated against experiments are in turn used in order to develop closure models for macroscale simulation of

multiphase flows (Mehrabadi et al., 2015; Sun et al., 2015; Tenneti et al., 2013, 2011, 2010). With development of more recent flow visualizations methods such as Particle Image Velocimetry (PIV), it is possible to get field measurement in more complicated geometries. Recently, several studies have been done by different researchers in a variety of geometries (Ozgoren, 2013; Ozgoren et al., 2013, 2011; Pinar et al., 2013).

Current study attempts to investigate interactions of solid particles in a liquid medium by measuring flow field around inline set of spherical particles. Such measurements are of particular interest in validating multiphase flow models and also for developing a fundamental understanding of the interaction of the distributed and the continuous phases in such flows.

There is also plenty of literature available that study fluid flow around different arrangements of spherical solid particles (Chen and Wu, 2000; Johnson and Patel, 1999; Liang et al., 1996; Maheshwari et al., 2006; Ozgoren, 2013; Ozgoren et al., 2014; Prahl et al., 2007; Tsuji et al., 2003, 1982; Zhu et al., 1994). Current study focuses on experimental investigation of a simplified case of a train of successive spherical solid particles inside a liquid flowing medium confined in a square duct. The results provided in this study serves as a fundamental experimental data set for verification of multiphase flow numerical methods.

### 5.3 Experimental setup and procedure

The experimental apparatus used in this study is shown in Figure 5.1. The test section consists of a square cross section water tunnel with 149 mm width and 610 mm length made of clear acrylic. In order to get a uniform inlet flow to the test section, several layers of perforated stainless steel sheets with varying arrangements are installed in the upstream flow conditioner that provides a uniform flow of deionized water into the test section. A stationary arrangement of fused silica spheres with the diameter of 15 mm are placed inside the channel

that are held by means of a 2 mm rod attached to the back wall of the section. This wall of the section is removable and allows for varying the arrangement of the spheres from one experiment to the other one.

The flow loop outside of the test section consists of 38 mm (1½") PVC piping. Flow of De-Ionized water is maintained circulating through the flow facility by means of a March® Mfg. TE series centrifugal pump controlled by an ITT® PumpSmart inverter system that uses a DynaSonic® TFX Ultra flow meter for the feedback of the control system. The system is capable of maintaining a set flow rate within 1% and allows a range of Reynolds numbers from 500 to 20000 based on the width of the test section.

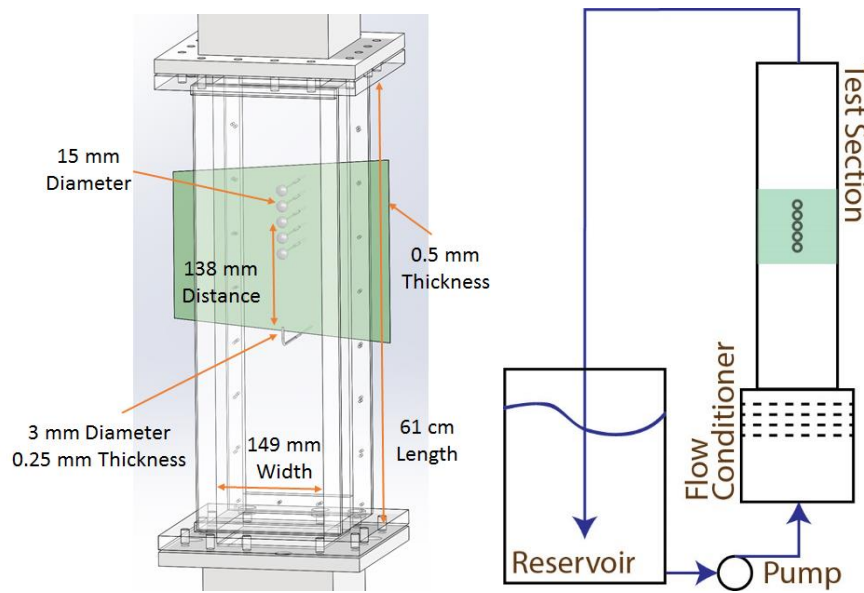


Figure 5.1 schematic of the experimental setup. Left: Details of the test section, Right: Flow loop.

Seeding for PIV is done with a density corresponding to 12 seed particles in a 16×16 pixel interrogation window using Spherical® hollow microspheres from Potters® industries with a mean diameter of 11  $\mu\text{m}$  and density of 1.10  $\text{g/cc}$  dissolved in the working liquid by means of the Kodak® Photo-Flo surfactant with a ratio of 1-200. Usage of the surfactant

eliminates presence of air bubbles in the system and minimizes deposition of seed particles on the wall and sphere surfaces and barely affects properties of the working liquid at the specified concentration. Deposition of either tiny air bubbles or seed particles on these surfaces can cause high intensity light scatter in near wall regions that can make successful interrogation impossible.

A PIV system from LaVision® Co. is used in this research that incorporates a NewWave Research® Gemini double pulsed Nd-YAG laser illuminating the middle plane of the test section, three double frame FlowMaster 3s cameras recording images of the corresponding flow field, and the DaVis 7.2 software acquisition and processing data fields. Macro lenses with 50 mm focal length set at an aperture of 5.6 f# were mounted on cameras that gives a sufficient depth of field for the measurements. Simple linear optics are used for maintaining a laser sheet thickness of 1 mm throughout the width of the channel and special care was taken in order to make sure that the plane of laser slices the center plane of the glass spheres. Calibration of the cameras using a pinhole model (Tsai, 1987) is usually considered accurate when the cameras are at a normal angle to the walls of the test section. But since the current setup is considered a 3 media environment, calibration was done using a 3<sup>rd</sup> order polynomial function (Soloff et al., 1999) in order to make it possible for accurately matching the images from all the cameras.

The common PIV criteria were taken into account in all experiments as described in (Raffel et al., 2007; Westerweel, 1997). The time difference between the two successive images was chosen so that the movement of particles was between 8-10 pixels. Out of plane motion of particles is expected to be negligible in all cases due to the symmetry of the flow. For each one of the cases presented here, 3333 pairs of images were taken. Multi pass cross

correlation (Scarano and Riethmuller, 2000) with interrogation windows of  $32 \times 32$  pixel size for the final pass with a 50% overlap was used for data processing. Particle image intensity is assumed to take on a Gaussian shape for sub-pixel interpolation (Nobach et al., 2005). In order to set the interrogation parameters, the correlation map was carefully studied at different interrogation window sizes. A post processing scheme that iteratively removes and replaces spurious vectors depending on correlation peak ratio and local velocity (Westerweel, 1994) was used to identify and remove false vectors. The effect of peak locking was investigated by plotting the probability density function of the resulting measured velocities in order to make sure there is no bias towards the integer values.

Results of a few cases were compared with the available literature for verification of the experimental facility using the experimental results of Goldstein et al. (Goldstein and Kreid, 1967). It should be noted that the experimental facility used here is relatively short in non-dimensional units ( $\frac{x}{HRe}$ ) and full length of the duct is in the developing region. The experiments were intentionally designed to be in this flow region in order to see the interaction of a flat velocity profile rather than a parabolic velocity profile with spherical particles. Figure 5.2 shows a comparison of velocity profile with that of Goldstein et al (Goldstein and Kreid, 1967) and also DNS results of Ramezani et al.

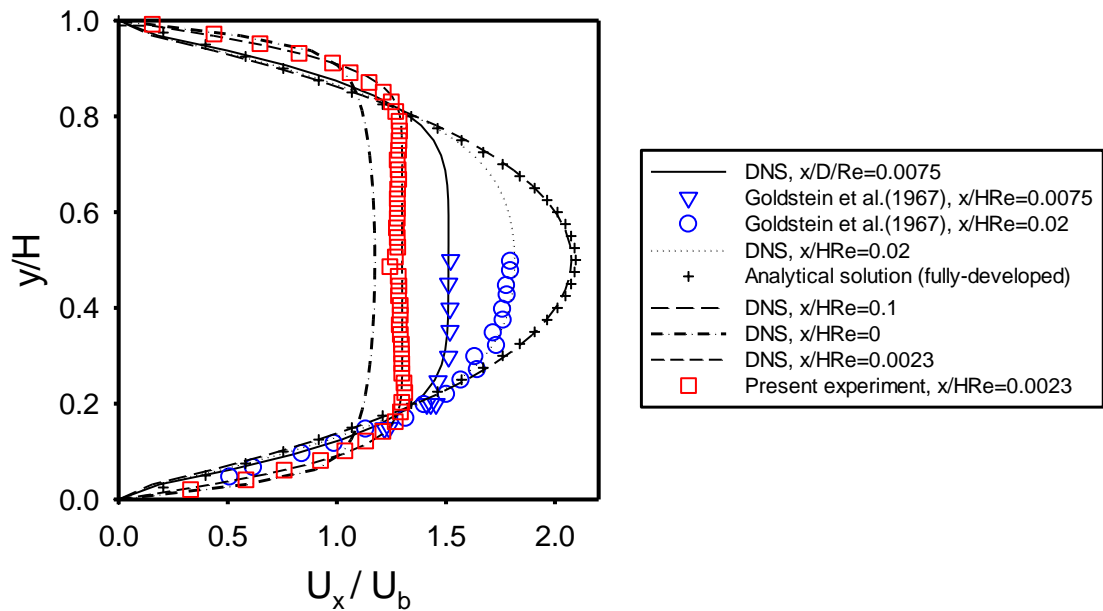


Figure 5.2 Comparison of velocity profile in developing duct flow.

#### 5.4 Results and Discussion

Current study provides field velocity data for a train of spherical particles arranged parallel to the flow direction on the centerline of the flow duct with different arrangements of three and five spheres and six different distance over diameter ratios. In addition to providing a large variety of test cases for validation of numerical results, it is possible to study the interaction of particles with flow as a function of particle distance and location in the train of particles. Such interactions between particles cause a dispersion in beds of particles (Koch and Brady, 1985) and are of particular importance in fundamental understanding of multiphase flows.

Results of the velocity field in this study are acquired using 3 cameras aligned in the axial direction, in order to expand the instantaneous field of view comparing to a single camera. The velocity field from each individual camera is calculated separately and then the resulting fields are combined using a linear interpolant in Matlab® software. Figure 5.3 shows a contour

plot of the results of the case of 5 spheres with a distance over diameter ratio of 2.19. Here, the color contours show the full field result and the line contours of different color show results from individual cameras. The figure shown here demonstrates the integrity of the interpolation scheme used for combining data fields. All experimental results are depicted as the average field of the 3333 frames recorded and the uncertainty of the values is believed to be under 2 percent per guidelines of PIV. Since the flow here is in laminar regime, time variations of flow field are negligible and instantaneous velocity fields look essentially similar.

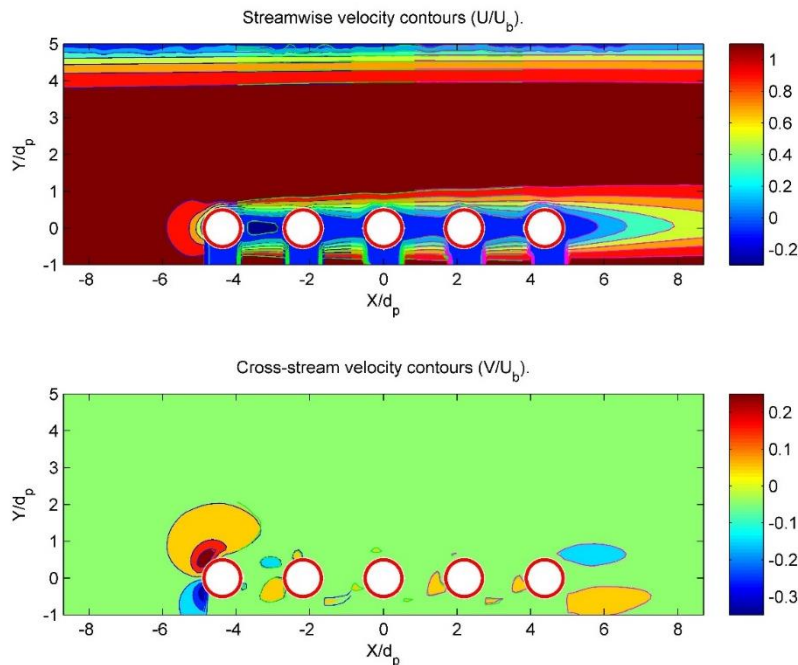


Figure 5.3 Comparison of the interpolated velocity field with individual data fields for  $Re_d=100$ . The lines represent the PR-DNS data and the contour plots represent the experimental data.

All the experimental data collection for the cases with spheres is done at a Reynolds number of 100 based on the diameter of the spherical particles, which corresponds to  $Re=1000$  based on the width of the duct. The flow inside the duct is in the developing region in order to have a flat velocity profile interact with the particle train. The flow is laminar and for a single sphere, a downstream conical vortex region is expected to be seen. Due to the symmetry of the

setup, laser illumination was provided from one side and only the illuminated half of the flow was recorded masking the spheres and the shadow area behind them from the field of view. A summary of all the cases studied here is given in Figure 5.4 below showing streamline plots of the flow.

Initial visual examination of Figure 5.4 suggests that depending on the distance over diameter ratio, spherical particles can already behave as a cluster, not allowing any significant flow in between them, for the  $d/D = 1.38$ . As the spheres get farther away from each other, for  $d/D = 1.73$  and  $d/D = 2.19$ , the vertical flow in the region between the spheres takes place which suggests that the flow can interact with spheres individually, hence that cannot be considered a particle cluster. A different variation of the flow appears for the spheres placed at  $d/D = 2.76$  which evidently suppresses the vertical flow due to the hindrance of neighboring spheres. However, at  $d/D = 4.38$ , the spheres are far enough that the downstream vortices appear again. It should be mentioned that in the near vicinity of the spheres, due to the very low velocities and optical interference from the refraction of the spheres, acquired velocity is expected to have lower accuracy. It is believed that the streamlines attaching to the spheres is not physical and is merely an artifact of the experimental method used here.

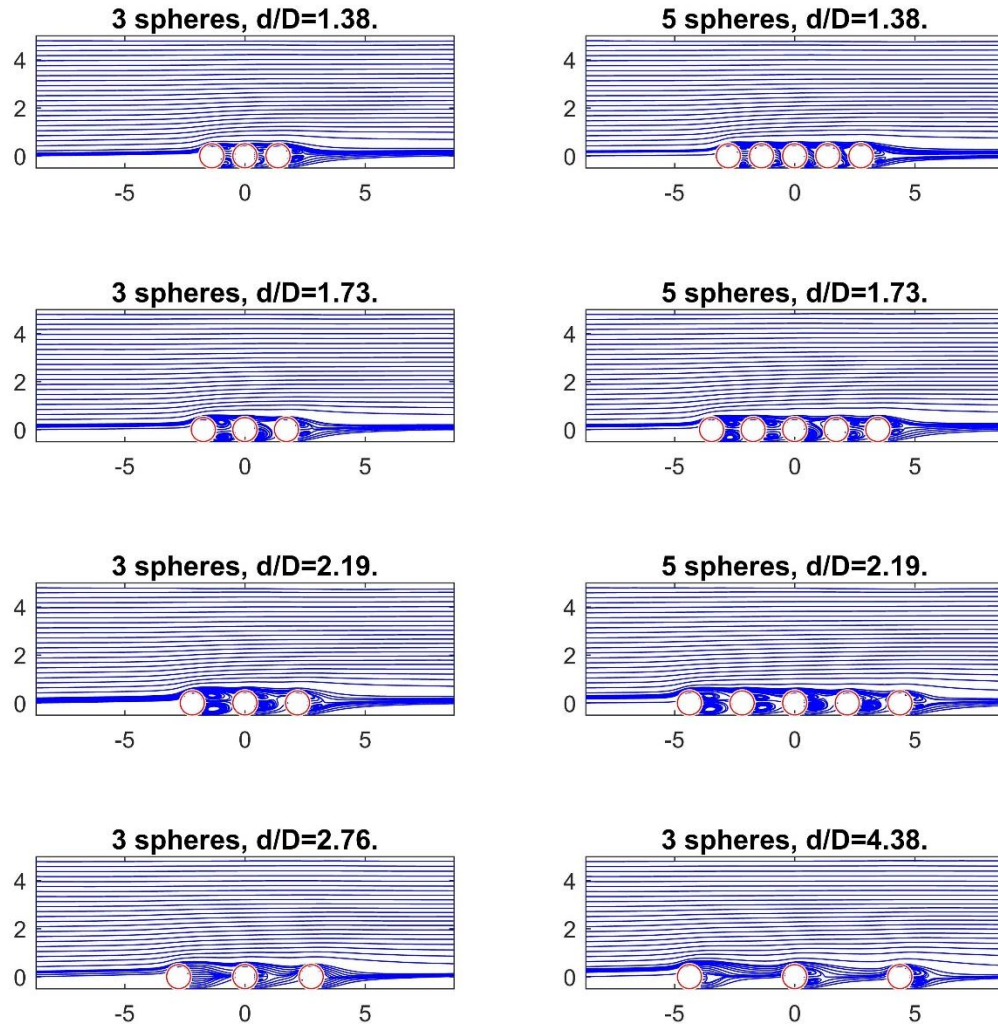


Figure 5.4 Experimental velocity field around a train of particles for  $Re_d=100$  at different arrangements.

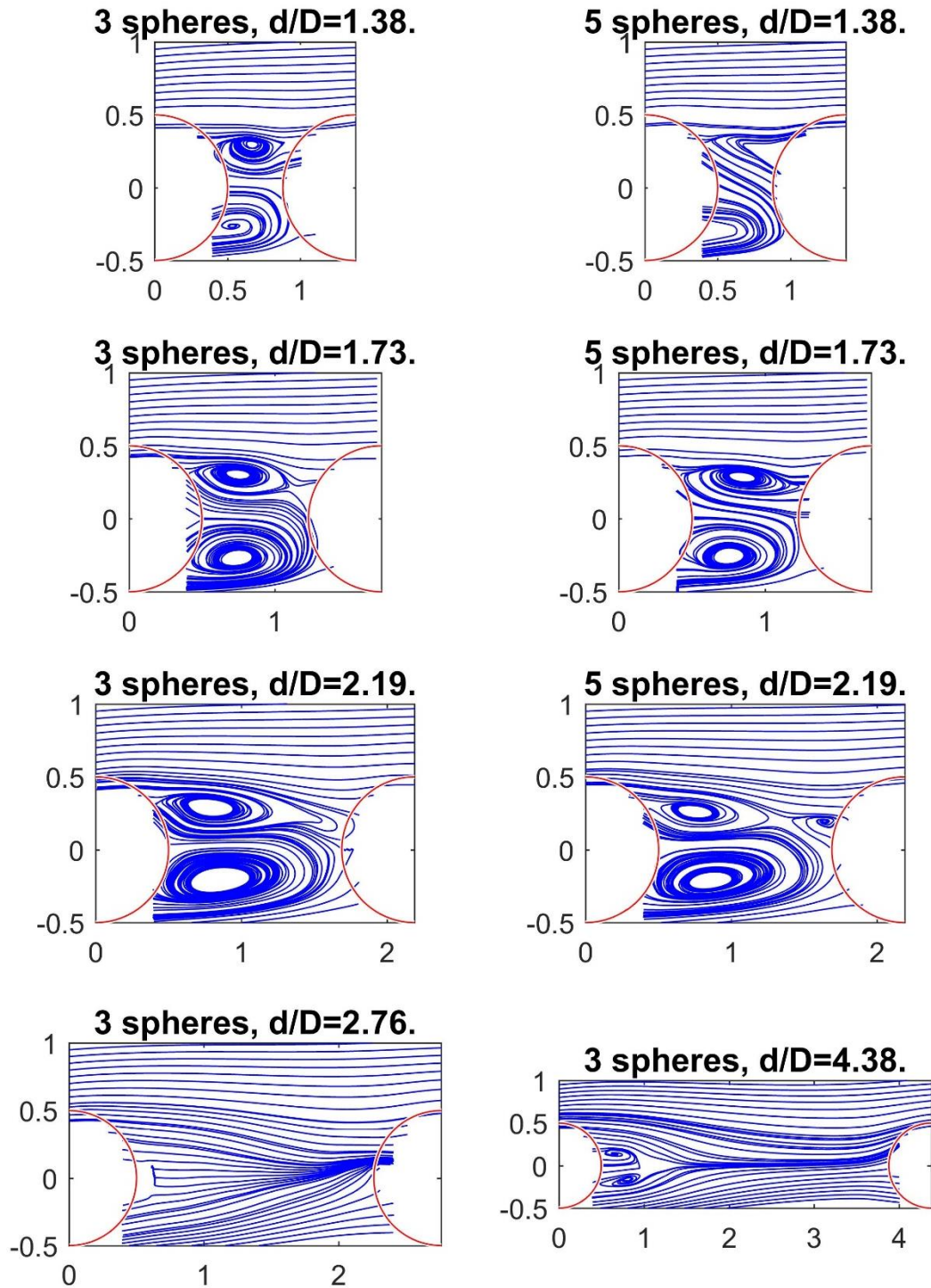


Figure 5.5 Spatio-temporal Average of flow between the spheres for different cases.

Some studies of multiphase flow systems are based on phasic averaging and this particular arrangement of spherical particles allows another way of representing data that emulates such averaging. Since the spherical particles are arranged in-line, it is possible to move the data of several spheres to the location of only one of them and calculate a spatial average of the already temporal averaged flow field between the two spheres. This is a spatio-temporal average that reveals the flow field based only the arrangement of particles and independent of their location in the arrangement. The spatio-temporal average of the experimental data is given in Figure 5.5 for all the studied cases showing very interesting structure of the corresponding flow field. These plots suggest that the interaction of flow with a train of particles depends merely on the distance over diameter ratio and the number of spherical particles in the arrangement make almost no effect on the flow. A double vortex appears in all cases except for the  $d/D = 2.76$  which is consistent with Figure 5.4 suggesting that certain arrangements of particles can hinder appearance of vertical structures.

In order to further investigate the differences seen in the previous figures, comparisons along a line are extracted and depicted separately in the following figures. Most of the similar plots from different cases compared here show very similar features, hence a few of the cases may be missing from the figures for such cases. Stream-wise velocity profiles on the centerline of the train between the first two spheres is shown in Figure 5.6 as a function of location non-dimensionalized by the distance between the spheres. This figure shows that the most packed arrangement with  $d/D = 1.38$  has virtually zero velocity between the spheres whereas the other cases show either positive or negative velocity depending on their formation. It can be seen that for the distance over diameter ratios of 1.73 and 2.19 the velocity is negative suggesting

that flow will pull the particle arrangement together to make it more packed whereas a positive velocity profile for the higher distance ratios will tend to spread the particles apart.

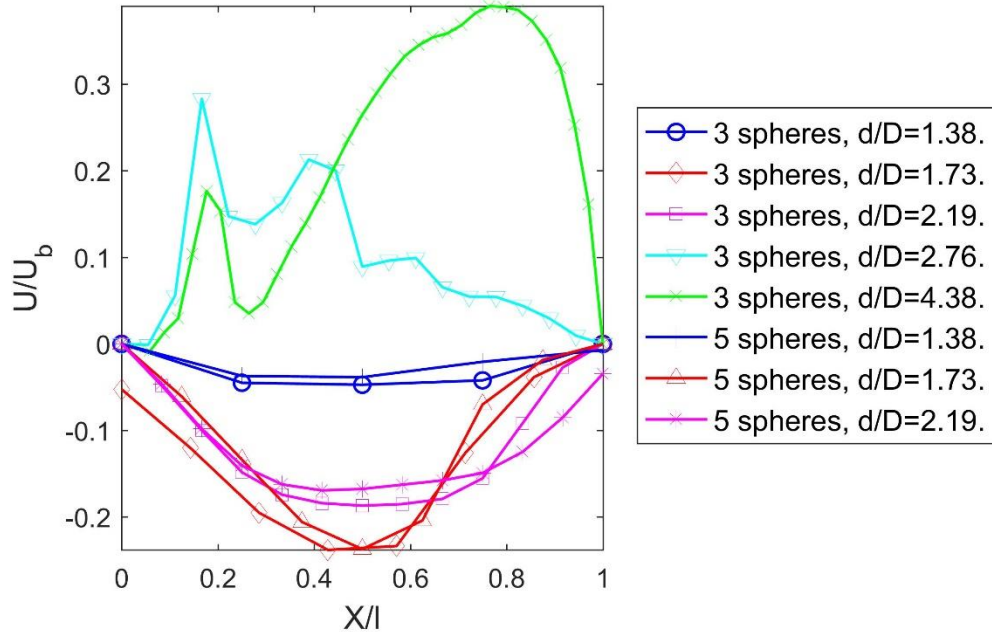


Figure 5.6 Stream-wise velocity profile on the centerline between the first and second spheres.

Development of the flow downstream the particle train is an important feature showing the impact of the particle arrangement on the flow. Figure 5.7 shows stream-wise velocity profiles on the centerline downstream the last sphere in different arrangements in comparison to the case of a single sphere. It is evident from this figure that all the cases of multiple spheres have very similar flow development downstream the train of particles which is quite different from the single sphere case. The length of the wake defined by the location of zero velocity too is the same for different cases with multiple spheres and that is shorter than the single sphere case.

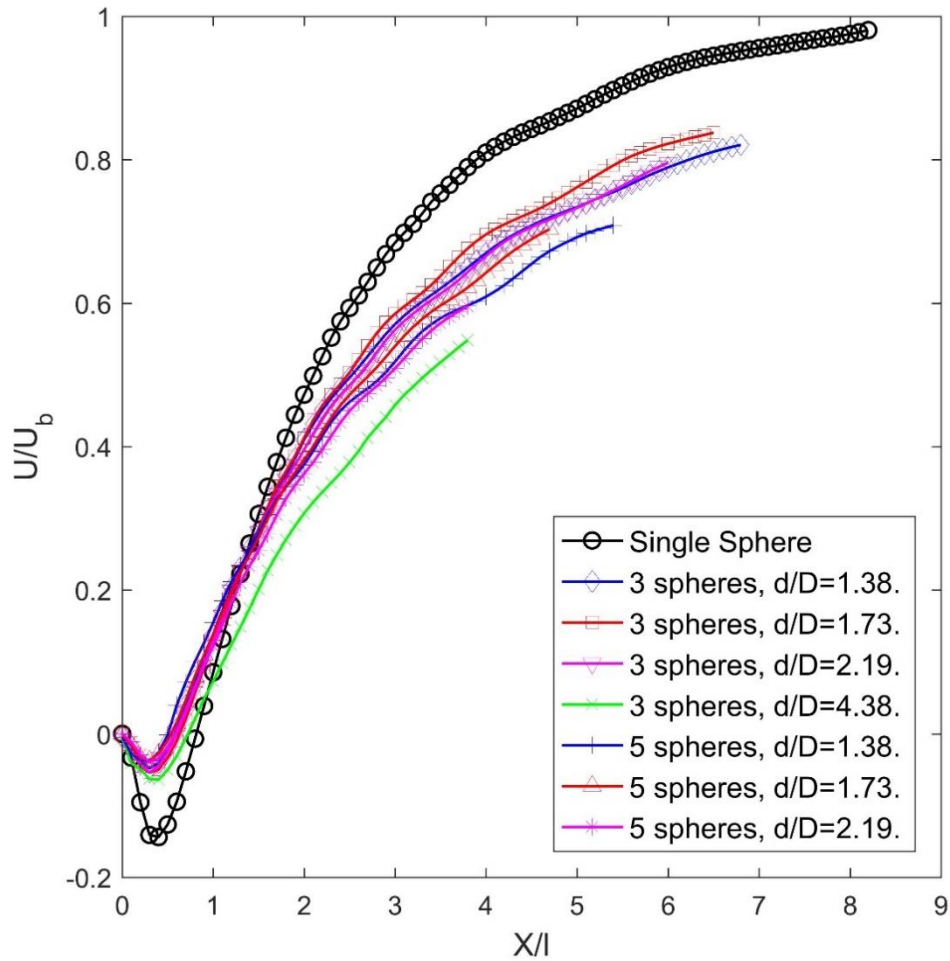


Figure 5.7 Stream-wise velocity profile on the centerline downstream the last sphere.

The interaction of flow with the most upstream sphere in the arrangement is quite different comparing to the downstream ones as shown in Figure 5.8. This figure shows the velocity profile along the centerline of the first, third, and fifth sphere in the arrangement. The first sphere causes a spike in the flow velocity in the near vicinity of the sphere and that effect is absent in rest of the spheres and their profiles look almost identical. Profiles of the other two spheres were omitted from this figure due to being very similar in order to keep the figure clear.

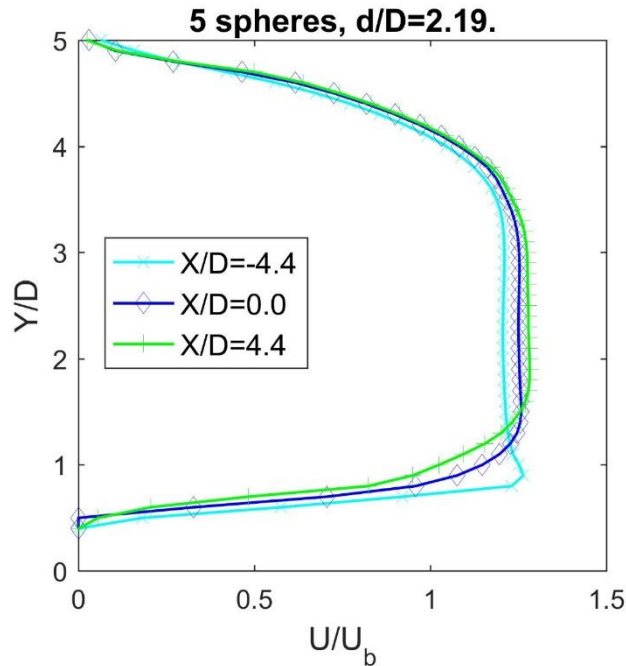


Figure 5.8 Stream-wise velocity profile on the centerline downstream the last sphere.

The profile of velocity in the middle of the spheres are given in Figure 5.9 for three nominal cases with three distance over diameter ratios. As was pointed out earlier, for the case with closes packing, the flow velocity is almost zero and is persistent for about the whole radius of the sphere. For the lower packing at  $d/D = 1.73$ , a low negative velocity is seen in between the spheres with the highest velocity occurring between the first and second sphere while the rest being almost identical. The case with the highest distance over diameter ratio also shows that the velocity is positive across the width of the duct.

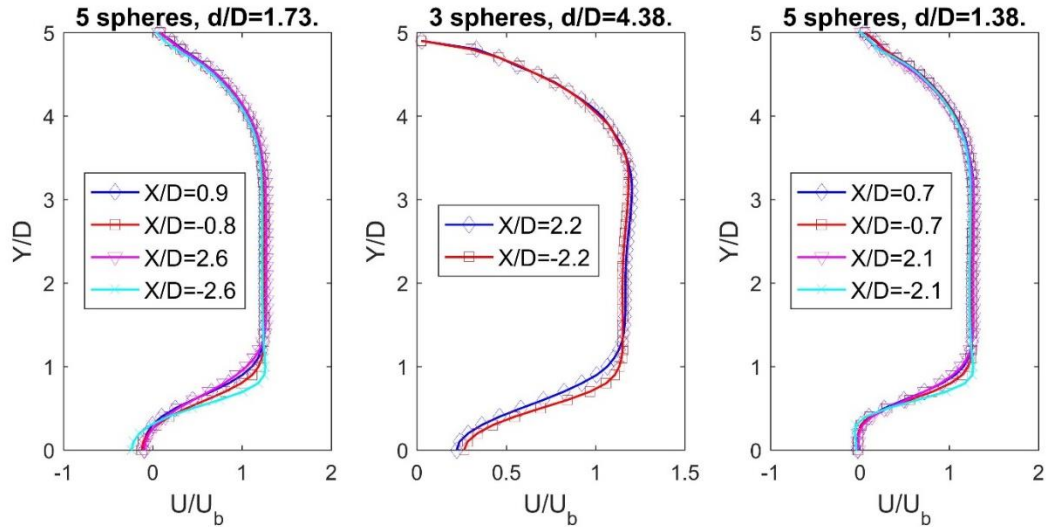


Figure 5.9 Stream-wise velocity profile on the centerline downstream the last sphere.

## 5.5 Conclusions

Experiments were performed with a train of 1, 3, or 5 spherical particles arranged inline on the centerline of a square duct at 5 different distance over diameter ratios in order to characterize the interaction of flow with a cluster of particles. Velocity field data was presented and studies showing that the behavior of flow is merely a function of the distance and almost independent of the number of spheres in the arrangement. The higher packed arrangement seems to not allow the flow between the spheres and act as a cluster whereas the lower packed arrangements allow the flow between them to interact with the particles and either pull them together or push them away depending on the distance over diameter ratio. The interaction of multiple spheres with flow was contrasted with the case of a single sphere. Within the arrangement, it was noted that the most upstream sphere causes quite different flow patterns in comparison to the rest of the arrangement.

## CHAPTER 6

DETAILED EXPERIMENTAL AND NUMERICAL INVESTIGATION OF  
HYDRODYNAMIC FLUID-PARTICLE INTERACTIONS USING VELOCITY FIELD  
COMPARISON OF A FIXED TRAIN OF SPHERICAL PARTICLES INSIDE A SQUARE  
DUCT

This chapter is a manuscript prepared for submission to Journal of Multiphase Flow. My contribution to this work is to perform the experimental measurements, data processing, and preparation of the manuscript. The numerical simulation is performed by Doctor Bo Sun under supervision of Professor Shankar Subramaniam.

## 6.1 Abstract

Experimental measurement and numerical simulation of flow inside a square duct around a train of five spherical particles at a Reynolds number of 100 is performed for two different particle separation distances of  $l/D_p$  of 1.38 and 2.19. The full geometry of the simulation was directly matched between the simulation and experiment and the velocity fields are compared in detail. The results from Particle-Resolved Direct Numerical Simulation (PR-DNS) were validated with the Particle Image Velocimetry (PIV) data with an average error of 7%. It was argued that validations using local flow measurement are potentially unreliable for simulation verification and field value comparisons are needed. In addition, conclusions are drawn about the interaction of flow with spherical particles in the arrangement depending on the distance over diameter ratio.

## 6.2 Introduction

A fundamental understanding of multiphase flow systems requires the study of the complex phenomena that occur between the particles, bubbles, or droplets that comprise the disperse phase and their interaction with the continuous phase. Of particular interest in fluid-solid two-phase systems are the effects of fluid phase hydrodynamics on the aggregation and dispersion of solid particles (Koch and Brady, 1985; Lim et al., 1995; Mehrabadi et al., 2015), the interactions of the solid phase such as elasticity and friction (Mehrabadi et al., 2016a), electrostatic charges and surface properties of particles (Royer et al., 2009), and effects of the shape of the solid phase particles (Siewert et al., 2014).

Two-phase fluid-solid flow is encountered in a variety of industrial applications (Dai and Grace, 2010; Wang et al., 2004). Perhaps the oldest industrial application is Fluid Catalytic Cracking (FCC). Other fluid-solid applications include the production of different monomers and polymers, Chemical Looping Combustion (CLC), pyrolysis of biomass, and gasification. The design and optimization of any laboratory scale prototype or industry scale plant often involves numerical simulations. These simulations are usually performed using two-fluid models or point-particle schemes. The use of the density-weighted average equations or the point-particle assumptions of these schemes bring about unknown source terms that are implemented through the use of closure models (Mehrabadi et al., 2016b; Tenneti et al., 2011). A successful numerical simulation will typically be used to predict operating parameters such as flow rate, pressure drop, bed height, particle carry-over, clustering or preferential accumulation, fluid entrainment, and particle attrition.

Most of the industrial applications of such flow systems involve heat or mass transfer between the two phases and possibly chemical reactions in either or both phases (Chen et al.,

1997; Sun et al., 2016, 2015; Tenneti et al., 2013). Attempts have been made in the past to study such phenomena in terms of dispersion and diffusion of concentration (Koch and Brady, 1987, 1985). Most of these studies consider porous media or a fixed or fluidized bed (Tang et al., 2016; Wang et al., 2004). Clustering of particles is also of particular interest in such flow systems (Capecelatro et al., 2014). Previous studies have investigated fluid flow around different arrangements of spherical solid particles based on drag force measurement (Liang et al., 1996; Zhu et al., 1994), numerical investigation of flow around multiple spheres (Jadoon et al., 2010; Maheshwari et al., 2006; Pahl et al., 2009, 2007; Tsuji et al., 2003), experimental field measurement of similar geometries (Chen and Wu, 2000; Ozgoren, 2013; Pinar et al., 2013; Tsuji et al., 1982). A fundamental understanding of the basic hydrodynamics in such flow systems is crucial for correctly predicting other aspects of these flows. Providing appropriate closure models for a successful simulation can possibly be done using experiments and analytical modeling; however, the complex nature of these flows makes such an approach challenging. Specifically, experimental investigation of such flows is inherently difficult due to the presence of the particles that inhibits access and hinders data collection from inside the bed. Most of the small scale phenomena occurring inside the flow is not directly traceable and only local and average readings can be made. In contrast, Direct Numerical Simulation (DNS) of such flows can provide very detailed information that both increases knowledge of the complex phenomena and if simulated appropriately, can provide the necessary data to develop and validate closure models (Tang et al., 2016; Tenneti and Subramaniam, 2014; Tenneti et al., 2011). The Particle Resolved DNS (PR-DNS) simulation introduced in the current paper is capable of providing numerical correlations for drag coefficient, Nusselt number, and

Schmidt number along with closure models for pseudo turbulent terms in the Favre-averaged continuum equations.

The current study focuses on investigating the case of a train of successive spherical solid particles inside a liquid flowing medium confined in a square duct both experimentally using particle image velocimetry (PIV) and numerically using PR-DNS. Simultaneous experimental and numerical investigation of this geometry allows a detailed validation of the simulation method based on a direct velocity field comparison. This is an important step towards providing reliable correlations based on the PR-DNS results.

### 6.3 Approach

#### 6.3.1 Experimental Setup and Procedure

The experimental apparatus used in this study is shown in Figure 6.1. The test section consists of a square cross section water tunnel with 149 mm width and 610 mm length made of clear acrylic. In order to get a uniform inlet flow to the test section, several layers of perforated stainless steel sheets with varying arrangements are installed in the upstream flow conditioner that provides a uniform flow of deionized water into the test section. Fused silica spheres with diameters of 15 mm are placed inside the channel and held in place by means of 2 mm diameter stings attached to the back wall of the section at stationary arrangements. This wall of the section is removable and allows for varying the arrangement of the spheres from one experiment to the next.

The flow loop outside of the test section consists of 38 mm (1½") diameter PVC piping. Flow of De-Ionized water is maintained circulating through the flow facility by means of a March® Mfg. TE series centrifugal pump controlled by an ITT® PumpSmart inverter system that uses a DynaSonics® TFX Ultra flow meter for the feedback of the control system. The

system is capable of maintaining a set flow rate within 1% and allows for a range of Reynolds numbers from 500 to 20000 based on the width of the test section.

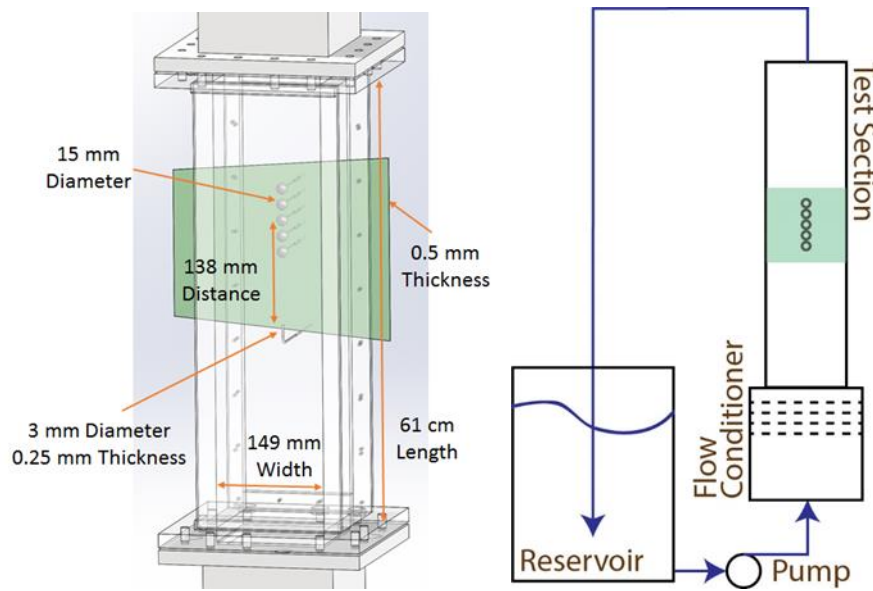


Figure 6.1 Schematic of the experimental setup. Left: Details of the test section, Right: Flow loop.

The PIV seed particles were Spherical® hollow microspheres from Potters® industries with a mean diameter of 11  $\mu\text{m}$  and an almost neutrally Buoyant density of 1.10 g/cc dissolved in the working liquid. Kodak® Photo-Flo surfactant solution was added to the water at a volume ratio of 0.05%. The surfactant eliminated the presence of air bubbles in the system and reduced the deposition of seed particles on the test section walls and sphere surfaces while negligibly affecting the properties of the working fluid at the specified concentration. The seeding density corresponded to a mean of 12 seed particles within each 16 $\times$ 16 pixel PIV interrogation window.

The PIV system from LaVision® Co. used in this research that incorporated a NewWave Research® Gemini double pulsed Nd-YAG laser illuminating the middle plane of the test section, three double frame FlowMaster 3s cameras recording images of the

corresponding flow field, and DaVis 7.2 software for system synchronization and processing of velocity fields. Macro lenses with 50 mm focal length set at an aperture of 5.6 f# were mounted on cameras. The illuminating laser sheet had a thickness of 1 mm throughout the width of the channel and was carefully aligned to dissect the center plane of the glass spheres. Calibration of the cameras using a pinhole model (Tsai, 1987) is usually considered accurate when the cameras are at a normal angle to the walls of the test section. However, since the current setup actually consists of a 3 media environment (plexiglass test section, water as the working fluid, and air outside of the test section), calibration was performed using a 3rd order polynomial function (Soloff et al., 1999) in order to make it possible for accurately matching the images from all the cameras.

The PIV system operating parameters in all experiments were determined according to guidelines described Westerweel (Westerweel, 1997) and Raffel et al. (Raffel et al., 2007). The time separation between two successive images was chosen so that the movement of particles was between 8-10 pixels. Out of plane motion of particles is expected to be negligible in all cases due to the symmetry of the flow. For each one of the cases presented here, 3333 pairs of images were collected. Multi-pass cross correlation with interrogation windows of 32×32 pixel size for the final pass with a 50% overlap was used for data processing (Scarano and Riethmuller, 2000). Particle image intensity is assumed to take on a Gaussian shape for sub-pixel interpolation (Nobach et al., 2005). In order to set the interrogation parameters, the correlation map was carefully studied at different interrogation window sizes. A post processing scheme that iteratively removes and replaces spurious vectors depending on correlation peak ratio and local velocity was used to identify and remove false vectors (Westerweel, 1994). The effect of peak locking was investigated by plotting the probability

density function of the resulting measured velocities in order to make sure there is no bias towards the integer values.

### 6.3.2 Numerical Simulation

A finite-difference (FD) PR-DNS formulation has been developed to simulate the wall-bounded particle-laden flow and heat transfer. The numerical results obtained from simulations of the same geometries as the experiments are used for comparison with the experimental data from the experimental test section. The FD formulation is briefly described and validated in two test cases in the following sections.

#### 6.3.2.1 Governing Equations

The mass, momentum conservation, and scalar equations to solve constant density wall-bounded flow with heat transfer from particles are the same as those in the formulation of Tenneti et al. (Tenneti and Subramaniam, 2014; Tenneti et al., 2010) as follows:

$$\frac{\partial u_i}{\partial x_i} = 0 \quad \text{on } \Omega \quad (6.1)$$

$$\frac{\partial u_i}{\partial t} + S_i = -\frac{1}{\rho_f} g_i + \nu_f \frac{\partial^2 u_i}{\partial x_j^2} + I_s f_{u,i} \quad \text{on } \Omega \quad (6.2)$$

$$\frac{\partial \phi}{\partial t} + S_\phi = \alpha_f \frac{\partial^2 \phi}{\partial x_j^2} + I_s f_\phi \quad \text{on } \Omega \quad (6.3)$$

where  $\Omega$  is the entire domain,  $\nu_f$  is the kinematic viscosity in the fluid phase,  $\alpha_f$  is the thermal diffusivity in the fluid phase,  $g_i = \partial p / \partial x_i$  is the pressure gradient,  $S_i = \partial(u_i u_j) / \partial x_j$  and  $S_\phi = \partial(u_j \phi) / \partial x_j$  are the convective terms in the momentum conservation and scalar equations,  $f_{u,i}$  and  $f_\phi$  are the additional immersed boundary (IB) direct forcing

terms that are nonzero only in the solid phase. The IB direct forcing accounts for the presence of the solid particles in the domain by ensuring that the no-slip and isothermal boundary conditions are satisfied on each particle surface. Various boundary conditions such as Neumann boundary condition can be implemented easily with these equations.

### 6.3.2.2 Numerical Approach

The FD formulation allows for implementation of various boundary conditions such as walls and inflow/outflow to simulate the same setup as the experimental test section. With appropriate boundary conditions the governing equations in Eqs. (6.1-6.3) are discretized on a uniform Cartesian grid and solved at each time step. The spatial discretization of these equations is performed using a second-order finite-difference scheme on a fully-staggered grid. On a fully-staggered grid, the velocity or momentum variables are located at the cell faces while the scalar variables such as pressure and temperature are stored at cell centers. The time discretization of the momentum equation is performed following Tenneti et al. (Sun et al., 2015).

$$\frac{u_i^{n+1} - u_i^n}{\Delta t} = -\left(\frac{3}{2} S_i^n - \frac{1}{2} S_i^{n-1}\right) - \frac{1}{\rho_f} \nabla q^{n+1} + \frac{v_f}{2} \nabla^2 (u_i^n + u_i^{n+1}) + f_{u,i}^{n+1} \quad (6.4)$$

where the IB forcing is

$$f_{u,i}^{n+1} = \frac{u_i^d - u_i^n}{\Delta t} + S_i^n + \frac{1}{\rho_f} g_i^n - v_f \frac{\partial^2 u_i^n}{\partial x_j^2} \quad (6.5)$$

For the temporal discretization of the momentum equation, the Adams-Bashforth scheme is used for the convective terms, and the Crank-Nicolson scheme is used for the viscous terms. In order to solve the discretized momentum equation (Eq. 6.4), a two-step fractional step method is used. The first step to obtain the intermediate velocity field  $u^*$  is computed from

$$\frac{u_i^* - u_i^n}{\Delta t} = -\left(\frac{3}{2}S_i^n - \frac{1}{2}S_i^{n-1}\right) - \frac{1}{\rho_f}g_i^n + \frac{v_f}{2}\nabla^2(u_i^n + u_i^*) + f_{u,i}^{n+1} \quad (6.6)$$

Since the velocity in the  $n+1$ th step  $u^{n+1}$  is required to satisfy the divergence-free condition, the second step is to solve the Poisson equation (Eq. 6.7) to correct the velocity field based on the intermediate velocity field as shown in Eq. 8.

$$\frac{\Delta t}{\rho} \nabla^2 \varphi = \nabla \cdot u_i^* \quad (6.7)$$

$$u_i^{n+1} = u_i^* - \frac{\Delta t}{\rho} \nabla \varphi \quad (6.8)$$

The pressure at the  $n+1$ th step is also updated based on the pressure at the pervious step, as:

$$p^{n+1} = p^n + \varphi - \frac{v_f \Delta t}{2} \nabla^2 \varphi \quad (6.9)$$

The discretized scalar equation in Eq. 3 is solved using the same temporal discretization for the solution of the momentum equation in Eq. 4:

$$\frac{\phi^{n+1} - \phi^n}{\Delta t} = -\left(\frac{3}{2}S_\phi^n - \frac{1}{2}S_\phi^{n-1}\right) + \frac{\alpha_f}{2} \nabla^2 (\phi^n + \phi^{n+1}) + f_\phi^{n+1}, \quad (6.10)$$

where the IB direct forcing term  $f_\phi$  is

$$f_\phi^{n+1} = \frac{\phi^d - \phi^n}{\Delta t} + S_\phi^n - \alpha_f \frac{\partial^2 \phi^n}{\partial x_j^2} \quad (6.11)$$

The spatial discretization of the convection and diffusion terms in the discretized scalar equation (Eq. 6.10) use the same schemes as those in the momentum equation.

### 6.3.2.3 Numerical convergence and accuracy of FD formulation

To validate the accuracy and convergence of the FD formulation, a suite of simulations was conducted. The first test case was thermal fully-developed flow in a square duct, and the second case was a flow past a fixed sphere in an open domain.

In order to investigate the accuracy of the FD formulation, simulations were performed for fully-developed flow in a square duct. The numerical results from the FD formulation were then compared with the analytical solution for fully-developed flow in a square duct. The analytical solution for the velocity is

$$\frac{u}{u_m} = \frac{48}{\pi^3} \left[ \sum_{n=1,3,\dots}^{\infty} \frac{1}{n^3} (-1)^{(n-1)/2} \left[ 1 - \frac{\cosh(n\pi y / 2a)}{\cosh(n\pi b / 2a)} \right] \cos\left(\frac{n\pi z}{2a}\right) \right] / \left[ 1 - \frac{192}{\pi^2} \left(\frac{a}{b}\right) \sum_{n=1,3,\dots}^{\infty} \frac{1}{n^5} \tanh\left(\frac{n\pi b}{2a}\right) \right] \quad (6.12)$$

where  $2a$  and  $2b$  are the height and width of the cross-section of a rectangle duct, respectively, and  $u_m$  is the mean velocity in the streamwise direction. In the case of a square duct,  $a$  is set equal to be  $b$ . Figure 6.2 shows the error in the velocity profiles between numerical results and the analytical solution along the central line in the cross section of the duct. It was found that the error in the velocity profile obtained using the FD formulation was below 0.3%. The error in the entire domain of the duct was also checked (see Figure 6.3) using the  $L_2$ -norm of the error. The  $L_2$ -norm of the error is defined as

$$\xi_{\|u\|_2} = \left[ \frac{1}{N_y N_z} \sum_{j=1}^{N_y} \sum_{k=1}^{N_z} \left( \frac{u_{j,k}^{num} - u_{j,k}^{ana}}{u_m^{ana}} \right)^2 \right]^{1/2} \quad (6.13)$$

where  $N_y$  and  $N_z$  is the number of grid nodes in y and z direction. In Figure 6.3 the spatial accuracy of the FD formulation is observed to be second-order in the  $L_2$  norm.

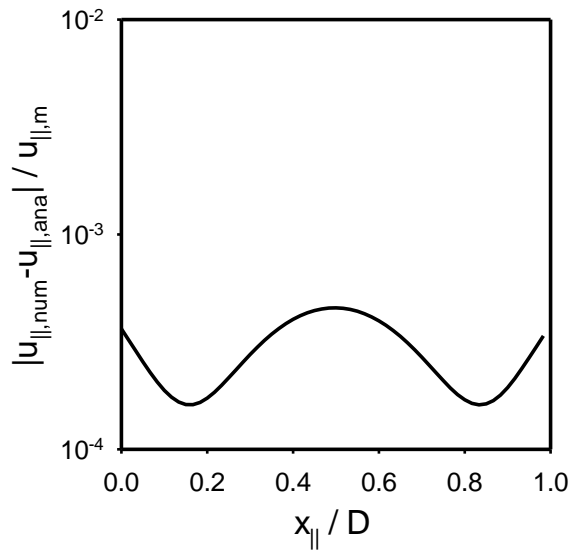


Figure 6.2 Accuracy of numerical results ( $D_m=D/dx=90$ ) and analytical solution along the central line in the cross section of the duct.

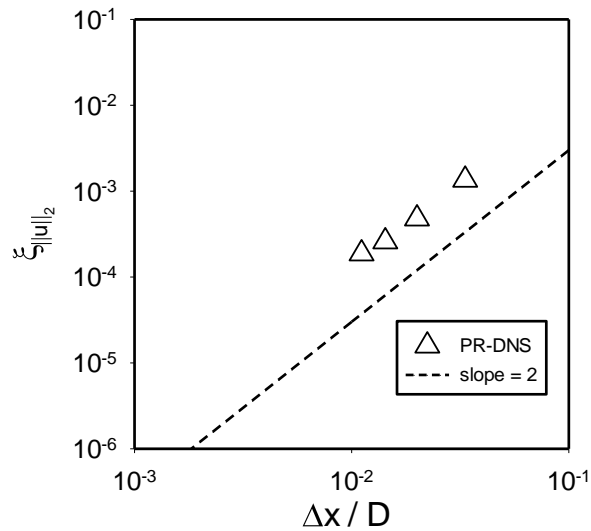


Figure 6.3 Convergence of FD formulations in the duct flow using the  $L_2$ -norm of the error.

The other test case was flow past a single spherical particle in an open field. This is a common benchmark accuracy test for any numerical simulation approach to gas-solid flow. With the parallel FD solver, it is possible to simulate a large domain with a single spherical particle in order to avoid the effect of boundary conditions on the particle drag. Steady flow

past a sphere with a uniform velocity  $U_{in}$  in the inlet was simulated in a computational domain of dimensions  $20D \times 20D \times 20D$ , where  $D$  is the diameter of the sphere. Except for the inlet boundary, Neumann boundary conditions are imposed on all the domain boundaries. No-slip and no-penetration boundary conditions are imposed at the particle surface. The Reynolds number was defined as  $Re = \rho_f D U_{in} / \mu_f$  and was varied from 20 to 140. The sphere was represented using 30 grid points along the sphere diameter.

Figure 6.4 shows the drag coefficient for flow past a sphere in the large domain. The drag coefficient is defined as  $C_D = 2F_d / \rho_f U_{in}^2 A$ , where  $F_d$  is the drag force, and  $A$  is the frontal area of the sphere. The drag coefficient using FD PR-DNS shows excellent agreement with existing numerical data and experimental data. The results indicate that parallel FD has the capability to capture flow physics accurately.

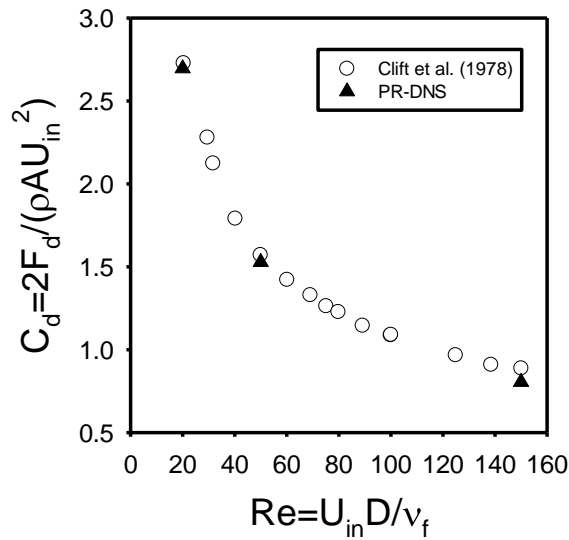


Figure 6.4 Drag coefficient ( $C_D$ ) for flow past a fixed sphere at various Reynolds numbers. The circles represent the numerical results from standard drag coefficient from Clift et al. (Clift et al., 2005).

#### 6.3.2.4 Validation

Comparisons between model and experiment were made for a pure duct flow by running different experimental and numerical cases at various Reynolds numbers. These results were compared with the experimental results of Goldstein et al. (Goldstein and Kreid, 1967) for verification of the experimental facility design and the numerical method used in this study. The results from two numerical simulations and three experimental cases are presented in Figure 6.5 and show the dimensionless centerline velocity versus the dimensionless axial location in the duct. Both the simulations and experiments match the available literature very well for the different cases. It should be noted that the experimental facility used here is relatively short in dimensionless units ( $\frac{x}{HRe}$ ), and thus the entire length of the duct is in the developing region as shown in Figure 6.5. The experiments were intentionally designed to be in this flow region in order to observe the interaction of a flat velocity profile rather than a parabolic velocity profile with spherical particles. Figure 6.6 shows a comparison of velocity profiles obtained from the numerical simulations to the corresponding data from available literature and also the current experiments.

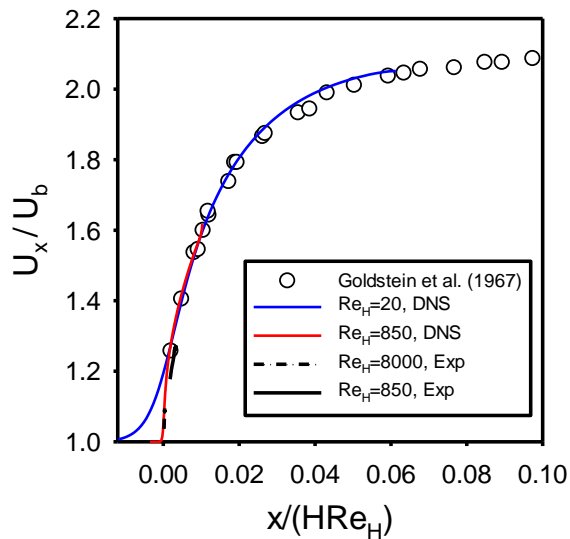


Figure 6.5 Comparison of centerline velocity development in duct flow.

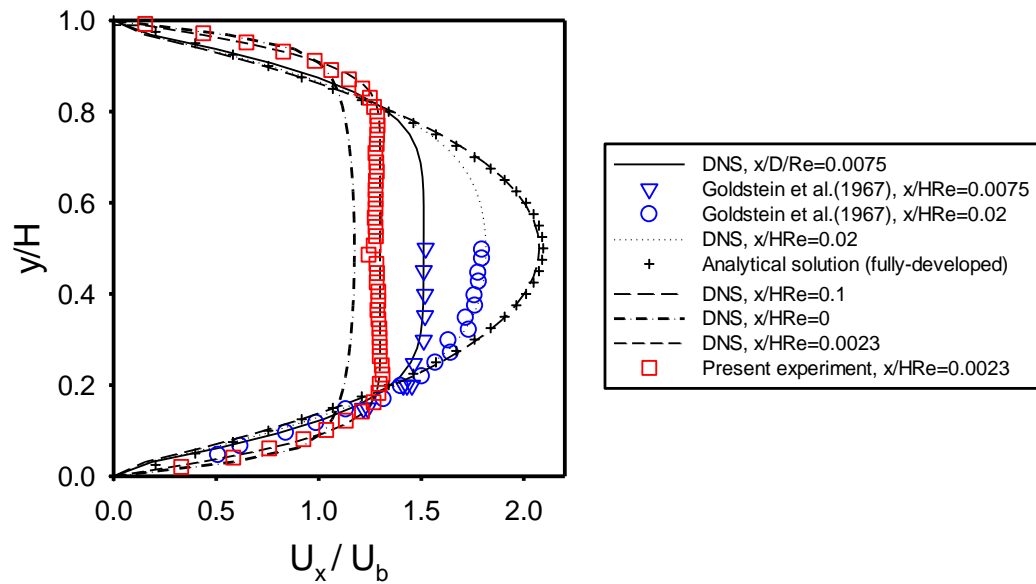


Figure 6.6 Comparison of velocity profile in developing duct flow.

The case of flow around a single sphere is very well known, and many aspects of this flow at different conditions have been previously studied. A second test case in the current investigation is flow around a single sphere in a duct. For this purpose, the geometry of the experiment was matched in the simulation and velocity field results are compared as shown in

Figure 6.7 for a single sphere in a flow at  $Re_d = 85$  based on the diameter of the sphere. This figure compares contour plots of individual components of the velocity vector for the simulation (shown in color) with the experiment (shown as lines). Contour levels of the overlaid experimental and numerical results match each other, which means that the lines are expected to overlap with the boundary of the colored contours. It can be seen that the velocities match nearly perfectly, and the only discrepancy is noticed across the sphere going towards the higher velocity region in between the sphere and the wall of the duct. The length of the wake for a sphere in free flow is expected to be  $L_w/D_p = 0.9$  (Taneda, 1956). Current results for the sphere confined within the duct shows a longer wake due to the containment inside a duct although the width of the wake is not affected. The simulation yields  $L_w/D_p = 1.20$ , and the experiment yields  $L_w/D_p = 1.25$  for the length of the wake.

In the experiments, the field of view is limited by the camera sensor size and is focused on the area around the sphere in order to provide a high resolution of velocity vectors relative to the sphere diameter. This results in 30 vectors per sphere diameter ratio in the experiments compared to a 25 grid point per sphere diameter resolution in the PR-DNS results. Hence, it is believed that both methods resolve the near-sphere boundary very well and allow a detailed comparison of the two methods. This high resolution for the experiments also helps to avoid any complication with resolving the near zero velocity in the vortex region downstream the sphere due to the limited dynamic range of PIV.

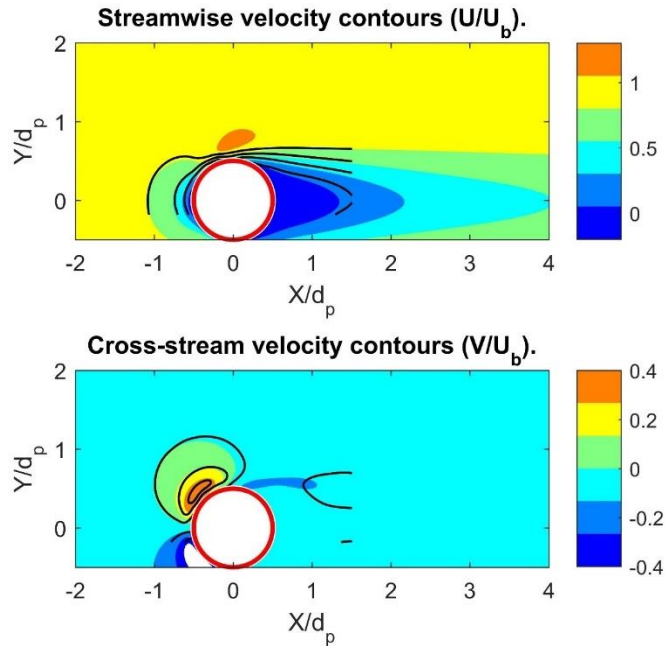


Figure 6.7 Comparison of the single sphere case at  $Re_d=85$ . The line contours represent the experimental data and the color contours represent the numerical PR-DNS data.

Other comparisons can be extracted from the velocity field data of Figure 6.7 that provide a clearer verification of the simulation results. Figure 6.8 and Figure 6.9 show comparisons of the axial velocity profile at different axial and transverse locations, respectively. Both figures show the experimental data using markers and the corresponding numerical results are shown as lines. It can be seen that the experimental and numerical results follow each other very closely in both the figures with about a 6 percent average difference. The development of the wake downstream the sphere can be seen in Figure 6.9, which shows the length of the wake is predicted within the margin of error of the experiment.

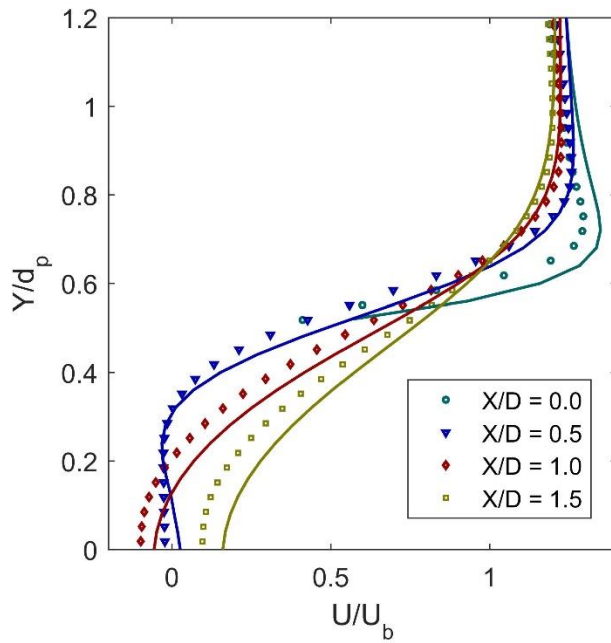


Figure 6.8 Comparison of axial velocity profile along the axial lines for a sphere at  $Re_d=85$ . The lines represent the PR-DNS data and the symbols represent the experimental data.

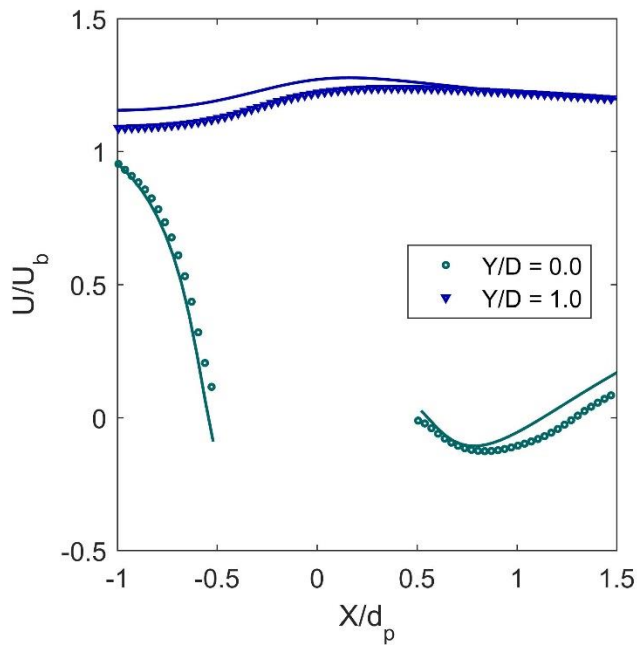


Figure 6.9 Comparison of axial velocity profile along the transverse lines for one sphere at  $Re_d=85$ . The lines represent the PR-DNS data and the symbols represent the experimental data.

It is worth mentioning that the velocity field is expected to be symmetric and hence, for all cases except for the pure duct flow, data collection is only focused on one half of the field. The symmetry of the flow field can be easily seen in Figure 6.6.

#### 6.4 Results and Discussion

The geometry that was chosen for comparison in the current study is a train of five spherical particles arranged parallel to the flow direction on the centerline of the flow duct. Using the two different sphere separation distance over diameter ratios, it is possible to study the effect of the particle wake on the downstream particles. Such interactions between particles cause a dispersion in beds of particles (Ham and Homsy, 1988; Koch and Brady, 1985) and are of particular importance in fundamental understanding of multiphase flows.

The experimental data collection for the cases with trains of spheres was performed at a Reynolds number of  $Re_d = 100$  based on the diameter of the spherical particles, corresponding to  $Re = 1000$  based on the width of the duct. Recall that the flow inside the duct is in the developing region in order to have a flat velocity profile interact with the particle train. The flow is laminar, and for a single sphere, a downstream conical vortex region is expected to be observed. Arrangements of a single particle and a train of 5 spherical particles with corresponding distance to diameter ratios of  $l/D_p = 1.38$  and  $2.19$  were investigated. Velocity vector fields from experiments are presented in Figure 6.10 showing streamline field for both of the five-particle cases investigated. It should be noted that the laser illumination for the velocity vector fields shown in this figure is from the top, causing a shadow area below the spheres. It is not possible to acquire velocity vectors in those areas and hence, they are simply masked out without causing any issues with the results due to the symmetry of the flow field. The locations of the spheres are also shown in the PIV velocity vector fields.

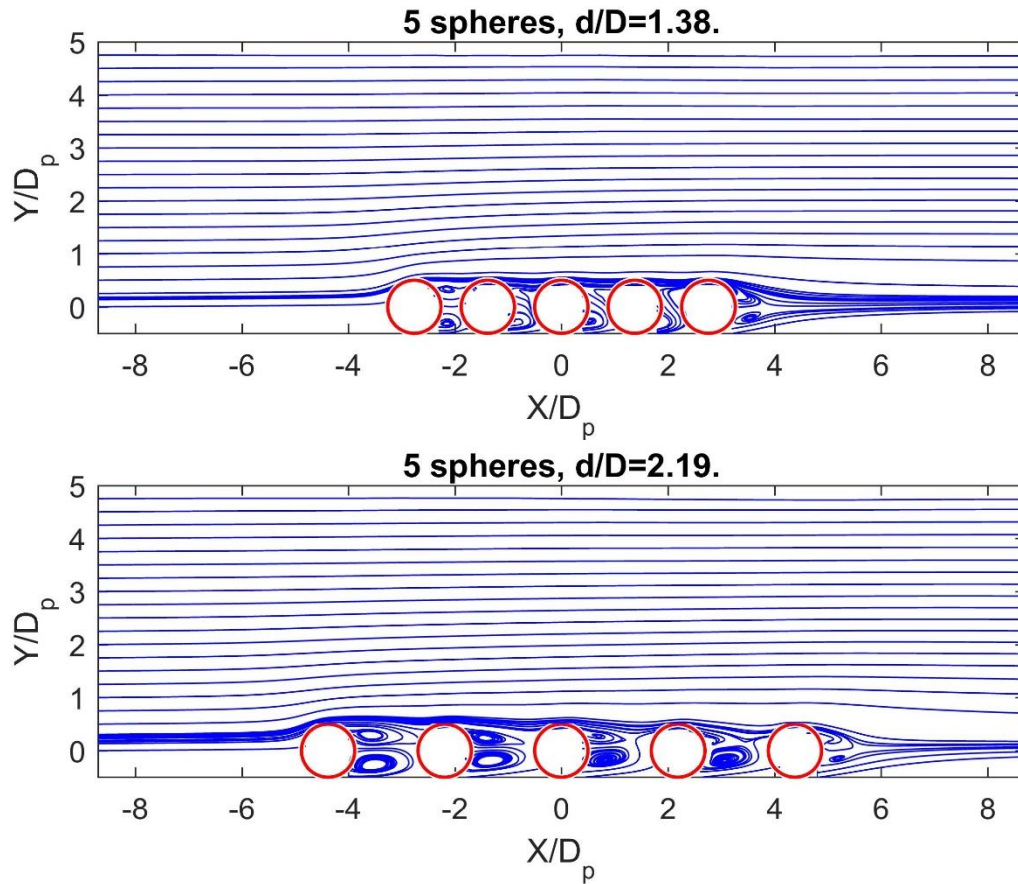


Figure 6.10 Experimental velocity field around a train of 5 particles overlaid on contour plots of velocity magnitude for  $Re_d=100$ . Top:  $l/D_p = 1.38$ , Bottom:  $l/D_p = 2.19$ .

The experimentally measured velocity field in this study are acquired using 3 cameras aligned along the axial direction, in order to expand the instantaneous field of view compared to using a single camera. The velocity field from each individual camera is calculated separately, and then the resulting fields are combined using a linear interpolant in Matlab® software. Figure 6.11 shows a contour plot of the individual velocity components for the case of 5 spheres with a distance over diameter ratio of 2.19. Here, the color contours show the interpolated complete field result and the line contours of different color show results from the individual cameras. These results demonstrate the integrity of the interpolation scheme used for combining data fields.

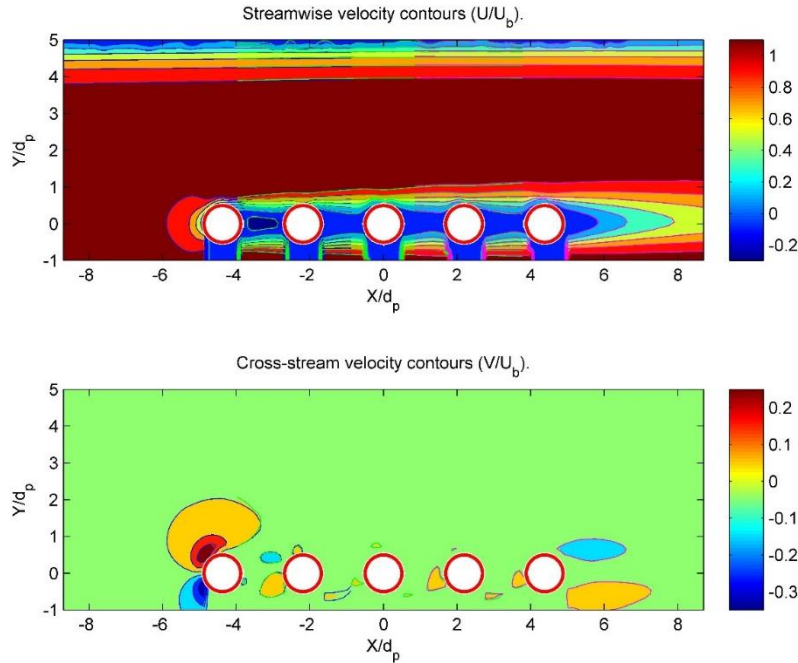


Figure 6.11 Contour plot of velocity comparing the interpolated velocity field with that of individual cameras. Top: Streamwise velocity, Bottom: Cross-stream velocity.

Numerical simulations were performed for the full test section with the same geometry as the experimental test section, and a representation of the resulting flow field is given in Figure 6.12 using 3D velocity streamlines. Usually a comparison between the simulation and experiment is done by simplifying the geometry and neglecting the effects of walls (Maheshwari et al., 2006). In contrast, this study shows a detailed comparison of the velocity field in the full duct between the experiment and simulation. It is worth noting that even though validation of a numerical model is possible using bulk quantities such as drag force or pressure drop comparison (Hicks, 1970; Wang et al., 2004), the exerted force on an object in flow is only a measure of velocity in the immediate vicinity of that object. Collecting detailed velocity field data, in contrast to local force measurement, allows for further extending the reach of verification tools into the fluid domain and extracting more information for comparison.

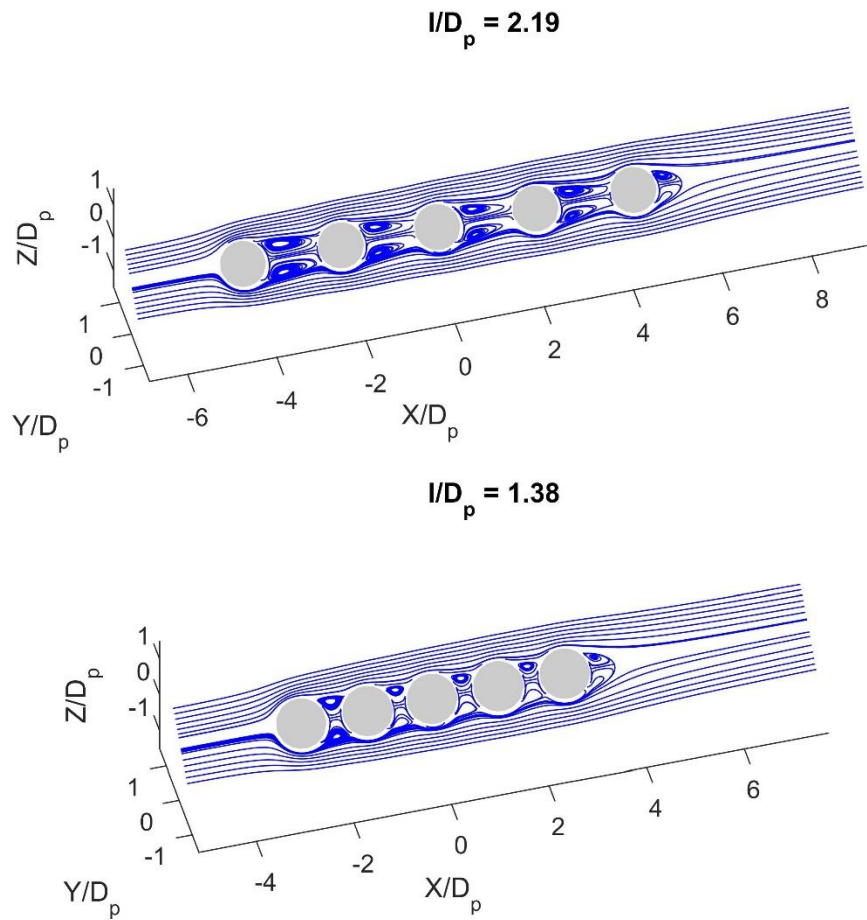


Figure 6.12 Three dimensional streamlines for train of five particles using PR-DNS results.

Comparison of the results between simulation and experiment are first shown as overlaid contours of axial and transverse components of velocity. Figure 6.13 and Figure 6.14 show contour plots of the numerical results in color and the experimental results as lines. Due to the symmetry of the velocity field, the flow field on the shadowed side of the spheres is not plotted in these figures, and only the upper half of the flow field is shown. Lines of experimental data are expected to follow the border of colored contours of simulation results and in both figures, the experimental and numerical results are in good agreement. It can be noted that the contour levels of the two methods agree very closely in the regions close to the

train of spheres, however some discrepancy is seen in the area between the spheres and wall and also in the wall boundary layer, where the experiments show a higher velocity than the simulations. It should be noted that in the experiments, the spheres are supported using 2 mm diameter stings normal to the field of measurement as shown in Figure 6.1 whereas the simulation geometry was setup without the sting. It is also not possible to experimentally achieve a perfect uniform inlet velocity as is assumed in the simulation. Plots of velocity profile are shown in the following to discuss the flow field in more detail.

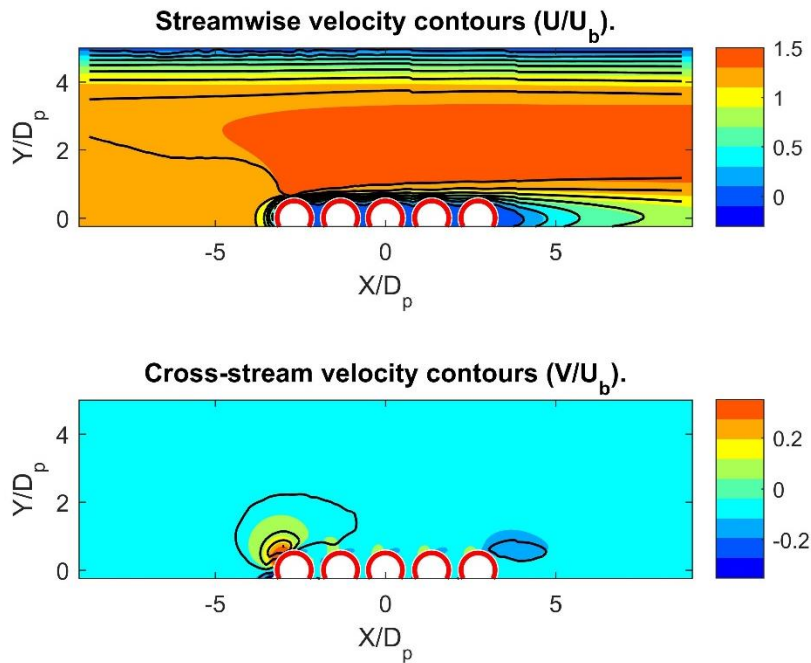


Figure 6.13 Comparison of the contours of velocity components between simulation (color) and experiment (line) for  $l/D_p = 1.38$ .

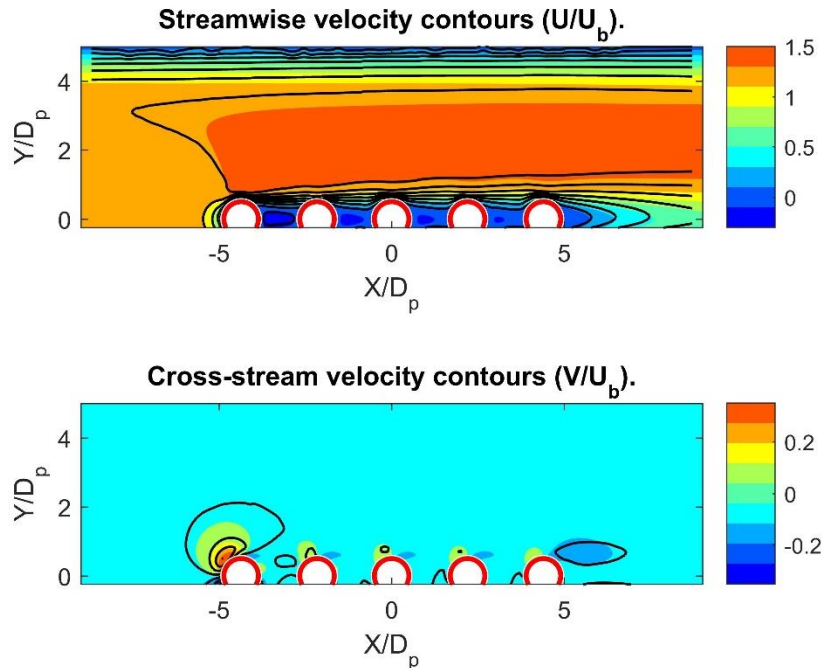


Figure 6.14 Comparison of the contours of velocity components between simulation (color) and experiment (line) for  $l/D_p = 2.19$ .

The velocity field shown in Figure 6.13 and Figure 6.14 further supports the idea that only using a comparison of drag force on the spheres as a verification can prove to not be reliable for simulation validation since the drag force is merely a local measurement of the velocity gradient on the spheres and is barely influenced by the velocity field away from the spheres. Velocity field measurement such as the current study, on the other hand, allow for a more detailed comparison of the results and are a more reliable source for validation of simulation results.

In the following figures, velocity profiles at various locations are extracted and wherever the resulting curves from different locations or different cases were found to show very similar features, for the sake of brevity, only one representative case was shown for each comparison. Temporal variation of the velocity field in experimental results are almost non-existent due to the laminar flow. All the experimental results are depicted as the ensemble

average field of the 3333 measured velocity fields for each case using markers. Numerical results are depicted as lines overlaid on the same plot using a similar color.

The streamwise component of velocity vs. axial location at different transverse locations is depicted in Figure 6.15 and Figure 6.16 for three different transverse locations that represent the centerline of the duct, one location close to the train of spheres and one location inside the wall boundary layer for  $l/D_p = 1.38$  and  $2.19$  respectively. These plots reveal that the numerical results follow the experiments closely with about a 7% difference, although there are some differences between simulation and experiment. Both the simulations and experiments show that the negative streamwise velocity between spheres is larger between the first two spheres and the peak negative velocity in between the spheres diminishes moving to each successive downstream sphere.

Comparing the results for the two different particle spacings, one major difference between the cases is in the negative streamwise velocity regions between the spherical particles. The magnitude of this negative streamwise velocity is a measure of the strength of the recirculation zones that form between the spheres. The case of the closer particle formation shows an almost zero velocity between the spheres, and thus a nearly stagnant flow region between the spheres. One consequence of this is that once a fluid particle enters this region, it becomes trapped, as it is difficult to exit this stagnant region. In this case, the train of particles can be taken as a single, larger particle, whereas the farther particle formation must be treated as individual particles, since the flow structure in the region between the spheres cannot be neglected.

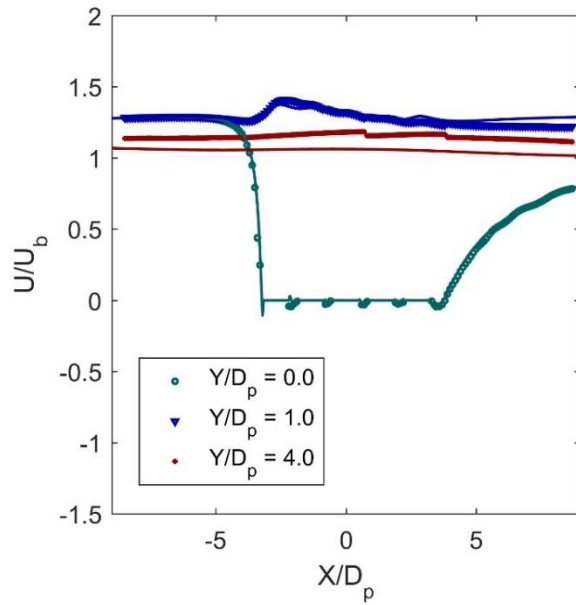


Figure 6.15 Comparison of axial velocity profile along axial lines at different transverse locations for train of 5 spheres at  $l/D_p = 1.38$ . The lines represent the PR-DNS data and the symbols represent the experimental data.

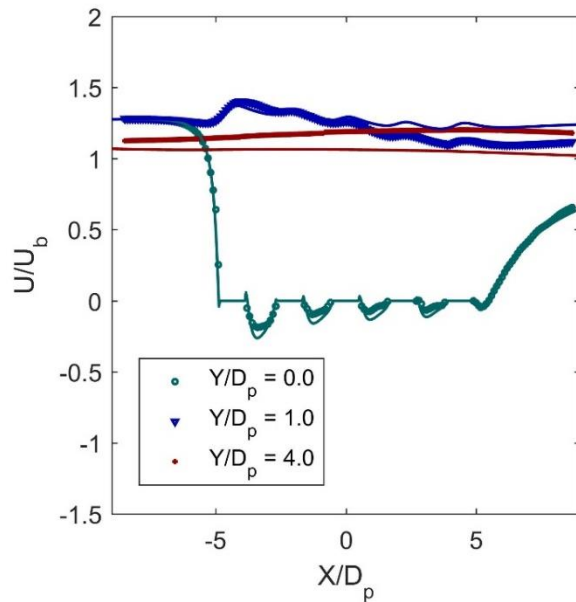


Figure 6.16 Comparison of axial velocity profile along axial lines at different transverse locations for train of 5 spheres at  $l/D_p = 2.19$ . The lines represent the PR-DNS data and the symbols represent the experimental data.

The streamwise velocity profile along the transverse centerline of the spheres is shown in Figure 6.17 and Figure 6.18 for the first, second, and last sphere in the arrangement for  $l/D_p = 1.38$  and 2.19 respectively (profiles for the third and fourth spheres are removed here for the sake of clarity in the figure). The boundary layers forming on the surface of the spheres is clearly observed in the numerical simulations, and it is evident that the first sphere has a different impact on the flow comparing to the rest of the spheres in the arrangement. In both cases, only the leading sphere causes a peak in the velocity profile. As was previously discussed, the flow inside the duct in between the train of spheres and wall shows a slightly higher velocity in experiments compared to the simulations. A closer look at Figure 6.17 and Figure 6.18 shows that the difference lies in a slightly wider wall boundary layer in the simulations. On average, the results are about 10% different between the experiment and simulation.

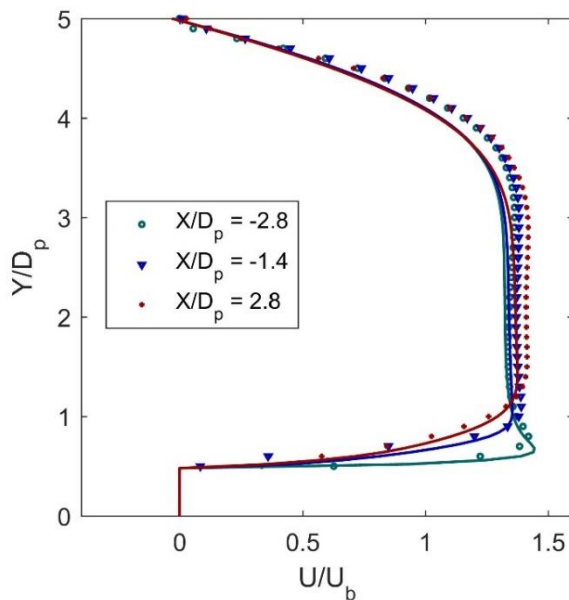


Figure 6.17 Streamwise velocity profile along transverse lines along the center of particles at  $l/D_p = 1.38$ . The lines represent the PR-DNS data and the symbols represent the experimental data.

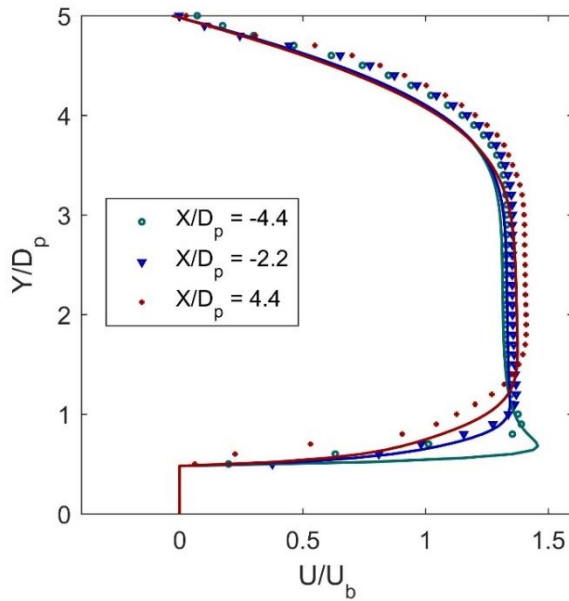


Figure 6.18 Streamwise velocity profile along transverse lines along the center of particles at  $l/D_p = 2.19$ . The lines represent the PR-DNS data and the symbols represent the experimental data.

Figure 6.19 and Figure 6.20 show streamwise velocity plotted vs. transverse location for profile locations midway between pairs of spheres for  $l/D_p = 1.38$  and  $2.19$  respectively. Two such profiles are shown, corresponding to the middle of the gaps between the first and last pair of spheres and the rest were omitted for the clarity of the figure. It can be seen that in the closer arrangement of the spheres, where  $l/D_p = 1.38$ , the velocity profiles at different downstream locations match each other almost exactly with a zero velocity in the center. However, for  $l/D_p = 2.19$ , velocity profiles are different. In that case, the first sphere has a relatively larger peak negative velocity along the sphere train centerline. In both cases, the agreement between simulation and experiments are very good with about an average 7% difference.

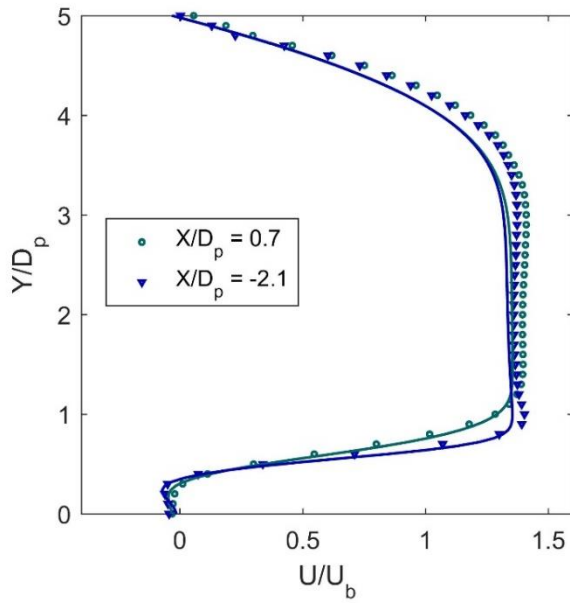


Figure 6.19 Streamwise velocity profile along transverse lines along middle of the first and last pair of spheres at  $l/D_p = 1.38$ . The lines represent the PR-DNS data and the symbols represent the experimental data.

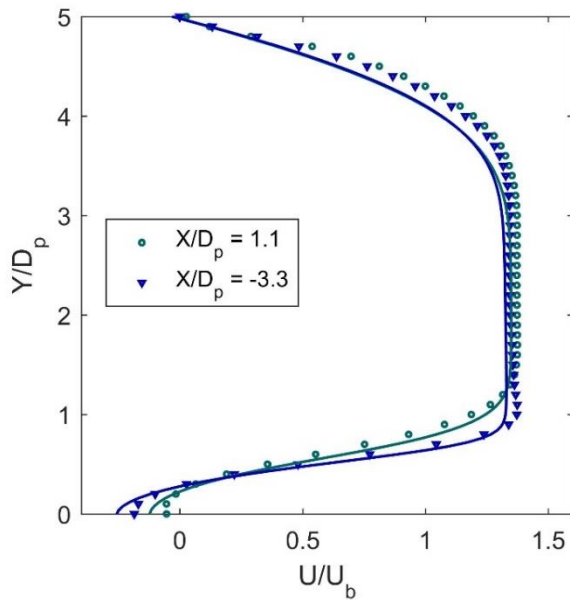


Figure 6.20 Streamwise velocity profile along transverse lines along middle of the first and last pair of spheres at  $l/D_p = 2.19$ . The lines represent the PR-DNS data and the symbols represent the experimental data.

Figure 6.21 and Figure 6.22 show velocity profile development downstream of the train of particles at 4 different axial locations for  $l/D_p = 1.38$  and 2.19 respectively. The locations plotted here correspond to 1, 3, 6, and 9 diameters downstream of the last sphere in the train arrangement. The region corresponding to the wake behind the train of particles ( $Y/D_p < 0.5$ ) are in very close agreement between the experiments and simulation. However, as was previously observed, the lower simulation velocity in the region between the wake and wall when compared to the experimental results still persists. The results from simulations are on average about 7% different from experimental measurements.

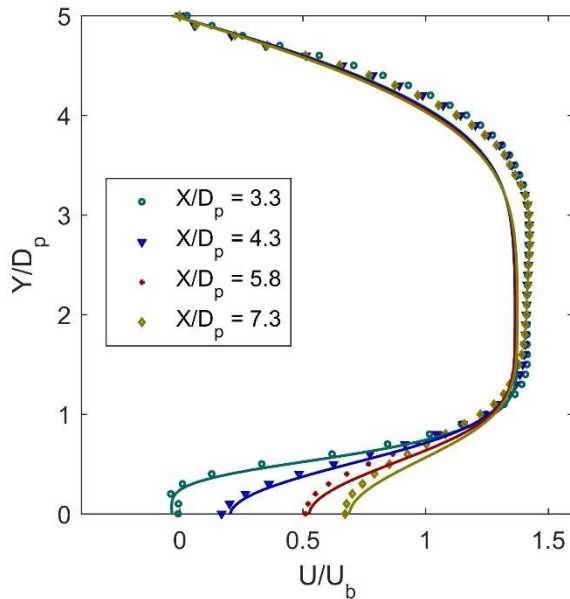


Figure 6.21 Streamwise velocity profile along transverse lines downstream the particle train of 5 spheres at  $l/D_p = 1.38$ . The lines represent the PR-DNS data and the symbols represent the experimental data.

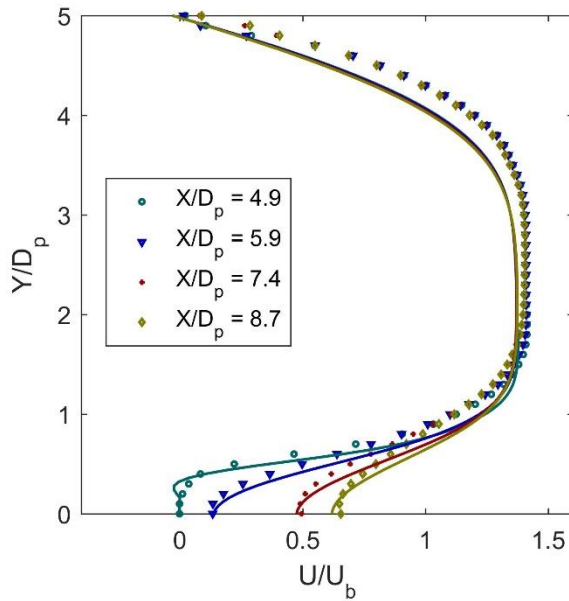


Figure 6.22 Streamwise velocity profile along transverse lines downstream the particle train of 5 spheres at  $U/D_p = 2.19$ . The lines represent the PR-DNS data and the symbols represent the experimental data.

Measuring the transverse component of velocity can be more difficult due to the transverse velocity components being approximately one order of magnitude smaller than the streamwise velocity component in most of the field. The difficulty merely is due to the inherent limitation of the PIV method for capturing a wide range of velocity vectors which is the dynamic range of this method (Adrian, 1999). Errors in PIV measurements are minimized by increasing the distance particles move between laser pulses, since this reduces the effect of sub-pixel displacement interpolation errors on the measured velocity. When transverse velocities are small relative to streamwise velocities, the measured transverse velocities will be more dependent on sub-pixel interpolation, and hence, have greater potential measurement error. Moreover, near zero velocity measurements suffer more from any small misalignments in either the laser sheet or the cameras. Despite these potential limitations, comparisons in

transverse velocity here shown in Figure 6.23 and Figure 6.24 have an outstanding agreement between simulations and experiments with less than 2% average difference in the results.

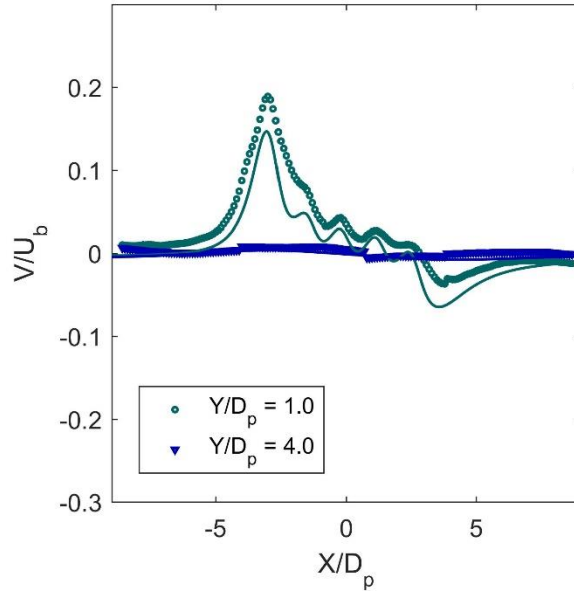


Figure 6.23 Comparison of transverse velocity profile along axial lines at different transverse locations for train of 5 spheres at  $l/D_p = 1.38$ . The lines represent the PR-DNS data and the symbols represent the experimental data.

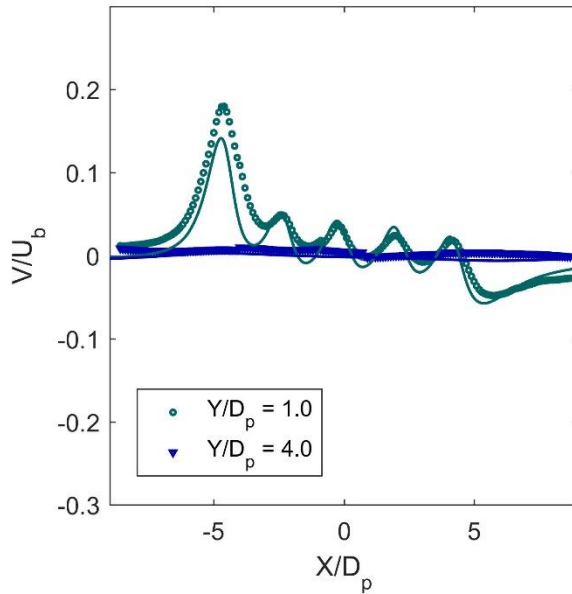


Figure 6.24 Comparison of transverse velocity profile along axial lines at different transverse locations for train of 5 spheres at  $l/D_p = 2.19$ . The lines represent the PR-DNS data and the symbols represent the experimental data.

Figure 6.23 and Figure 6.24 show a comparison of the transverse velocity component along axial profiles close to the wall (four sphere diameters from the train centerline) and close to the train of spheres (one sphere diameter from the train centerline). Other locations are not shown due to all values being virtually identical to the  $Y/D = 4.0$  results. It can be observed that the transverse velocity features are well captured by the numerical simulations. The peaks in these figures show that the flow is expelled away from the spheres and the first sphere shows a much higher intensity comparing to the rest of the spheres. In the area between the spheres, for the more packed case studied, there is virtually no entrainment of fluid and the corresponding valleys have positive velocities whereas for the less packed case, there is small negative velocities showing an entrainment of fluid between the particles. The biggest valley on the far right side of the figures corresponds to the vertical wake region downstream the train of particles where a major entrainment of flow occurs

## 6.5 Conclusions

Experimental field velocity measurements using Particle Image Velocimetry (PIV) and numerical simulation using Particle Resolved Direct Numerical Simulation (PR-DNS) was performed for the case of a train of 5 inline spherical particles in the center of a square duct with water flowing at a Reynolds number of 100. It was shown that even though the velocity in the vicinity of particles match greatly between the experiments and simulations, some discrepancies exist in the far field. Even though those areas are of lesser interest in multiphase fluid simulations, further investigations will be performed in order to find the reason for this discrepancy. It was concluded that local measurements such as drag force cannot be reliably used for validation of simulation results and field value measurements are required for that purpose.

A direct comparison of the velocity field for the flow past a train of 5 particles inside a square duct at 2 different distance to diameter ratios was presented between PIV experimental data PR-DNS. The simulation data were validated using the experimental results showing an average of about 7% difference for most cases studied and a maximum of less than 10% difference. It was observed that the flow-particle interaction for the two different particle separation distances are very different. The closer arrangement allows practically no penetration of flow between the particles which causes the particles to stay as a cluster whereas the farther away arrangement allows penetration of fluid between the particles and they interact with the surrounding flow as individual particle despite being influenced by the rest of particles in the arrangement. The velocity field values outside the train of particles in the two cases were fairly similar showing that the interaction of the flow field with the arrangement of particles is practically independent of the distance between the particles in the arrangement.

## 6.6 Acknowledgements

The authors acknowledge great discussion and helpful insights of our colleague, Mohammad Mehrabadi and efforts of undergraduate laboratory assistant Ekoue Kangni. We also gratefully acknowledge financial support for this work from the National Science Foundation (CBET-1034307).

## CHAPTER 7

### CONCLUSION

Experimental measurements were performed to obtain bubble size and shape distributions and liquid phase volumetric mass transfer coefficients in a vertically oriented semi-batch Taylor-Couette reactor for several combinations of axial and azimuthal Reynolds numbers. The study was followed by investigation of the effect of interfacial surface tension on these parameters using ethanol as the surfactant. Experiments were done at several combinations of rotational speed, gas flow rate, and surfactant concentration.

Bubble size distributions were found to be log-normally distributed, and the Sauter mean diameter was shown to monotonically increase with increasing inner cylinder rotation speed and gas flow rate according to a power law relation. Sauter mean diameter was shown to generally decrease with higher concentrations of ethanol corresponding to lower interfacial surface tension. This effect is non-linear with higher reduction of the bubble size at lower concentrations of surfactant. Empirical correlations for calculation of the Sauter mean bubble diameter as a function of azimuthal and axial Reynolds numbers and Capillary number were proposed. Bubbles were found to have an average ellipticity of 1.2-2.0 even though there seems to be no apparent correlation of ellipticity with the parameters studied here. Bubble size and shape measurements demonstrate that bubbles have higher aspect ratio in annular columns compared to those observed in cylindrical columns and the shearing flow causes them to take on the shape of prolate spheroids rather than the commonly observed oblate shape in bubble columns.

Mass transfer coefficients for cases with no surfactant were acquired using both needles and sparge stones for gas inlet and the difference were discussed. It was shown that the mass

transfer coefficient increases monotonically by increasing the azimuthal and axial Reynolds numbers. It was observed that introduction of the surfactant generally causes an increase in mass transfer coefficient at lower concentrations and higher concentrations of surfactant has little impact on mass transfer. Correlations were proposed for calculation of the Sherwood number in terms of azimuthal and axial Reynolds numbers and Capillary number. Several comparisons of the results were made with other available correlations for different types of reactors.

Simulation of gas–liquid mass transfer in a Taylor vortex reactor was performed by using a two-fluid CFD model to obtain local phase distribution and velocity field information, which in turn was used to select an appropriate mass transfer model for computing the volumetric mass transfer coefficient,  $k_{LA}$ . The mass transfer model is based upon the Higbie theory, but automatically adapts to the local hydrodynamic environment by computing exposure time using either the penetration theory or eddy cell model based upon the turbulence dissipation rate. This approach was validated by comparing simulation predictions with experimental measurements for the temporal evolution of the concentration of dissolved oxygen at a specific location in the reactor in response to a step change in feed gas composition. The simulations support the assumption that measurements at a single location in the reactor are sufficient for determining the mass transfer coefficient and it was noted that determination of  $k_{LA}$  from experimental data at a single location also requires that the local liquid saturation concentration only depends upon temperature. Such an assumption can be justified if the gas phase partial pressures do not vary strongly with position. Simulation results show that gas bubbles are mostly located near the inner cylinder causing most of the interphase mass transfer to occur near the inner cylinder wall. The cylinder rotation speed, in contrast to the gas feed

flow rate, strongly impacts the bubble diameter, slip velocity, and turbulence dissipation rate. The gas flow rate has a greater effect than the cylinder speed on gas holdup,  $\alpha_g$ , but because the holdup is small (<2%) even for the highest gas flow rates studied, the rate of interphase mass transfer in general depends more strongly on the azimuthal Reynolds number, in agreement with experimental findings for this system.

Experiments were performed with a train of 3 or 5 spherical particles arranged inline on the centerline of a square duct at 5 different distance over diameter ratios in order to characterize the interaction of flow with a cluster of particles. Velocity field data was presented and studies showing that the behavior of flow is merely a function of the distance and almost independent of the number of spheres in the arrangement. The higher packed arrangement seems to not allow the flow between the spheres and act as a cluster whereas the lower packed arrangements allow the flow between them to interact with the particles and either pull the together or push them away depending on the distance over diameter ratio. The interaction of multiple spheres with flow was contrasted with the case of a single sphere. Within the arrangement, it was noted that the most upstream sphere causes quite different flow patterns in comparison to the rest of the arrangement.

Particle Resolved Direct Numerical Simulation (PR-DNS) were performed for identical geometries as that of Particle Image Velocimetry (PIV) measurement. It was shown that even though the velocity in the vicinity of particles match greatly between the experiments and simulations, some discrepancies exist in the far field. It was concluded that local measurements such as drag force cannot be reliably used for validation of simulation results and field value measurements are required for that purpose. A direct comparison of the velocity

field for the flow past a train of 5 particles inside a square duct at 2 different distance to diameter ratios was presented between PIV experimental data PR-DNS. The simulation data was validated using the experimental results showing an average of about 7% difference for most cases studied and a maximum of less than 10% difference.

## CHAPTER 8 REFERENCES

- Achenbach, E., 1974. Vortex shedding from spheres. *J. Fluid Mech.* 62, 209.  
doi:10.1017/S0022112074000644
- Adrian, R.J., 1999. Dynamic ranges of velocity and spatial resolution of particle image velocimetry. *Meas. Sci. Technol.* 8, 1393–1398. doi:10.1088/0957-0233/8/12/003
- Akita, K., Yoshida, F., 1974. Bubble Size, Interfacial Area, and Liquid-Phase Mass Transfer Coefficient in Bubble Columns. *Ind. Eng. Chem., Process Des. Dev.* 13, 84–90.  
doi:10.1021/i260045a015
- Akita, K., Yoshida, F., 1973. Gas Holdup and Volumetric Mass Transfer Coefficient in Bubble Columns. Effects of Liquid Properties. *Ind. Eng. Chem. Process Des. Dev.* 12, 76–80.  
doi:10.1021/i260045a015
- Alves, S.S., Maia, C.I., Vasconcelos, J.M.T., Serralheiro, A.J., 2002. Bubble size in aerated stirred tanks. *Chem. Eng. J.* 89, 109–117. doi:10.1016/S1385-8947(02)00008-6
- Alves, S.S., Vasconcelos, J.M.T., Orvalho, S.P., 2006. Mass transfer to clean bubbles at low turbulent energy dissipation, *Chemical Engineering Science*.  
doi:10.1016/j.ces.2005.08.001
- Anastasiou, A.D., Kazakis, N.A., Mouza, A.A., Paras, S. V., 2010. Effect of organic surfactant additives on gas holdup in the pseudo-homogeneous regime in bubble columns equipped with fine pore sparger. *Chem. Eng. Sci.* 65, 5872–5880. doi:10.1016/j.ces.2010.08.011
- Andereck, C.D., Liu, S.S., Swinney, H.L., 1986. Flow regimes in a circular Couette system with independently rotating cylinders. *J. Fluid Mech.* doi:10.1017/S0022112086002513

- Antal, S.P., Lahey, R.T., Flaherty, J.E., 1991. Analysis of phase distribution in fully developed laminar bubbly two-phase flow. *Int. J. Multiph. Flow* 17, 635–652. doi:10.1016/0301-9322(91)90029-3
- Asgharpour, M., Mehrnia, M.R., Mostoufi, N., 2010. Effect of surface contaminants on oxygen transfer in bubble column reactors. *Biochem. Eng. J.* 49, 351–360. doi:10.1016/j.bej.2010.01.010
- Bachalo, W.D., 1994. Experimental methods in multiphase flows. *Int. J. Multiph. Flow.* doi:10.1016/0301-9322(94)90075-2
- Baier, G., Graham, M.D., 2000. Two-fluid Taylor-Couette flow with countercurrent axial flow: Linear theory for immiscible liquids between corotating cylinders. *Phys. Fluids* 12, 294. doi:10.1063/1.870308
- Baier, G., Graham, M.D., Lightfoot, E.N., 2000. Mass transport in a novel two-fluid Taylor vortex extractor. *AIChE J.* 46, 2395–2407. doi:10.1002/aic.690461208
- Battino, R., Rettich, T.R., Tominaga, T., 1983. The Solubility of Oxygen and Ozone in Liquids. *J. Phys. Chem. Ref. Data* 12, 163–177. doi:10.1063/1.555680
- Behkish, A., Lemoine, R., Sehabiague, L., Oukaci, R., Morsi, B.I., 2007. Gas holdup and bubble size behavior in a large-scale slurry bubble column reactor operating with an organic liquid under elevated pressures and temperatures. *Chem. Eng. J.* 128, 69–84. doi:10.1016/j.cej.2006.10.016
- Behzadi, A., Issa, R.I., Rusche, H., 2004. Modelling of dispersed bubble and droplet flow at high phase fractions. *Chem. Eng. Sci.* 59, 759–770. doi:10.1016/j.ces.2003.11.018

- Belo, I., Garcia-Abuin, A., Gomez-Diaz, D., Navaza, M.J., Vidal-Tato, I., 2011. Effect of tween 80 on bubble size and mass transfer in a bubble contactor. *Chem. Eng. Technol.* doi:10.1002/ceat.201100140
- Benedek, A., Heideger, W.J., 1971. Effect of Additives on Mass Transfer in Turbine Aeration. *Biotechnol. Bioeng.* 663–684. doi:10.1002/bit.260130507
- Bilson, M., Bremhorst, K., 2007. Direct numerical simulation of turbulent Taylor–Couette flow. *J. Fluid Mech.* doi:10.1017/S0022112007004971
- Bouaifi, M., Hebrard, G., Bastoul, D., Roustan, M., 2001. A comparative study of gas hold-up, bubble size, interfacial area and mass transfer coefficients in stirred gas-liquid reactors and bubble columns. *Chem. Eng. Process.* 40, 97–111. doi:10.1016/S0255-2701(00)00129-X
- Brown, A.H., Fredrickson, A.G., Miller, R.L., Tsuchiya, H.M., 1964. Hydromechanical method to increase efficiency of algal photosynthesis. *Ind. Eng. Chem. Process Des. Dev.* 3, 134–143. doi:10.1021/i260010a008
- Buffo, A., Marchisio, D.L., 2014. Modeling and simulation of turbulent polydisperse gas-liquid systems via the generalized population balance equation. *Rev. Chem. Eng.* 30, 73–126. doi:10.1515/revce-2013-0015
- Calderbank, P.H., Lochiel, A.C., 1964. Mass transfer coefficients, velocities and shapes of carbon dioxide bubbles in free rise through distilled water. *Chem. Eng. Sci.* doi:10.1016/0009-2509(64)85075-2
- Campero, R., Vigil, R., 1999. Flow patterns in liquid-liquid Taylor-Couette-Poiseuille flow. *Ind. Eng. Chem. Res.* 38, 1094–1098.

- Campero, R., Vigil, R., 1997. Spatiotemporal Patterns in Liquid-Liquid Taylor-Couette-Poiseuille Flow. *Phys. Rev. Lett.* doi:10.1103/PhysRevLett.79.3897
- Capecelatro, J., Desjardins, O., Fox, R.O., 2014. Numerical study of collisional particle dynamics in cluster-induced turbulence. *J. Fluid Mech.* 747, R2. doi:10.1017/jfm.2014.194
- Chaumat, H., Billet, A.M., Delmas, H., 2007. Hydrodynamics and mass transfer in bubble column: Influence of liquid phase surface tension. *Chem. Eng. Sci.* 62, 7378–7390. doi:10.1016/j.ces.2007.08.077
- Chen, R.C., Wu, J.L., 2000. The flow characteristics between two interactive spheres. *Chem. Eng. Sci.* 55, 1143–1158. doi:10.1016/S0009-2509(99)00390-5
- Chen, S., Yeh, A., Wu, J, S., 1997. Effects of particle radius, fluid viscosity and relative velocity on the surface heat transfer coefficient of spherical particles at low Reynolds numbers. *J. Food Eng.* 31, 473–484. doi:10.1016/S0260-8774(96)00093-3
- Chen, X., Liu, G. hua, Fan, H., Li, M., Luo, T., Qi, L., Wang, H., 2013. Effects of surfactant contamination on oxygen mass transfer in fine bubble aeration process. *Korean J. Chem. Eng.* doi:10.1007/s11814-013-0092-x
- Chern, J.M., Chou, S.R., Shang, C.S., 2001. Effects of impurities on oxygen transfer rates in diffused aeration systems. *Water Res.* 35, 3041–3048. doi:10.1016/S0043-1354(01)00031-8
- Chouippe, A., Climent, E., Legendre, D., Gabillet, C., 2014. Numerical simulation of bubble dispersion in turbulent Taylor-Couette flow. *Phys. Fluids* 26, 043304. doi:10.1063/1.4871728
- Clift, R., Grace, J., Weber, M., 2005. *Bubbles, drops, and particles.*

- Cockx, A., Do-Quang, Z., Audic, J., Liné, A., Roustan, M., 2001. Global and local mass transfer coefficients in waste water treatment process by computational fluid dynamics. *Chem. Eng. Process. Process Intensif.* 40, 187–194. doi:10.1016/S0255-2701(00)00138-0
- Coles, D., 1964. Transition in circular couette flow. *J. Fluid Mech.* 21, 385. doi:10.1017/S0022112065000241
- Colombet, D., Legendre, D., Cockx, A., Guiraud, P., Risso, F., Daniel, C., Galinat, S., 2011. Experimental study of mass transfer in a dense bubble swarm. *Chem. Eng. Sci.* 66, 3432–3440. doi:10.1016/j.ces.2011.01.020
- Dai, J., Grace, J.R., 2010. Blockage of constrictions by particles in fluid-solid transport. *Int. J. Multiph. Flow* 36, 78–87. doi:10.1016/j.ijmultiphaseflow.2009.08.001
- Davis, M.W., Weber, E.J., 1960. Liquid-Liquid Extraction between Rotating Concentric Cylinders. *Ind. Eng. Chem.* 52, 929–934. doi:10.1021/ie50611a027
- Deckwer, W.-D.D., Burckhart, R., Zoll, G., 1974. Mixing and mass transfer in tall bubble columns. *Chem. Eng. Sci.* 29, 2177–2188. doi:10.1016/0009-2509(74)80025-4
- Djeridi, H., Gabillet, C., Billard, J.Y., 2004. Two-phase Couette-Taylor flow: Arrangement of the dispersed phase and effects on the flow structures. *Phys. Fluids* 16, 128–139. doi:10.1063/1.1630323
- Dłuska, E., Wroński, S., Hubacz, R., Dłuska, E., Wronski, S., Hubacz, R., 2001. Mass transfer in gas-liquid Couette-Taylor flow reactor. *Chem. Eng. Sci.* 56, 1131–1136. doi:10.1016/s0009-2509(00)00331-6
- Dłuska, E., Wroński, S., Ryszczyk, T., 2004. Interfacial area in gas-liquid Couette-Taylor flow reactor. *Exp. Therm. Fluid Sci.* 28, 467–472. doi:10.1016/j.expthermflusci.2003.06.003

- Dong, S., 2007. Direct numerical simulation of turbulent Taylor–Couette flow. *J. Fluid Mech.*  
doi:10.1017/S0022112007007367
- Donnelly, R.J., 1991. Taylor-Couette flow: The early days. *Phys. Today* 44, 32–39.  
doi:10.1063/1.881296
- Drew, D.A., Lahey, R.T., 1993. Analytical Modeling of Multiphase Flow, in: *Particulate Two-Phase Flow*.
- Dumont, E., Andrès, Y., Le Cloirec, P., 2006. Effect of organic solvents on oxygen mass transfer in multiphase systems: Application to bioreactors in environmental protection. *Biochem. Eng. J.* 30, 245–252. doi:10.1016/j.bej.2006.05.003
- Dusting, J., Balabani, S., 2009. Mixing in a Taylor-Couette reactor in the non-wavy flow regime. *Chem. Eng. Sci.* 64, 3103–3111. doi:10.1016/j.ces.2009.03.046
- Dutta, P.K., Ray, A.K., 2004. Experimental investigation of Taylor vortex photocatalytic reactor for water purification. *Chem. Eng. Sci.* doi:10.1016/j.ces.2004.07.091
- Ergun, S., Orning, a. a., 1949. Fluid Flow through Randomly Packed Columns and Fluidized Beds. *Ind. Eng. Chem.* 41, 1179–1184. doi:10.1021/ie50474a011
- Fenstermacher, P.R., Swinney, H.L., Gollub, J.P., 1979. Dynamical instabilities and the transition to chaotic Taylor vortex flow. *J. Fluid Mech.* doi:10.1017/S0022112079000963
- Ferri, J.K., Stebe, K.J., 2000. Which surfactants reduce surface tension faster? A scaling argument for diffusion-controlled adsorption. *Adv. Colloid Interface Sci.* 85, 61–97.  
doi:10.1016/S0001-8686(99)00027-5
- Fox, R.O., 2014. On multiphase turbulence models for collisional fluid–particle flows. *J. Fluid Mech.* 742, 368–424. doi:10.1017/jfm.2014.21

- Fox, R.O., 2012. Large-Eddy-Simulation Tools for Multiphase Flows. *Annu. Rev. Fluid Mech.* 44, 47–76. doi:10.1146/annurev-fluid-120710-101118
- Gao, X., Kong, B., Ramezani, M., Olsen, M.G., Vigil, R.D., 2015a. An adaptive model for gas–liquid mass transfer in a Taylor vortex reactor. *Int. J. Heat Mass Transf.* 91, 433–445. doi:10.1016/j.ijheatmasstransfer.2015.07.125
- Gao, X., Kong, B., Vigil, R.D., 2015b. CFD investigation of bubble effects on Taylor–Couette flow patterns in the weakly turbulent vortex regime. *Chem. Eng. J.* 270, 508–518. doi:10.1016/j.cej.2015.02.061
- Gao, X., Wang, L.J., Wu, C., Cheng, Y.W., Li, X., 2013. Novel bubble-emulsion hydrodynamic model for gas-solid bubbling fluidized beds. *Ind. Eng. Chem. Res.* 52, 10835–10844. doi:10.1021/ie4002298
- Garcia-Abuin, A., Gomez-Diaz, D., Losada, M., Navaza, J.M., 2013. Oxygen absorption in polymer+surfactant aqueous solutions. *Chem. Eng. J.* 225, 76–83. doi:10.1016/j.cej.2013.03.067
- Garcia-Abuin, A., Gomez-Diaz, D., Losada, M.M., Navaza, J.M.J.M., 2012. Bubble column gas-liquid interfacial area in a polymer+surfactant+water system. *Chem. Eng. Sci.* 75, 334–341. doi:10.1016/j.ces.2012.03.054
- Garcia-Abuin, A., Gomez-Diaz, D., Navaza, J.M., Sanjurjo, B., 2010. Effect of surfactant nature upon absorption in a bubble column. *Chem. Eng. Sci.* 65, 4484–4490. doi:10.1016/j.ces.2010.04.009
- Garcia-Ochoa, F., Gomez, E., 2009. Bioreactor scale-up and oxygen transfer rate in microbial processes: An overview, *Biotechnology Advances*. Elsevier Inc. doi:10.1016/j.biotechadv.2008.10.006

- Garcia-Ochoa, F., Gomez, E., 2005. Prediction of gas-liquid mass transfer coefficient in sparged stirred tank bioreactors. *Biotechnol. Bioeng.* 92, 761–772. doi:10.1002/bit.20638
- Garcia-Ochoa, F., Gomez, E., 2004. Theoretical prediction of gas-liquid mass transfer coefficient, specific area and hold-up in sparged stirred tanks. *Chem. Eng. Sci.* 59, 2489–2501. doi:10.1016/j.ces.2004.02.009
- García-Ochoa, F., Gómez, E., 1998. Mass transfer coefficient in stirred tank reactors for xanthan gum solutions. *Biochem. Eng. J.* 1, 1–10. doi:10.1016/S1369-703X(97)00002-8
- Goldstein, R.J., Kreid, D.K., 1967. Measurement of laminar flow development in a square duct using a laser-Doppler flowmeter. *J. Appl. Mech.* 34, 813. doi:10.1115/1.3607839
- Gomez-Diaz, D., Gomes, N., Teixeira, J.A.J.A., Belo, I., 2009. Oxygen mass transfer to emulsions in a bubble column contactor. *Chem. Eng. J.* 152, 354–360. doi:10.1016/j.cej.2009.04.059
- Gomez-Diaz, D., Navaza, J.M., Sanjurjo, B., 2009. Mass-transfer enhancement or reduction by surfactant presence at a gas-liquid interface. *Ind. Eng. Chem. Res.* 48, 2671–2677. doi:10.1021/ie8009523
- Gomez-Diaz, D., Navaza, J.M., Sanjurjo, B., 2008. Interfacial area evaluation in a bubble column in the presence of a surface-active substance. Comparison of methods. *Chem. Eng. J.* 144, 379–385. doi:10.1016/j.cej.2008.02.002
- Gourich, B., Vial, C., El Azher, N., Belhaj Soulami, M., Ziyad, M., 2006. Improvement of oxygen mass transfer estimation from oxygen concentration measurements in bubble column reactors. *Chem. Eng. Sci.* 61, 6218–6222. doi:10.1016/j.ces.2006.04.045
- Griffith, R.M., 1960. Mass transfer from drops and bubbles. *Chem. Eng. Sci.* 12, 198–213. doi:10.1016/0009-2509(60)85006-3

- Ham, J.M., Homsy, G.M., 1988. Hindered settling and hydrodynamic dispersion in quiescent sedimenting suspensions. *Int. J. Multiph. Flow* 14, 533–546. doi:10.1016/0301-9322(88)90056-0
- Hassan, R., Loubiere, K., Legrand, J., Delaplace, G., 2012. A consistent dimensional analysis of gas-liquid mass transfer in an aerated stirred tank containing purely viscous fluids with shear-thinning properties. *Chem. Eng. J.* doi:10.1016/j.cej.2011.12.066
- Haut, B., Ben Amor, H., Coulon, L., Jacquet, A., Halloin, V., Amor, H. Ben, Coulon, L., Jacquet, A., Halloin, V., 2003. Hydrodynamics and mass transfer in a Couette-Taylor bioreactor for the culture of animal cells. *Chem. Eng. Sci.* 58, 777–784. doi:10.1016/S0009-2509(02)00607-3
- Hebrard, G., Zeng, J., Loubiere, K., 2009. Effect of surfactants on liquid side mass transfer coefficients: A new insight. *Chem. Eng. J.* 148, 132–138. doi:10.1016/j.cej.2008.08.027
- Heijnen, J.J., Van ' K., Riet, T., Van't Riet, K., 1984. Mass transfer, mixing and heat transfer phenomena in low viscosity bubble column reactors. *Chem. Eng. J.* 28, B21–B42. doi:10.1016/0300-9467(84)85025-X
- Hicks, R.E., 1970. Pressure drop in packed beds of spheres 9, 500–502. doi:10.1021/i160035a032
- Higbie, R., 1935. The rate of absorption of a pure gas into a still liquid during short periods of exposure. *Trans. Am. Inst. Chem. Eng.* 31, 365–389.
- Hill, G.A., 2006. Measurement of overall volumetric mass transfer coefficients for carbon dioxide in a well-mixed reactor using a pH probe. *Ind. Eng. Chem. Res.* 45, 5796–5800. doi:10.1021/ie060242t

- Hills, J.H., 1976. The operation of a bubble column at high throughputs: I. Gas holdup measurements. *Chem. Eng. J.* 12, 89–99. doi:10.1016/0300-9467(76)87002-5
- Huang, Q., Yang, C., Yu, G., Mao, Z.-S., 2010. CFD simulation of hydrodynamics and mass transfer in an internal airlift loop reactor using a steady two-fluid model. *Chem. Eng. Sci.* 65, 5527–5536. doi:10.1016/j.ces.2010.07.021
- Hubacz, R., Wroński, S., 2004. Horizontal Couette–Taylor flow in a two-phase gas–liquid system: flow patterns. *Exp. Therm. Fluid Sci.* 28, 457–466. doi:10.1016/j.expthermflusci.2003.07.004
- Hur, Y.G., Yang, J.H., Jung, H., Lee, K.Y., 2014. Continuous alcohol addition in vaporized form and its effect on bubble behavior in a bubble column. *Chem. Eng. Res. Des.* 92, 804–811. doi:10.1016/j.cherd.2013.08.006
- Imamura, T., Saito, K., Ishikura, S., Nomura, M., 1993. A new approach to continuous emulsion polymerization. *Polym. Int.* 30, 203–206. doi:10.1002/pi.4990300210
- Jadoon, A., Prahl, L., Revstedt, J., 2010. Dynamic interaction of fixed dual spheres for several configurations and inflow conditions. *Eur. J. Mech. B/Fluids* 29, 43–52. doi:10.1016/j.euromechflu.2009.09.003
- Jamnongwong, M., Loubiere, K., Dietrich, N., Hebrard, G., 2010. Experimental study of oxygen diffusion coefficients in clean water containing salt, glucose or surfactant: Consequences on the liquid-side mass transfer coefficients. *Chem. Eng. J.* 165, 758–768. doi:10.1016/j.cej.2010.09.040
- Jia, X., Hu, W., Yuan, X., Yu, K., 2015. Effect of surfactant type on interfacial area and liquid mass transfer for CO<sub>2</sub> absorption in a bubble column. *Chinese J. Chem. Eng.* doi:10.1016/j.cjche.2014.11.027

- Johnson, T. a., Patel, V.C., 1999. Flow past a sphere up to a Reynolds number of 300. *J. Fluid Mech.* 378, 19–70. doi:10.1017/S0022112098003206
- Jordan, U., Schumpe, A., 2001. The gas density effect on mass transfer in bubble columns with organic liquids. *Chem. Eng. Sci.* 56, 6267–6272. doi:10.1016/S0009-2509(01)00255-X
- Joseph, D.D., Nguyen, K., Beavers, G.S., 1984. Non-uniqueness and stability of the configuration of flow of immiscible fluids with different viscosities. *J. Fluid Mech.* 141, 319–345. doi:10.1017/S0022112084000872
- Joseph, D.D., Preziosi, L., 2006. Stability of rigid motions and coating films in bicomponent flows of immiscible liquids. *J. Fluid Mech.* 185, 323. doi:10.1017/S0022112087003197
- Kadam, B.D., Joshi, J.B., Koganti, S.B., Patil, R.N., 2008. Hydrodynamic and mass transfer characteristics of annular centrifugal extractors. *Chem. Eng. Res. Des.* 86, 233–244. doi:10.1016/j.cherd.2007.10.020
- Kapic, A., Heindel, T., 2006. Correlating Gas-Liquid Mass Transfer in a Stirred-Tank Reactor. *Chem. Eng. Res. Des.* 84, 239–245. doi:10.1205/cherd.05117
- Kataoka, K., Ohmura, N., Kouzu, M., Simamura, Y., Okubo, M., 1995. Emulsion polymerization of styrene in a continuous Taylor vortex flow reactor. *Chem. Eng. Sci.* 50, 1409–1416. doi:10.1016/0009-2509(94)00515-S
- Kawase, Y., Halard, B., Moo-Young, M., 1987. Theoretical prediction of volumetric mass transfer coefficients in bubble columns for Newtonian and non-Newtonian fluids. *Chem. Eng. Sci.* 42, 1609–1617. doi:10.1016/0009-2509(87)80165-3
- Kawase, Y., Hashiguchi, N., 1996. Gas—liquid mass transfer in external-loop airlift columns with newtonian and non-newtonian fluids. *Chem. Eng. J. Biochem. Eng. J.* 62, 35–42. doi:10.1016/0923-0467(95)03049-2

- Khatab, I.S., Bandarkar, F., Fakhree, M.A.A., Jouyban, A., 2012. Density, viscosity, and surface tension of water+ethanol mixtures from 293 to 323K. *Korean J. Chem. Eng.* 29, 812–817. doi:10.1007/s11814-011-0239-6
- Kim, M., Park, K.J., Lee, K.U., Kim, M.J., Kim, W.-S., Kwon, O.J., Kim, J.J., 2014. Preparation of black pigment with the Couette–Taylor vortex for electrophoretic displays. *Chem. Eng. Sci.* 119, 245–250. doi:10.1016/j.ces.2014.08.036
- Kliphuis, A.M.J., de Winter, L., Vejrazka, C., Martens, D.E., Janssen, M., Wijffels, R.H., 2010. Photosynthetic efficiency of *Chlorella sorokiniana* in a turbulently mixed short light-path photobioreactor. *Biotechnol. Prog.* 26, 687–696. doi:10.1002/btpr.379
- Koch, D.L., Brady, J.F., 1987. Nonlocal dispersion in porous media: Nonmechanical effects. *Chem. Eng. Sci.* 42, 1377–1392. doi:10.1016/0009-2509(87)85010-8
- Koch, D.L., Brady, J.F., 1985. Dispersion in fixed beds. *J. Fluid Mech.* 154, 399–427. doi:10.1017/S0022112085001598
- Koide, K., Yamazoe, S., Harada, S., 1985. EFFECTS OF SURFACE-ACTIVE SUBSTANCES ON GAS HOLDUP AND GAS-LIQUID MASS TRANSFER IN BUBBLE COLUMN. *J. Chem. Eng. Japan* 18, 287–292.
- Kong, B., Shanks, J. V., Vigil, R.D., 2013. Enhanced algal growth rate in a Taylor vortex reactor. *Biotechnol. Bioeng.* 110, 2140–2149. doi:10.1002/bit.24886
- Kong, B., Vigil, R.D., 2014. Simulation of photosynthetically active radiation distribution in algal photobioreactors using a multidimensional spectral radiation model. *Bioresour. Technol.* 158, 141–148. doi:10.1016/j.biortech.2014.01.052
- Kong, B., Vigil, R.D., 2013. Light-limited continuous culture of *Chlorella vulgaris* in a Taylor vortex reactor. *Environ. Prog. Sustain. Energy* 32, 884–890. doi:10.1002/ep.11834

- Krishna, R., Urseanu, M.I., Dreher, A.J., 2000. Gas hold-up in bubble columns: Influence of alcohol addition versus operation at elevated pressures. *Chem. Eng. Process. Process Intensif.* doi:10.1016/S0255-2701(00)00093-3
- Labík, L., Vostal, R., Moucha, T., Rejl, F., Kordač, M., 2014. Volumetric mass transfer coefficient in multiple-impeller gas-liquid contactors. Scaling-up study for various impeller types. *Chem. Eng. J.* 240, 55–61. doi:10.1016/j.cej.2013.11.066
- Lamont, J.C., Scott, D., 1970. Eddy Cell Model of Mass Transfer Into the Surface of a Turbulent Liquid. *AIChE J.* 16, 513–519. doi:10.1002/aic.690160403
- Lathrop, D., Fineberg, J., Swinney, H., 1992. Transition to shear-driven turbulence in Couette-Taylor flow. *Phys. Rev. A* 46, 6390.
- Liang, S.-C.C., Hong, T., Fan, L.S., 1996. Effects of particle arrangements on the drag force of a particle in the intermediate flow regime. *Int. J. Multiph. Flow* 22, 285–306. doi:10.1016/0301-9322(95)00070-4
- Lim, K.S., Zhu, J.X., Grace, J.R., 1995. Hydrodynamics of gas-solid fluidization. *Int. J. Multiph. Flow* 21, 141–193. doi:10.1016/0301-9322(95)00038-Y
- Linek, V., Kordač, M., Fugasová, M., Moucha, T., 2004. Gas-liquid mass transfer coefficient in stirred tanks interpreted through models of idealized eddy structure of turbulence in the bubble vicinity. *Chem. Eng. Process. Process Intensif.* 43, 1511–1517. doi:10.1016/j.cep.2004.02.009
- Linek, V., Kordač, M., Moucha, T., 2005a. Mechanism of mass transfer from bubbles in dispersions part II: Mass transfer coefficients in stirred gas-liquid reactor and bubble column. *Chem. Eng. Process. Process Intensif.* 44, 121–130. doi:10.1016/j.cep.2004.05.009

- Linek, V., Moucha, T., Kordač, M., 2005b. Mechanism of mass transfer from bubbles in dispersions. *Chem. Eng. Process. Process Intensif.* doi:10.1016/j.cep.2004.05.010
- Lochiel, A.C., Calderbank, P.H., 1964. Mass transfer in the continuous phase around axisymmetric bodies of revolution. *Chem. Eng. Sci.* 19, 471–484. doi:10.1016/0009-2509(64)85074-0
- Maheshwari, A., Chhabra, R.P., Biswas, G., 2006. Effect of blockage on drag and heat transfer from a single sphere and an in-line array of three spheres. *Powder Technol.* 168, 74–83. doi:10.1016/j.powtec.2006.07.007
- Maryami, R., Farahat, S., Poor, M.J., Mayam, M.H.S., 2014. Bubbly drag reduction in a vertical Couette–Taylor system with superimposed axial flow. *Fluid Dyn. Res.* 46, 055504. doi:10.1088/0169-5983/46/5/055504
- McClure, D.D., Deligny, J., Kavanagh, J.M., Fletcher, D.F., Barton, G.W., 2014. Impact of surfactant chemistry on bubble column systems. *Chem. Eng. Technol.* doi:10.1002/ceat.201300711
- McClure, D.D., Kavanagh, J.M., Fletcher, D.F., Barton, G.W., 2015. Oxygen transfer in bubble columns at industrially relevant superficial velocities: Experimental work and CFD modelling. *Chem. Eng. J.* 280, 138–146. doi:10.1016/j.cej.2015.06.003
- McClure, D.D., Lee, A.C., Kavanagh, J.M., Fletcher, D.F., Barton, G.W., 2015. Impact of surfactant addition on oxygen mass transfer in a bubble column. *Chem. Eng. Technol.* doi:10.1002/ceat.201400403
- McClure, D.D., Norris, H., Kavanagh, J.M., Fletcher, D.F., Barton, G.W., 2015. Towards a CFD model of bubble columns containing significant surfactant levels. *Chem. Eng. Sci.* 127, 189–201. doi:10.1016/j.ces.2015.01.025

- Mehrabadi, M., Murphy, E., Subramaniam, S., 2016a. Development of a gas–solid drag law for clustered particles using particle-resolved direct numerical simulation. *Chem. Eng. Sci.* doi:10.1016/j.ces.2016.06.006
- Mehrabadi, M., Tenneti, S., Garg, R., Subramaniam, S., 2015. Pseudo-turbulent gas-phase velocity fluctuations in homogeneous gas – solid flow : fixed particle assemblies and freely evolving suspensions. *J. Fluid Mech* 770, 210–246. doi:10.1017/jfm.2015.146
- Mehrabadi, M., Tenneti, S., Subramaniam, S., 2016b. Importance of the fluid-particle drag model in predicting segregation in bidisperse gas-solid flow Importance of the fluid-particle drag model in predicting segregation in bidisperse gas-solid flow. *Int. J. Multiph. Flow.* doi:10.1016/j.ijmultiphaseflow.2016.07.006
- Mehrabadi, M., Tenneti, S., Subramaniam, S., 2012. Gas-phase velocity fluctuations in statistically homogeneous fixed particle beds and freely evolving suspensions using particle-resolved direct numerical simulation. *Int. J. Multiph. Flow.*
- Monahan, S.M., Fox, R.O., 2007. Effect of model formulation on flow-regime predictions for bubble columns. *AIChE J.* 53, 9–18. doi:10.1002/aic.11042
- Moraveji, M.K., Pasand, M.M., Davarnejad, R., Chisti, Y., 2012. Effects of surfactants on hydrodynamics and mass transfer in a split-cylinder airlift reactor. *Can. J. Chem. Eng.* doi:10.1002/cjce.20516
- Murai, Y., Oiwa, H., Takeda, Y., 2005. Bubble behavior in a vertical Taylor-Couette flow. *J. Phys. Conf. Ser.* 14, 143–156. doi:10.1088/1742-6596/14/1/018
- Muroyama, K., Imai, K., Oka, Y., Hayashi, J., 2013. Mass transfer properties in a bubble column associated with micro-bubble dispersions. *Chem. Eng. Sci.* 100, 464–473. doi:10.1016/j.ces.2013.03.043

- Muroyama, K., Oka, Y., Fujiki, R., 2012. Transport properties of micro-bubbles in a bubble column. *J. Chem. Eng. Japan* 45, 666–671. doi:10.1252/jcej.12we066
- Nemri, M., Cazin, S., Charton, S., Climent, E., 2014. Experimental investigation of mixing and axial dispersion in Taylor–Couette flow patterns. *Exp. Fluids* 55, 1769. doi:10.1007/s00348-014-1769-6
- Nobach, H., Damaschke, N., Tropea, C., 2005. High-precision sub-pixel interpolation in particle image velocimetry image processing. *Exp. Fluids* 39, 299–304. doi:10.1007/s00348-005-0999-z
- Oasmaa, A., Elliott, D.C., Mu, S., 2009. Quality Control in Fast Pyrolysis Bio-Oil Production and Use. *Environ. Prog.* 28, 404–409. doi:10.1002/ep
- Özbek, B., Gayik, S., 2001a. The studies on the oxygen mass transfer coefficient in a bioreactor. *Process Biochem.* 36, 729–741. doi:10.1016/S0032-9592(00)00272-7
- Özbek, B., Gayik, S., 2001b. The studies on the oxygen mass transfer coefficient in a bioreactor. *Process Biochem* 36, 729–741. doi:10.1016/S0032-9592(00)00272-7
- Ozgoren, M., 2013. Flow structures around an equilateral triangle arrangement of three spheres. *Int. J. Multiph. Flow* 53, 54–64. doi:10.1016/j.ijmultiphaseflow.2013.02.001
- Ozgoren, M., Dogan, S., Canli, E., Akilli, H., Sahin, B., 2014. Comparison of Different Configurations of Two Spheres at  $Re=5000$  in a Uniform Flow. p. 02.10\_4\_322.
- Ozgoren, M., Okbaz, A., Dogan, S., Sahin, B., Akilli, H., 2013. Investigation of flow characteristics around a sphere placed in a boundary layer over a flat plate. *Exp. Therm. Fluid Sci.* 44, 62–74. doi:10.1016/j.expthermflusci.2012.05.014

- Ozgoren, M., Okbaz, A., Kahraman, A., Hassanzadeh, R., Sahin, B., Akilli, H., Dogan, S., 2011. Experimental investigation of the flow structure around a sphere and its control with jet flow via PIV. 6th IATS 16–18.
- Painmanakul, P., Loubière, K., Hébrard, G., Mietton-Peuchot, M., Roustan, M., Loubière, K., Hébrard, G., Mietton-Peuchot, M., Roustan, M., 2005. Effect of surfactants on liquid-side mass transfer coefficients. *Chem. Eng. Sci.* 60, 6480–6491. doi:10.1016/j.ces.2005.04.053
- Patankar, S. V., 1980. Numerical heat transfer and fluid flow. *Appl. Numer. Math.* 46. doi:10.1002/cite.330530323
- Pinar, E., Sahin, B., Ozgoren, M., Akilli, H., 2013. Experimental study of flow structures around side-by-side spheres. *Ind. Eng. Chem. Res.* 52, 14492–14503. doi:10.1021/ie4022732
- Pirò, D., Quadrio, M., 2008. Direct numerical simulation of turbulent Taylor-Couette flow. *Eur. J. Mech. B/Fluids* 27, 552–566. doi:10.1016/j.euromechflu.2007.10.005
- Pittoors, E., Guo, Y., Van Hulle, S.W.H., 2014. Oxygen transfer model development based on activated sludge and clean water in diffused aerated cylindrical tanks. *Chem. Eng. J.* doi:10.1016/j.cej.2013.12.069
- Polli, M., Stanislao, M. Di, Bagatin, R., Bakr, E.A., Masi, M., 2002. Bubble size distribution in the sparger region of bubble columns. *Chem. Eng. Sci.* 57, 197–205. doi:10.1016/S0009-2509(01)00301-3
- Popovic, M.K., Robinson, C.W., 1989. Mass transfer studies of external-loop airlifts and a bubble column. *AIChE J.* 35, 393–405. doi:10.1002/aic.690350307

- Prahl, L., Hölzer, A., Arlov, D., Revstedt, J., Sommerfeld, M., Fuchs, L., 2007. On the interaction between two fixed spherical particles. *Int. J. Multiph. Flow* 33, 707–725. doi:10.1016/j.ijmultiphaseflow.2007.02.001
- Prahl, L., Jadoon, A., Revstedt, J., 2009. Interaction between two spheres placed in tandem arrangement in steady and pulsating flow. *Int. J. Multiph. Flow* 35, 963–969. doi:10.1016/j.ijmultiphaseflow.2009.05.001
- Pudjiono, P.I., Tavare, N.S., Garside, J., Nigam, K.D.P., 1992. Residence time distribution from a continuous Couette flow device. *Chem. Eng. J.* doi:10.1016/0300-9467(92)85011-W
- Qiao, J., Deng, R., Wang, C.-H., 2014a. Droplet behavior in a Taylor vortex. *Int. J. Multiph. Flow* 67, 132–139. doi:10.1016/j.ijmultiphaseflow.2014.08.011
- Qiao, J., Lew, C.M.J., Karthikeyan, A., Wang, C.-H., 2014b. Production of PEX protein from QM7 cells cultured in polymer scaffolds in a Taylor–Couette bioreactor. *Biochem. Eng. J.* 88, 179–187. doi:10.1016/j.bej.2014.04.012
- Raffel, M., Willert, C.E., Wereley, S.T., Kompenhans, J., 2007. Particle Image Velocimetry, *Current Science.* doi:10.1007/978-3-540-72308-0
- Ramezani, M., Kong, B., Gao, X., Olsen, M.G., Vigil, R.D., 2015. Experimental measurement of oxygen mass transfer and bubble size distribution in an air–water multiphase Taylor–Couette vortex bioreactor. *Chem. Eng. J.* 279, 286–296. doi:10.1016/j.cej.2015.05.007
- Renardy, Y., Joseph, D.D., 1985. Couette flow of two fluids between concentric cylinders. *J. Fluid Mech.* 150, 381. doi:10.1017/S0022112085000179
- Roghair, I., Van Sint Annaland, M., Kuipers, H.J.A.M., 2013. Drag force and clustering in bubble swarms. *AIChE J.* 59, 1791–1800. doi:10.1002/aic.13949

- Rosso, D., Huo, D.L., Stenstrom, M.K., 2006. Effects of interfacial surfactant contamination on bubble gas transfer. *Chem. Eng. Sci.* 61, 5500–5514. doi:10.1016/j.ces.2006.04.018
- Royer, J.R., Evans, D.J., Oyarte, L., Guo, Q., Kapit, E., Möbius, M.E., Waitukaitis, S.R., Jaeger, H.M., 2009. High-speed tracking of rupture and clustering in freely falling granular streams. *Nature* 459, 1110–3. doi:10.1038/nature08115
- Saenton, S., Illangasekare, T., 2013. Effects of incomplete remediation of NAPL-contaminated aquifers: experimental and numerical modeling investigations. *Appl. Water Sci.* 3, 401–414. doi:10.1007/s13201-013-0090-5
- Sakamoto, H., Haniu, H., 1995. The formation mechanism and shedding frequency of vortices from a sphere in uniform shear flow, *Journal of Fluid Mechanics*. Cambridge University Press. doi:10.1017/S0022112095000905
- Sakamoto, H., Haniu, H., Nakamura, T., 1989. A study on vortex shedding from spheres in a uniform flow. *Trans. Japan Soc. Mech. Eng. Ser. B* 55, 1889–1895. doi:10.1299/kikaib.55.1889
- Sakamoto, H., Haniu, H., Sakamoto, H., Haniu, H., Sakamoto, H., Haniu, H., 1990. A Study on Vortex Shedding From Spheres in a Uniform Flow. *J. Fluid Eng.* 112, 386–392. doi:10.1115/1.2909415
- Sardeing, R., Painmanakul, P., Hebrard, G., 2006. Effect of surfactants on liquid-side mass transfer coefficients in gas-liquid systems: A first step to modeling. *Chem. Eng. Sci.* 61, 6249–6260. doi:10.1016/j.ces.2006.05.051

- Sathe, M.J., Deshmukh, S.S., Joshi, J.B., Koganti, S.B., 2010. Computational fluid dynamics simulation and experimental investigation: Study of two-phase liquid-liquid flow in a vertical Taylor-couette contactor. *Ind. Eng. Chem. Res.* 49, 14–28. doi:10.1021/ie900185z
- Sato, Y., Sekoguchi, K., 1975. Liquid velocity distribution in two-phase bubble flow. *Int. J. Multiph. Flow* 2, 79–95. doi:10.1016/0301-9322(75)90030-0
- Scarano, F., Riethmuller, M.L., 2000. Advances in iterative multigrid PIV image processing. *Exp. Fluids* 29, S051–S060. doi:10.1007/s003480070007
- Sch, R., Merten, C., Eigenberger, G., 2002. Bubble size distributions in a bubble column reactor under industrial conditions 26, 595–604.
- Schlichting, D.H., Gersten, K., 1979. Boundary-layer theory. *Eur. J. Mech. - B/Fluids* 20, 817. doi:10.1016/S0997-7546(00)01101-8
- Schlüter, V., Deckwer, W., 1992. Gas/liquid mass transfer in stirred vessels. *Chem. Eng. Sci.* doi:10.1016/0009-2509(92)87060-4
- Sczechowski, J.G., Koval, C.A., Noble, R.D., 1995. A Taylor vortex reactor for heterogeneous photocatalysis. *Chem. Eng. Sci.* doi:10.1016/0009-2509(95)00176-6
- Shah, Y.T., Kelkar, B.G., Godbole, S.P., Deckwer, W.-D., 1982. Design parameters estimations for bubble column reactors. *AIChE J.* 28, 353–379. doi:10.1002/aic.690280302
- Siewert, C., Kunnen, R.P.J., Schröder, W., 2014. Collision rates of small ellipsoids settling in turbulence. *J. Fluid Mech.* 758, 686–701. doi:10.1017/jfm.2014.554

- Sijacki, I.M., Tokic, M.S., Kojic, P.S., Petrovic, D.L., Tekic, M.N., Lukic, N.L., 2013. Sparger type influence on the volumetric mass transfer coefficient in the draft tube airlift reactor with diluted alcohol solutions. *Ind. Eng. Chem. Res.* 52, 6812–6821. doi:10.1021/ie303211u
- Simonnet, M., Gentric, C., Olmos, E., Midoux, N., 2007. Experimental determination of the drag coefficient in a swarm of bubbles. *Chem. Eng. Sci.* 62, 858–866. doi:10.1016/j.ces.2006.10.012
- Singh, N., Prasad, R., 2011. Experimental studies on the effect of inert gases on diffusion distillation of ethanol-water mixtures. *J. Chem. Technol. Biotechnol.* 86, 1495–1500. doi:10.1002/jctb.2659
- Soloff, S.M., Adrian, R.J., Liu, Z.-C., 1999. Distortion compensation for generalized stereoscopic particle image velocimetry. *Meas. Sci. Technol.* 8, 1441–1454. doi:10.1088/0957-0233/8/12/008
- Sorg, R., Tanzeglock, T., Soos, M., Morbidelli, M., Périlleux, A., Solacroup, T., Broly, H., 2011. Minimizing hydrodynamic stress in mammalian cell culture through the lobed Taylor-Couette bioreactor. *Biotechnol. J.* 6, 1504–1515. doi:10.1002/biot.201000477
- Strong, A., Carlucci, L., 1976. An experimental study of mass transfer in rotating Couette flow with low axial Reynolds number. *Can. J. Chem.* ... 5, 295–298.
- Sujatha, K.S., Mani, A., Murthy, S.S., 1999. Experiments on a bubble absorber. *Int. Commun. Heat Mass Transf.* 26, 975–984.
- Sun, B., Tenneti, S., Subramaniam, S., 2015. Modeling average gas-solid heat transfer using particle-resolved direct numerical simulation. *Int. J. Heat Mass Transf.* 86, 898–913. doi:10.1016/j.ijheatmasstransfer.2015.03.046

- Sun, B., Tenneti, S., Subramaniam, S., Koch, D.L., 2016. Pseudo-turbulent heat flux and average gas-phase conduction during gas-solid heat transfer: flow past random fixed particle assemblies. *J. Fluid Mech.* 798, 299–349. doi:10.1017/jfm.2016.290
- Swinney, H., 1978. Hydrodynamic Instabilities and the transition to turbulence, Supplement of the progress of theoretical physics, Topics in Applied Physics. Springer Berlin Heidelberg, Berlin, Heidelberg. doi:10.1143/PTPS.64.164
- Talvy, S., Cockx, A., Liné, A., 2007. Modeling hydrodynamics of gas-liquid airlift reactor. *AIChE J.* 53, 335–353. doi:10.1002/aic.11078
- Taneda S, 1956. Experimental investigations of the wakes behind cylinders and plates at low Reynolds numbers. *J. Phys. Soc. Japan* 11, 302–307.
- Taneda, S., 1959. Downstream development of the wakes behind cylinders. *J. Phys. Soc. Japan* 14, 843–848. doi:10.1143/JPSJ.14.843
- Taneda, S., 1956. Experimental investigation of the wake behind a sphere at low Reynolds numbers. *J. Phys. Soc. Japan* 11, 1104–1105. doi:10.1143/JPSJ.11.1104
- Tang, Y., Lau, Y.M., Deen, N.G., Peters, E.A.J.F., Kuipers, J.A.M., 2016. Direct numerical simulations and experiments of a pseudo-2D gas-fluidized bed. *Chem. Eng. Sci.* 143, 166–180. doi:10.1016/j.ces.2015.12.026
- Taylor, G.I., 1923. Stability of a Viscous Liquid Contained between Two Rotating Cylinders. *Philos. Trans. R. Soc. A Math. Phys. Eng. Sci.* doi:10.1098/rsta.1923.0008
- Tenneti, S., Garg, R., Hrenya, C.M., Fox, R.O., Subramaniam, S., 2010. Direct numerical simulation of gas-solid suspensions at moderate Reynolds number: Quantifying the coupling between hydrodynamic force and particle velocity fluctuations. *Powder Technol.* 203, 57–69. doi:10.1016/j.powtec.2010.03.042

- Tenneti, S., Garg, R., Subramaniam, S., 2011. Drag law for monodisperse gas-solid systems using particle-resolved direct numerical simulation of flow past fixed assemblies of spheres. *Int. J. Multiph. flow* 37, 1072–1092. doi:10.1016/j.ijmultiphaseflow.2011.05.010
- Tenneti, S., Subramaniam, S., 2014. Particle-Resolved Direct Numerical Simulation for Gas-Solid Flow Model Development 46, 199–230. doi:10.1146/annurev-fluid-010313-141344
- Tenneti, S., Sun, B., Garg, R., Subramaniam, S., 2013. Role of fluid heating in dense gas-solid flow as revealed by particle-resolved direct numerical simulation. *Int. J. Heat Mass Transf.* 58, 471–479. doi:10.1016/j.ijheatmasstransfer.2012.11.006
- TOMIYAMA, A., KATAOKA, I., ZUN, I., SAKAGUCHI, T., 1998. Drag Coefficients of Single Bubbles under Normal and Micro Gravity Conditions. *JSME Int. J. Ser. B* 41, 472–479. doi:10.1299/jsmeb.41.472
- Tsai, R.Y., 1987. A Versatile Camera Calibration Technique for High-Accuracy 3D Machine Vision Metrology Using Off-the-Shelf TV Cameras and Lenses. *IEEE J. Robot. Autom.* 3, 323–344. doi:10.1109/JRA.1987.1087109
- Tsuji, T., Narutomi, R., Yokomine, T., Ebara, S., Shimizu, A., 2003. Unsteady three-dimensional simulation of interactions between flow and two particles. *Int. J. Multiph. Flow* 29, 1431–1450. doi:10.1016/S0301-9322(03)00137-X
- Tsuji, Y., Morikawa, Y., Terashima, K., 1982. Fluid-dynamic interaction between two spheres. *Int. J. Multiph. Flow* 8, 71–82. doi:10.1016/0301-9322(82)90008-8
- Ungerman, A.J., Heindel, T.J., 2007. Carbon monoxide mass transfer for syngas fermentation in a stirred tank reactor with dual impeller configurations. *Biotechnol. Prog.* 23, 613–620. doi:10.1021/bp060311z

- van der Meer, A.B., Beenackers, A.A.C.M., Burghard, R., Mulder, N.H., Fok, J.J., 1992. Gas/Liquid mass transfer in a four-phase stirred fermentor: Effects of organic phase hold-up and surfactant concentration. *Chem. Eng. Sci.* doi:10.1016/0009-2509(92)87062-U
- Van Gils, D.P.M., Huisman, S.G., Bruggert, G.W., Sun, C., Lohse, D., 2011. Torque scaling in turbulent Taylor-Couette flow with co- and counterrotating cylinders. *Phys. Rev. Lett.* 106, 024502. doi:10.1103/PhysRevLett.106.024502
- van Gils, D.P.M., Narezo Guzman, D., Sun, C., Lohse, D., 2013. The importance of bubble deformability for strong drag reduction in bubbly turbulent Taylor–Couette flow. *J. Fluid Mech.* 722, 317–347. doi:10.1017/jfm.2013.96
- Van Wachem, B.G.M., Almstedt, A.-E., 2003. Methods for multiphase computational fluid dynamics. *Chem. Eng. J.* 96, 81–98.
- Van't Riet, K., 1979. Review of Measuring Methods and Results in Nonviscous Gas-Liquid Mass Transfer in Stirred Vessels. *Ind. Eng. Chem. Process Des. Dev.* 18, 357–364. doi:10.1021/i260071a001
- Vasconcelos, J.M.T., Rodrigues, J.M.L., Orvalho, S.C.P., Alves, S.S., Mendes, R.L., Reis, A., 2003. Effect of contaminants on mass transfer coefficients in bubble column and airlift contactors. *Chem. Eng. Sci.* 58, 1431–1440. doi:10.1016/S0009-2509(02)00675-9
- Vázquez, G., Cancela, M., Riverol, C., Alvarez, E., Navaza, J., 2000. Application of the Danckwerts method in a bubble column. *Chem. Eng. J.* 78, 13–19. doi:10.1016/S1385-8947(99)00174-6
- Walter, J.F., Blanch, H.W., 1986. Bubble break-up in gas-liquid bioreactors: Break-up in turbulent flows. *Chem. Eng. J.* doi:10.1016/0300-9467(86)85011-0

- Wang, L., Olsen, M.G., Dennis Vigil, R., Vigil, R.D., 2005a. Reappearance of azimuthal waves in turbulent Taylor-Couette flow at large aspect ratio. *Chem. Eng. Sci.* 60, 5555–5568. doi:10.1016/j.ces.2005.05.024
- Wang, L., Vigil, R.D., Fox, R.O., 2005b. CFD simulation of shear-induced aggregation and breakage in turbulent Taylor–Couette flow. *J. Colloid Interface Sci.* 285, 167–178. doi:10.1016/j.jcis.2004.10.075
- Wang, T., Wang, J., 2007. Numerical simulations of gas–liquid mass transfer in bubble columns with a CFD–PBM coupled model. *Chem. Eng. Sci.* 62, 7107–7118. doi:10.1016/j.ces.2007.08.033
- Wang, Z.L., Ding, Y.L., Ghadiri, M., 2004. Flow of a gas-solid two-phase mixture through a packed bed. *Chem. Eng. Sci.* 59, 3071–3079. doi:10.1016/j.ces.2004.03.035
- Weisstein, E.W., n.d. Prolate Spheroid [WWW Document]. MathWorld--A Wolfram Web Resour. URL <http://mathworld.wolfram.com/ProlateSpheroid.html>
- Wereley, S.T., Lueptow, R.M., 1999. Velocity field for Taylor–Couette flow with an axial flow. *Phys. Fluids* 11, 3637. doi:10.1063/1.870228
- Wereley, S.T., Lueptow, R.M., 1998. Spatio-temporal character of non-wavy and wavy Taylor–Couette flow. *J. Fluid Mech.* doi:10.1017/S0022112098008969
- Westerweel, J., 1997. Digital Particle Image Velocimetry. *Meas. Sci. Technol.* 8, 1379–1392. doi:10.1088/0957-0233/8/12/002
- Westerweel, J., 1994. Efficient detection of spurious vectors in particle image velocimetry data. *Exp. Fluids* 247, 236–247. doi:10.1007/BF00206543
- Wilcox, D.C., 1993. Turbulence modeling for CFD. *Aiaa* 93, 2905. doi:0963605151

- Wong, Himmelblau, D.M., 1964. Diffusion of Dissolved Gases in Liquids. *Chem. Rev.* 64, 527–550. doi:10.1021/cr60231a002
- Wongsuchoto, P., Charinpanitkul, T., Pavasant, P., 2003a. Bubble size distribution and gas–liquid mass transfer in airlift contactors. *Chem. Eng. J.* 92, 81–90.
- Wongsuchoto, P., Charinpanitkul, T., Pavasant, P., 2003b. Bubble size distribution and gas–liquid mass transfer in airlift contactors. *Chem. Eng. J.* 92, 81–90. doi:10.1016/S1385-8947(02)00122-5
- Wroński, S., Dłuska, E., Hubacz, R., Molga, E., 1999. Mass transfer in gas–liquid Couette–Taylor flow in membrane reactor. *Chem. Eng. Sci.* 54, 2963–2967. doi:10.1016/S0009-2509(98)00380-7
- Wroński, S., Hubacz, R., Ryszczyk, T., 2005. Interfacial area in a reactor with helicoidal flow for the two-phase gas-liquid system. *Chem. Eng. J.* 105, 71–79. doi:10.1016/j.cej.2004.04.002
- Zhang, S., Wang, D., Bu, F., Zhang, X., Fan, P., 2013. Gas-liquid mass transfer in the presence of ionic surfactant: Effect of counter-ions and interfacial turbulence. *Surf. Interface Anal.* doi:10.1002/sia.5242
- Zhu, C., Liang, S.C.C., Fan, L.S.S., 1994. Particle wake effects on the drag force of an interactive particle. *Int. J. Multiph. Flow* 20, 117–129. doi:10.1016/0301-9322(94)90009-4
- Zhu, X., John Campero, R., Vigil, R.D., 2000. Axial mass transport in liquid–liquid Taylor–Couette–Poiseuille flow. *Chem. Eng. Sci.* 55, 5079–5087. doi:10.1016/S0009-2509(00)00118-4

Zhu, X., Vigil, R.D., 2001a. Banded liquid–liquid Taylor-Couette-Poiseuille flow. *AIChE J.* 47, 1932–1940. doi:10.1002/aic.690470905

Zhu, X., Vigil, R.D., 2001b. Banded liquid-liquid Taylor-Couette-Poiseuille flow. *AIChE J.* 47, 1932–1940. doi:10.1002/aic.690470905

Zhu, X.H., Arifin, D.Y., Khoo, B.H., Hua, J., Wang, C.-H., 2010. Study of cell seeding on porous poly(d,l-lactic-co-glycolic acid) sponge and growth in a Couette–Taylor bioreactor. *Chem. Eng. Sci.* 65, 2108–2117. doi:10.1016/j.ces.2009.12.006